FLAPPING WING DYNAMICS OF MAVs: NONLINEAR MODELING AND EXPERIMENTAL INVESTIGATION

A Thesis presented to
the Faculty of the Graduate School
at the University of Missouri-Columbia

In Partial Fulfillment
of the Requirements for the Degree

Master of Science

---

by

DAR'YA CHERNOVA

Dr. P. Frank Pai, Thesis Supervisor

December 2011

The undersigned, appointed by the dean of the Graduate School, have examined the thesis entitled

FLAPPING WING DYNAMICS OF MAVs:
NONLINEAR MODELING AND EXPERIMENTAL INVESTIGATION

presented by Dar'ya Chernova,

a candidate for the degree of master of science,

and hereby certify that, in their opinion, it is worthy of acceptance.

_____
Professor P. Frank Pai, Thesis Supervisor

_____
Professor John B. Miles

_____
Professor Zhen Chen

To my family…

ACKNOWLEDGEMENTS

I am grateful for the opportunity to work with a very talented professor and scientist, Dr. P. Frank Pai, whose guidance helped me accomplish this work and obtain my master's degree.

I am also grateful for the support of Dr. John B. Miles and Dr. Zhen Chen for being on my thesis committee. Their comments helped in the completion of this thesis. I am also thankful to my friend and graduate student Roxana Martinez Campuzano.

Finally, I am thankful to my friend Noel Heermance for his time in reading this thesis. Also, I am grateful to my family that supported and encouraged me throughout the process.

TABLE OF CONTENTS

LIST OF FIGURES

Figure Page

LIST OF TABLES

Figure Page

FLAPPING WING DYNAMICS OF MAVs: NONLINEAR MODELING AND EXPERIMENTAL INVESTIGATION

Dar'ya Chernova

Dr. P. Frank Pai, Thesis Supervisor

ABSTRACT

Analysis of the flapping-wing motion of micro air vehicles (MAVs) is a complex problem that involves nonlinear structural analysis coupled with unsteady fluid mechanics analysis. In this study I apply a fully nonlinear finite element modeling code for simulation of large-amplitude flapping motions. The MAV wing is modeled using fully nonlinear beam and membrane elements based on geometrically exact total-Lagrangian beam and membrane theories, and the unsteady aerodynamic loads are estimated using the modified strip theory of DeLaurier with improvements by Han. Moreover, in-flight dynamic wing deformations are experimentally measured using an eight-camera real-time digital motion analysis system. For experiments, the reduced frequency is calculated to be approximately 0.51; and *Re* number is about 22,600. Numerical studies that analyze nonlinear deformations of a rigid rectangular plate-like wing are carried out at *Re* number of about 6,400 and reduced frequency of about 0.26. Numerical and experimental results indicate that flapping-wing dynamics is very complicated and is primarily dominated by the unsteady aerodynamic loads. Hence, a reverse design process is recommended using optimization of the time-varying aerodynamic loads with assumed time-varying wing geometries.

CHAPTER 1

Introduction

1.1 Motivation

The recent need for developing new kinds of small unmanned air vehicles with greater endurance, better control, and hover-ability is the major reason for this research. For hundreds of years, man has been fascinated by the flight of natural creatures. It remains an unsolved mystery of nature. Scientists and engineers seek to replicate what birds can do naturally. As an example, planes must maintain a speed higher than the stall speed in order to successfully land, while birds can actually stall and then, using their tail and body, land softly and precisely.

To understand the complexity of 'natural' flight, it's necessary to understand the biomechanics of these creatures – birds, insects and bats. It's important to study their wing organization, and to understand how a particular part of the wing functions to produce flight. At the same time, the goal is to design an air vehicle that is capable of hovering, and, therefore, useful information can be acquired from studying natural hoverers, such as hummingbirds and insects.

From the beginning, pioneers of aeronautics, researchers and experimenters, such as Casey, Lilienthal, and the Wright brothers, were inspired by nature. Today, the method of applying natural principles to engineering the mechanical system is called biomimicry. This method requires the integration of biological and engineering research.

Recent micro air vehicle (MAV) research has tended to follow a certain set of constraints that have been proposed by the Defense Advanced Research Projects Agency (DARPA). [60] The size of MAV's should be limited to 15 centimeters in length, width or height. The concept defined by DARPA also suggests that reconnaissance MAVs should have a range of about 10 km, remain aloft for up to 60 minutes, reach speeds of 10 to 20 m/s (22 to 45 mph), and be capable of real time day/night imagery.

Consistent with those parameters, the preliminary scavenged information revealed the following choice of species capable of flying. Besides birds, we have considered insects and bats. Table 1-1 shows related specifications of different flying creatures, which were selected based on the size constraint.

Table 1-1. Different fliers that have a close fit to the size and weight constraints of MAVs.

No.	Bird /Insect /Bat	Body length (cm)	Wing span (cm)	Weight (g)
1	Blue-throated hummingbird [23, 27, 109]	12.7	20.3	9
2	Magnificent hummingbird [23, 27, 109]	13.3	19	9
3	Black-chinned hummingbird [9, 23, 109]	9.5	12	3
4	Rufous hummingbird [23, 28, 109, 125]	9.5	11.4	3
5	Ruby-throated hummingbird [23, 33, 36, 109]	9.5	11.4	3
6	Emperor dragonfly [122]	8	10.5	
7	Giant Honeybee [83, 121]	2	1.5	0.128
8	Brazilian free-tailed bat [13, 124]	9.5	11.4	12.5

Data presented in Table 1-1 are averaged approximations since every bird or insect is unique in size. If we consider every type of flyer, the research would be immense. Thus, we have decided to use birds as the major object of our 'nature-copying' method. In particular, we will consider as much as possible the smaller-sized birds, such as hummingbirds. The following research, however, is not limited to birds only, and will contain information about other flying creatures for comparison and point out their advantages in adaptation to particular surroundings.

The existing MAV designs have created certain vehicles categorized as follows: fixed wings, rotary wings, and flapping wings. The flapping wing type MAVs are of two types, insect-based MAVs (entomopters), and avian-based MAVs (ornithopters). Examples of existing MAV designs are presented below. Figure 1-1 displays examples of fixed-wing MAVs. Figure 1-2 displays examples of rotary-wing MAVs. And Figs. 1-3 and 1-4 display the flapping wing MAVs.

(a) (b) (c)

Fig. 1-1. Examples of fixed-wing MAVs: (a) Trocoid [3]; (b) WASP [3]; and (c) MC2 microflyer [120].

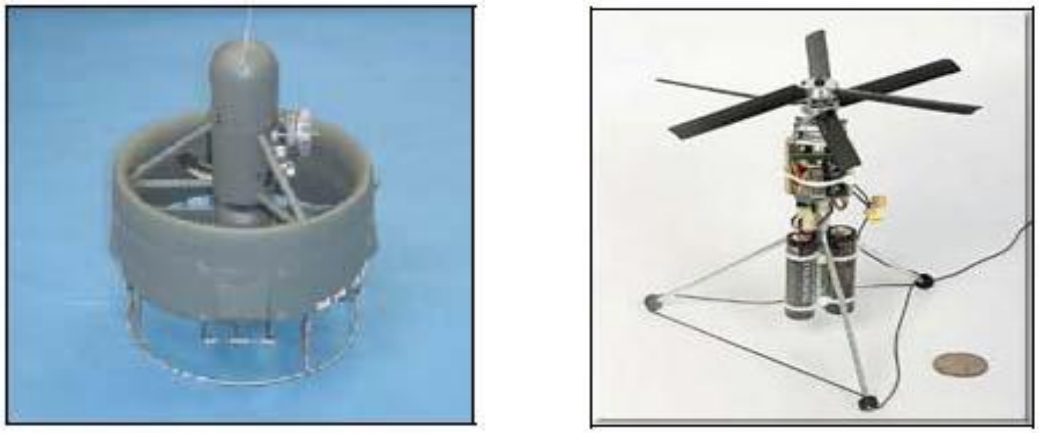

(a) (b)

Fig. 1-2. Examples of rotary-wing MAVs: (a) Micro-Craft Istar [3]; and (b) MICOR [3].

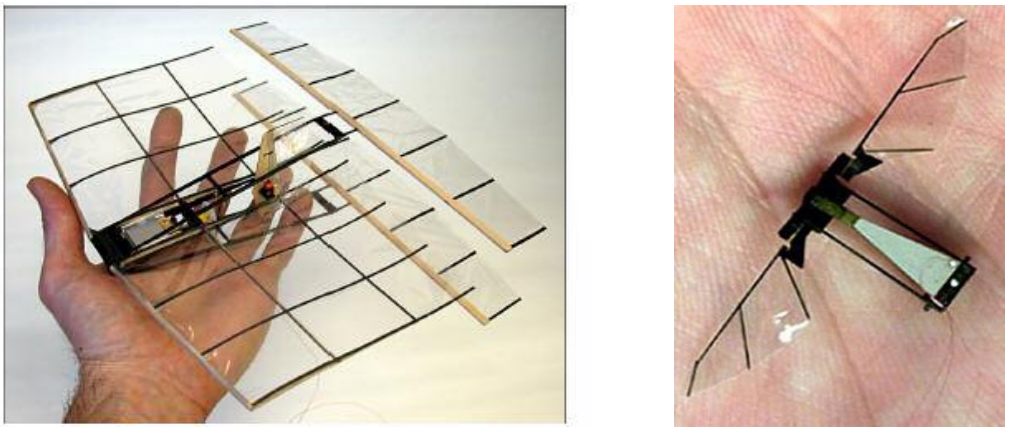

(a) (b)

Fig. 1-3. Examples of insect-based flapping-wing MAVs: (a) NPS with clap-fling mechanism [39]; and (b) Entomopter[123].

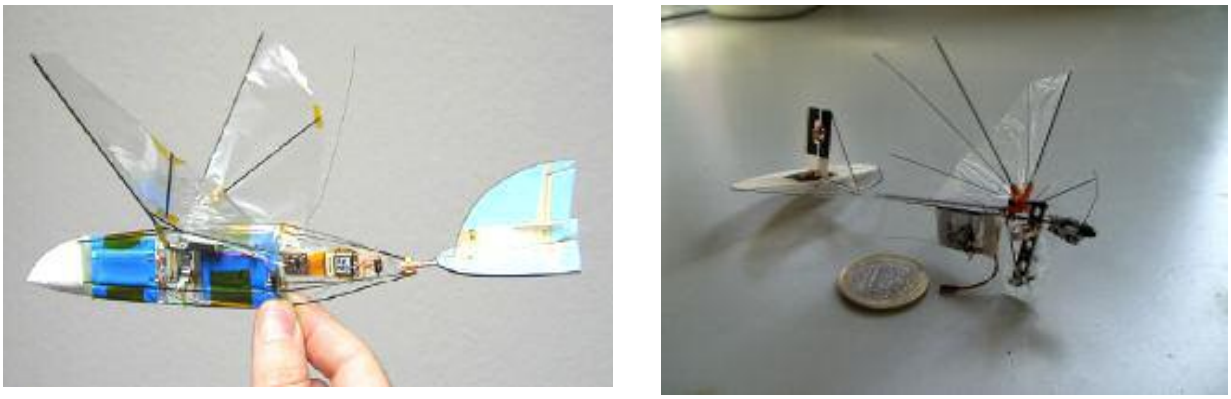

(a) (b)

Fig. 1-4. Examples of avian-based flapping-wing MAVs: (a) Microbat [3]; and (b) DelFly Micro [48].

This research will concentrate on studying forward flight, leaving hovering flight for future investigations. At first, it's important to learn as much as possible about the flight of birds before attempting to design an MAV. Therefore, the attempt is made to gather and review the available information regarding flapping flight. Our perspective on design of MAVs is focused on developing an experimental technique that can be used for such particular research. This experimental method is based on using noncontact sensors to measure the displacements of flapping wings during flight. This study also performs numerical simulations of nonlinear flapping-wing dynamics by using a total-Lagrangian displacement-based nonlinear finite element code (GESA - Geometrically Exact Structural Analysis), which is capable of solving for large-amplitude dynamic elastic displacements and rotations of highly flexible wing structures. Numerical studies in this research analyze linear deformations of flexible membrane wings at a Reynolds number (*Re*) around 22,600 and a reduced frequency around 0.51, and nonlinear deformations of

rigid rectangular plate-like wings at *Re* around 6,400 and a reduced frequency around 0.26.

Most available studies on flapping flight focus on the investigation of the rigid wings. However, biological studies of birds' and insects' kinematics indicate that their wings deform in flight to achieve aerodynamically efficient flight. Also, engineering studies investigating the effects of flexibility indicate that flexible wings perform better than rigid wings. Thus, it is important to study flapping flight with flexible wings. Moreover, it's important to realize that flapping flight is a nonlinearly coupled problem that is highly affected by interrelated aerodynamic and structural inertial forces.

1.2 Thesis Summary

In this thesis, a methodical approach has been adopted to investigate flapping wing dynamics in micro air vehicles. A summary of the contents of each chapter is presented. Chapter One offers an introduction and presents research motivations. It also lists chapter summaries and contributions.

Chapter Two reviews the literature. An extensive literature review was done in order to acquire an understanding of fluid-structure interaction problems related to bird morphology, aerodynamics, kinematics, hummingbird flight, and flapping flight. The morphology section covers the following topics:

- Body shape
- Wing structure

- Wing shape
- Aspect ratio and wing loading for birds
- Variation of wing geometry during flight – active flow control

The aerodynamics section covers the following topics:

- Importance of viscosity
- Scaling and similarity parameters for aerodynamics
- Review of aerodynamics of forward flight: classical theory
- Aerodynamics of forward flight: flapping flight
- Short review of aerodynamics of hovering flight
- Unsteady effects in birds' and insects' flight
- Kinematics

The last section in this chapter provides an overview of structural and aerodynamic models used to analyze flapping flight.

Chapter Three presents the theoretical aeroelasticity framework for the fluid-structure interaction problem of highly flexible flapping wings. It describes in detail the geometrically exact modeling of flapping wings and a nonlinear unsteady aerodynamic theory.

Chapter Four presents numerical simulation results. It includes various linear and nonlinear structural analyses and fluid-structure interaction dynamics of flapping wings.

Chapter Five presents the experimental setup, procedure, and measurement results. It describes in detail a camera-based motion analysis system, experimental setup, and steps for experiment.

Chapter Six summarizes each chapter with conclusions. It also gives recommendations for future work.

1.3 Summary of Contributions

This research offers a perspective into progress and challenges associated with the design of micro air vehicles. This information is a ‘weapon’ that can help ‘fight’ the challenging problem of MAV design. Today, information is readily available, however, not in a systematic way. This research attempts to systematize some particularly useful information for MAV development. It also presents a new experimental approach for the development of MAVs that can also be used in other areas of engineering where dynamic results are required. Finally, this research utilizes a fully nonlinear finite element analysis coupled with an aerodynamic solution technique to investigate the deformation of a wing during flapping flight.

CHAPTER 2

Literature Review

This chapter provides a literature review of the biological and engineering research that can help in the design of MAVs. It is divided into five parts: morphology of birds, aerodynamics of flapping flight, kinematics of flapping flight, hummingbird flight, and flapping flight as a fluid-structure interaction problem.

2.1. Morphology of Birds

Body and wing geometries and their correlation play an important role in in-flight performance of a bird. As limited by the MAV constraints, this research only considers the small birds shown in Table 1-1. Although study of hummingbirds is popular, the limited scope of information available from research on hummingbirds suggests a more general overview of birds as flying species. Study of birds should help to fill out the knowledge gap that exists in study of hummingbirds. Hence, considerations of general trends in morphology of birds are presented here.

2.1.1. Body Shape

Birds have streamlined bodies and adaptive tails. During flight, those morphological features help keep the flow from separation that would cause the increased drag. Bird bodies are covered with feathers that apparently greatly help them to keep the flow from separation. However, according to the experiments of Pennycuick [75], the body of the

dead frozen bird tested in the wind tunnel showed significant flow separation similar to the flow past a blunt body. Figure 2-1 shows the comparison of flows over a dead bird versus an alive bird.

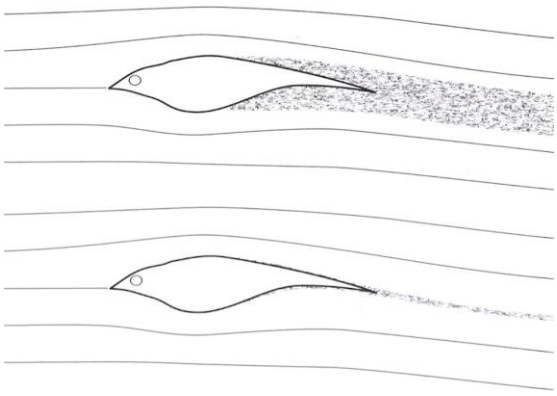

Fig. 2-1. Flow past a dead frozen bird's body (upper), and an alive bird (lower) in the wind tunnel.

Figure 2-1 shows that the alive bird "knows" how to adapt its body in flight to reduce the skin friction drag. For example, a study on Teals [74] showed that the body drag coefficient of an alive bird is about 0.08 and a dead bird is about 0.4. The experiments on dead birds imply that, if we intend to simulate bird flight, we may not be able to achieve the same aerodynamic characteristics that nature gives to birds. Hence, we need to look for ways to reduce the skin friction drag.

On the other hand, bodies of insects have no resemblance with streamlined bodies, and they don"t have feathers. Their bodies are much smaller than those of birds.

2.1.2. Wing structure

Bird wings have three joints – elbow, wrist, and metacarpal joint – that are covered with feathers. The elbow and wrist joints allow motion only in one plane – they work as hinges. Wing span and wing area can be reduced to about a half in an instant by flexing the elbow and wrist joints. The analogy to this motion is the closing/opening of a hand fan. This instant flexing does not affect either mechanical strength or stiffness of the wing and allows the mean cord to stay the same in the fully extended or flexed position. However, hummingbirds almost do not flex their wings, but they use different wing motions to enable different flights. For example, they use a figure „8" motion to enable hovering.

The wing has to be strong enough to resist bending and torsional moments. The wing creates a lift force that results in a bending moment around the wing root. Also, when in flight, a bird has to overcome the twisting moment that acts on its wings.

Birds" wing feathers perform significant aerodynamic functions. First, feathers are actually the material that has to withstand lift and drag forces as well as bending and twisting moments on the wings. Feathers can help increase or decrease wing span and wing area to adapt to particular flight conditions. In relation to aircraft, this is similar to the variable swift of aircraft wings. Second, feathers can reduce flow separation, increase lift, and act as a stall prevention device, similar to flaps used on airplanes during landing at a low forward speed and a high angle of attack. When landing or taking off, a high angle of attack is accompanied by flow separation that could reduce lift and eventually cause stall. To avoid that, the pilot turns on flaps to increase lift and reduce flow

separation in order to have smooth landing or taking off. Figure 2-2 shows a bird that uses feathers as flaps to make a safe landing at a low forward speed [70].

Fig. 2-2. Feathers that serve as flaps to increase lift.

Hummingbirds and swifts have a wing structure that is different from other birds. They have a ball-and-socket joint that allows the wing to rotate in all directions, which is similar to a human‟s arm. Interestingly, hummingbirds can hover and other birds cannot. Hovering is one of the constraints that we are trying to work on. Figure 2-3 compares the wing structures of pelicans and hummingbirds [29].

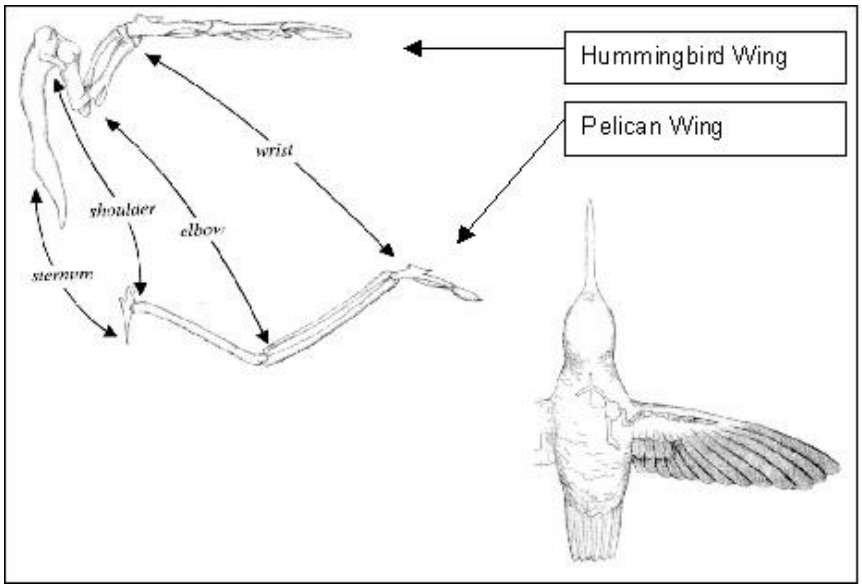

Fig. 2-3. Wing structures of pelicans and hummingbirds.

According to Fig. 2-3, a wing is divided into several parts. The arm wing is the part that is closer to the body, and the hand wing is the part at the tip of the wing – by analogy to the human body. The arm and hand wings play different roles in flight. An arm wing uses the conventional aerodynamic principles (such as attached flow) to generate lift, and the hand wing uses leading edge vortex (LEV) and other unsteady aerodynamics to generate lift.

2.1.3. Wing Shape

Birds‟ wing shapes differ based on their adaptation to nature. Figure 2-4 shows different types of wings and wingtips [109].

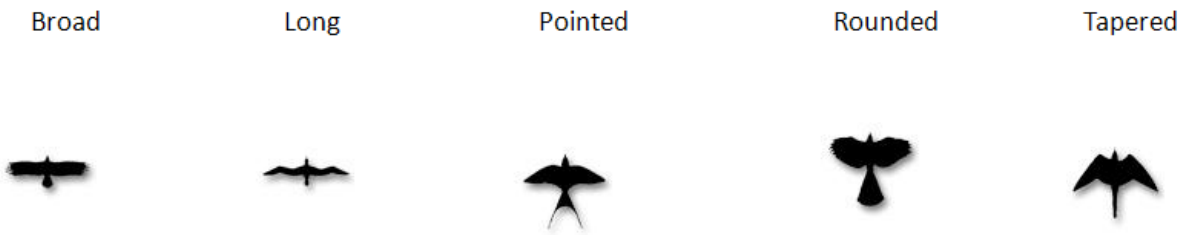

Fig. 2-4. Diversity of wings and wingtips in birds.

In general, wing geometry analysis shows that in adaptation to its surroundings, birds‟ flight differs. Broad wings allow for efficient power use needed for soaring. Long wings allow for efficient lift needed for gliding. Pointed wings allow for reduced drag and, therefore, speedy flight. Rounded or elliptical wings allow for better maneuverability. Tapered wings allow for extremely high speed and maneuverability [20,126].

Hummingbirds possess pointed wings with slightly rounded tips. Figure 2-5 is the photography of the wing of Ruby-throated hummingbird [36].

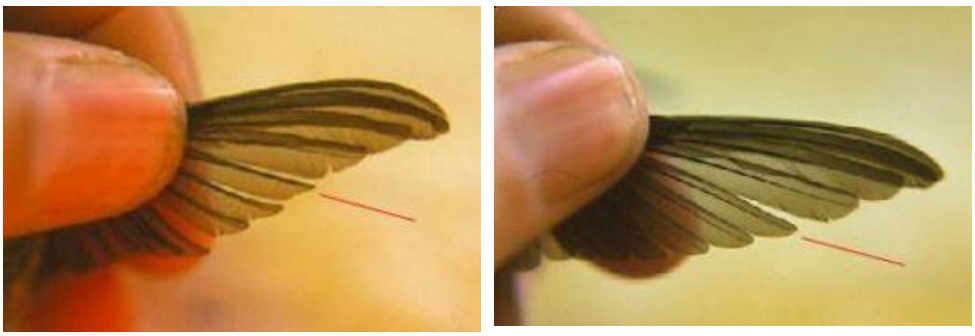

Fig. 2-5. Wing of the Ruby-throated hummingbird.

As can be seen from Fig. 2-5, the wing of the hummingbird appears to be of pointed configuration with a slight curvature at the tip. In aviation language, various wing shapes mean that the birds have different planform shapes. For the hummingbird, the shape of the wing is similar to an elliptical wing. As was proven by Prandl, this type of wings experiences minimum lift-induced drag due to elliptical lift distribution. Figure 2-6 shows an elliptical wing planform and the lift distribution over such a planform [80].

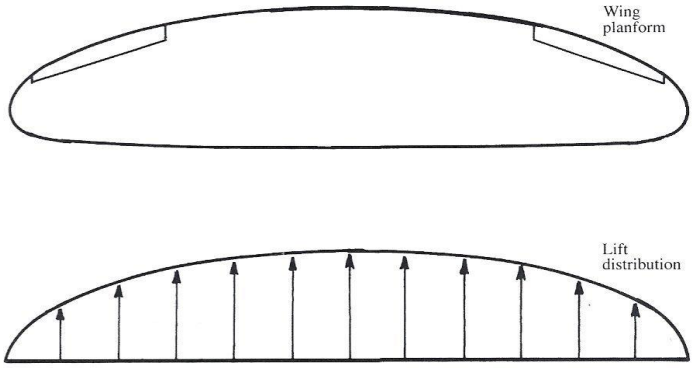

Fig. 2-6. Elliptical (ideal) wing planform and the lift distribution.

As it appears, hummingbirds use their elliptically-shaped wings to create relatively high lift for a small aspect ratio that allows them to be very maneuverable.

2.1.4. Aspect Ratio and Wing Loading

Wing shape can be described in terms of the aspect ratio. In aerodynamics, the aspect ratio is the wing span squared divided by the wing area, or the wingspan divided by the mean chord as given by

$$\mathcal{AR} = \frac{b^2}{A} = \frac{b}{c_{mean}} \tag{2.1}$$

Here, $\mathcal{AR}$ is the aspect ratio, b is the wing span, A is the wing area, and c_{mean} is the mean cord. Figure 2-7 displays a schematic drawing of a bird that shows how to measure the wing span and chord at the root and at the tip of the wing.

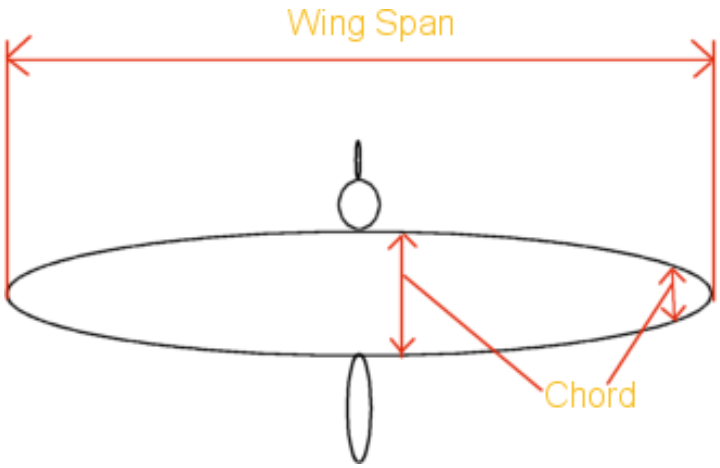

Fig. 2-7. Schematic drawing of a bird.

As discussed at the beginning of Sec. 2.1.3, different shapes are adopted for different functions. However, now we can consider the wing shape in combination with the aspect ratio concept and analyze birds from this standing. Narrow long wings that have very high aspect ratios, like in albatrosses, can generate a lot of lift and are adopted for soaring flight. The Wandering Albatross has an aspect ratio of 15 [72]. Broad long wings with a

high aspect ratio are used for soaring by such birds as eagles, vultures or pelicans. Such wings have reduced drag because the pointed tip has a decreased area that minimizes pressure differences between the top and the bottom, which decreases the turbulence at the wing tip. The Brown Pelican has an aspect ratio of 9.8 [73]. Rounded and short wings that may be tapered and that have a low aspect ratio are used for rapid take off and maneuverability in the areas with dense vegetation, such as forests. Non-migratory passerines, doves and pheasants have that type of wing. For example, the Zebra Finch has an aspect ratio of 4.5 [102]. Pointed short wings that may be tapered and that have a relatively low aspect ratio are used for high speed and maneuverability and can be found, for example, in swallows. The Barn Swallow has an aspect ratio of 7.4 [69].

Besides being very maneuverable and rather speedy, hummingbirds have the ability to hover. This may be among the reasons why they have wings that are somewhere in between pointed-short and rounded-short wings. Hummingbirds have an aspect ratio of about 7 to 8 [9, 10].

Figure 2-8 pictorially shows wing shapes of different birds with different flying functions and aspect ratios [15]. As research shows, an aspect ratio is the parameter that would depend on the type of the surrounding fluid: whether it is water or air. According to McLetchie [59], tested birds and fish of different aspect ratios showed that the aspect ratio of 4 gave the highest coefficient of thrust in the water. He also pointed out that these findings are consistent with most 3-D flapping foils of sea birds and flying fish found in nature.

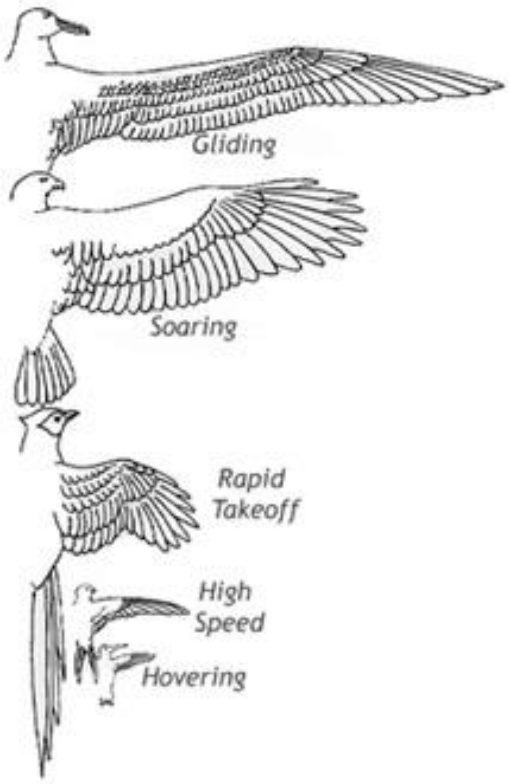

Fig. 2-8. Birds' wings and respected flight adaptations.

The aspect ratio by itself is not a very useful parameter unless the wing loading parameter is known. The wing loading is defined as the ratio of the bird‟s weight to the area of both wings and is expressed as[1]

$$Wing\ Loading = \frac{Mass_{bird}}{Area_{wings}} \qquad (2.2)^2$$

The larger is the wing loading, the more energy it requires for flying. On the other hand, the lower is the wing loading, the lower is the energy consumption, and, therefore, the lower is the minimum velocity at which the flight is possible. As a result, the wing

[1] http://www.csd.net/~cgadd/eflight/calcs_wingload.htm - wing loading calculator

[2] Here, wing loading is given in mass over area units; however, it also can be given in force over area units.

loading also affects the take-off and landing distances. When designing airplanes, the aspect ratio should be taken into consideration as the variable: the faster the plane flies, the more lift it produces per wing unit area, so the same weight can be carried by the wing with a smaller aspect ratio. Structurally, having shorter wings is advantageous because it allows the plane to carry less weight and be more maneuverable. Birds and planes both are subject to the laws of aerodynamics. However, their scales and the flight speeds are very different; and, therefore, it is reflected in the values of their wing loadings and aspect ratios. Table 2-1 shows planes and different species of birds with their respective wing loadings and aspect ratios.

Table 2-1. Planes and birds and their respective wing loadings and aspect ratios.

Fliers[3]	**Wing-loading** ($^{kg}/_{m^2}$)	**Aspect Ratio**
Magnificent Hummingbird [9]	2.52	8.4[4]
Barn Swallow [69]	1.39	7.4
Brown Pelican [73]	5.89	9.8
Homebuilt [80]	54	6
Transport jet [80]	586	~10

[3] Items are listed in the order of increasing mass.

[4] approximated from the wing length

Figure 2-9 compares these two important factors – the aspect ratio and the wing loading – for various nature- and man-made fliers [64].

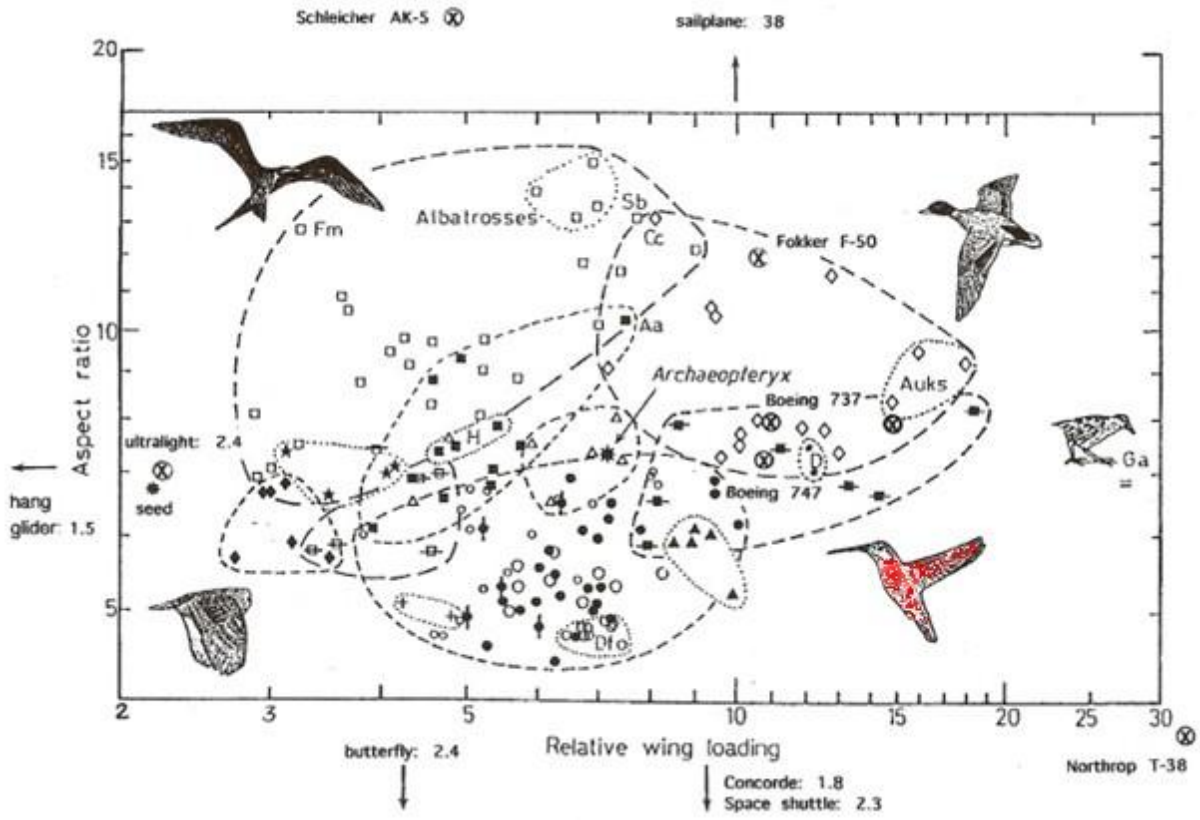

Fig. 2-9. Aspect ratio vs. wing loading index in some fliers.

As you can see from Fig. 2-9, the hummingbird, highlighted in red and located in the right lower corner, has a relatively low aspect ratio with a relatively high wing loading. From an aerodynamic point of view, both these characteristics do not favor the hummingbird. The low aspect ratio contributes to the high lift-induced drag. The high wing loading makes them consume more energy during flight; however, at the same time, it makes hummingbirds more maneuverable. Thus, contrary to the aerodynamic theory, nature created the hummingbird as quite wonderful flier and a great hoverer.

Wingtips are also important, and they depend on a bird‟s environment as well. Figure 2-10 illustrates four extremes of the wingtips according to pointedness and convexity [56]. Pointedness is the shift in wingtip toward the leading edge, and convexity is the decrease in acuteness of the wingtip. Figures 2-10 (a) and (b) illustrate the extremes of pointedness: (a) - rounded-shape wing that has low aspect ratio, and (b) – pointed-shape wing that is of high aspect ratio. Figures 2-10 (c) and (d) illustrate the extremes of convexity: (c) – concave wing, and (d) – convex wing.

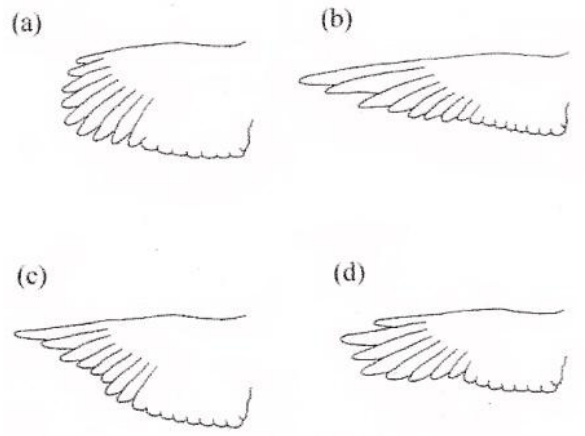

Fig. 2-10. Theoretical wings: extremes of pointedness and convexity.

Figure 2-11 continues the subject of wing pointedness and convexity [56]. Here, it demonstrates the spread of real bird species according to these qualities of their wings. Bird „*a*‟ is the tern, bird „*b*‟ is the duck, bird „*c*‟ is the pigeon, bird „*d*‟ is the gull, bird „*e*‟ is the magpie, bird „*f*‟ is the soaring hawk, and bird „*g*‟ is the sparrow hawk.

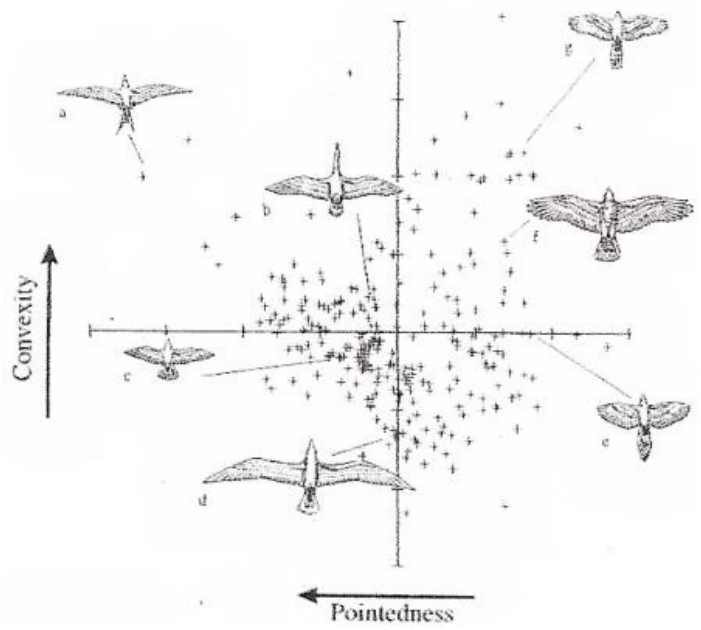

Fig. 2-11. Distribution of bird species according to wing pointedness and convexity.

According to Fig. 2-5, hummingbirds may be found located in the second quadrant of Fig. 2-11. Their wings are relatively pointed and are rather slightly convex than concave.

2.1.5 Variation of the Wing Geometry during Flight – Active Flow Control

Birds possess various wing shapes; however, any particular shape has the ability to change during flight as the bird applies active flow control. Birds constantly change wing geometry, including wing shape, wingspan, wing area, twist and so on and their original wing shape, optimizing the flight and energy consumption. For example, studies on doves [71] and swifts [49] show that, as the speed increases, the wingspan decreases. Figure 2-12 shows swift‟s variable wing geometry in flight [49].

(a)

(b)

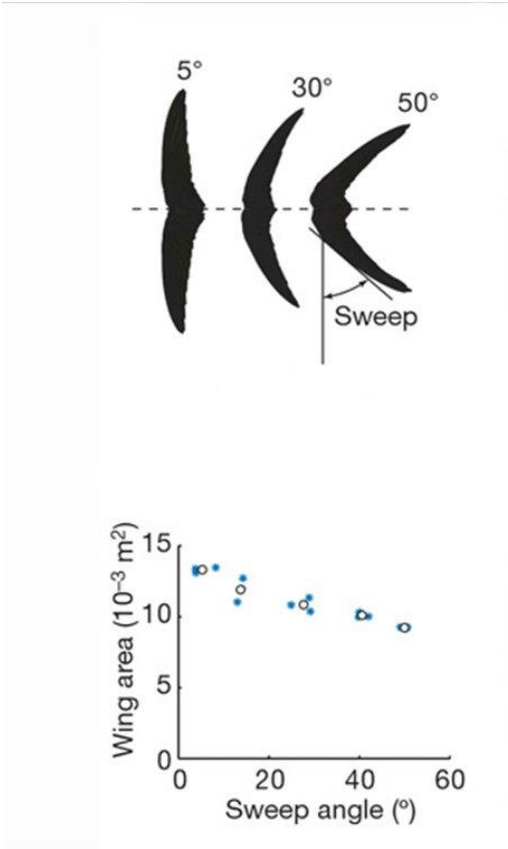

Fig. 2-12. (a) Variable sweep angle in swifts; (b) graph of the wing area: filled dots – values of individual wings, open circles – average value per sweep.

For hummingbirds, variation of the wing geometry is present, however not that drastic as for other species. Figure 2-13 shows wingspan as a function of flight speed for a variety of birds including hummingbirds [103]. As can be seen from this figure, hummingbirds display the highest span ratio, i.e. they fly with almost straight wings. Also, it can be seen that variation of the wing geometry for hummingbirds is almost independent of speed.

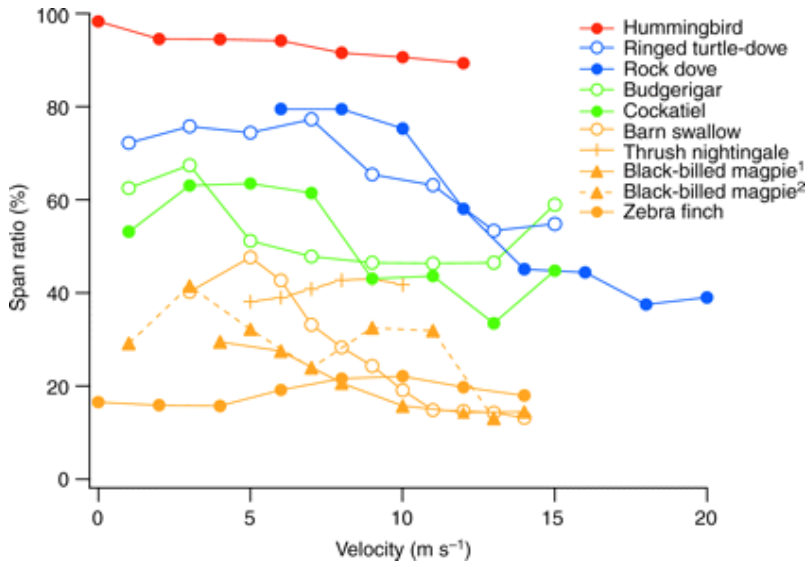

Fig. 2-13. Wingspan ratio as a function of flight velocity compared among bird species. (Values shown are means.)

From Fig. 2-13 we see that, according to the study of kinematics of different bird species conducted by Lentink *et al.* [49], the average wingtip span ratio for the hummingbird is 93 percent among different velocities, where as the span ratios in other species vary from 17 to 80 percent.

In modeling the hummingbird wing, 93 percent can be seen from different perspectives. On one hand, the span ratio of 93 percent is relatively larger than the maximum span ratio of 80 percent achieved by other birds, and therefore, the wing can be considered as „rigid". This view is supported by the study of Greenewalt [30] and modeled in several studies as the mechanical oscillator. On the other hand, a span ratio of 93 percent serves as the evidence that the hummingbird does slightly flex its wings on upstroke. Using the latter perspective, we use the flexible wing theory to model the wing for our MAV for numerical analysis.

2.2 Aerodynamics of Flapping Flight

2.2.1 Importance of Viscosity

Viscosity is the physical property that defines the resistance of a fluid to forces acting on it. Viscous flow involves friction that causes energy loss as well as heat conduction and mass diffusion. Lift force is mostly due to pressure, and, therefore, inviscid flow assumption works in conjunction with Kutta condition at the trailing edge [4]; and, therefore, Bernoulli principle applies. Total drag, however, cannot be predicted by inviscid flow (d‟Alembert‟s paradox). Friction of a viscous flow causes shear stresses on the surface that is moving through the fluid as well as it causes separation of the flow from the surface. Thus, to work in a real world, one has to solve the governing equations of motion – Navier-Stokes equations together with conservation of mass equation – of the viscous flow to account for lift and drag as well. Navier-Stokes equations (Eqs. (2.3), (2.4), and (2.5)) along with continuity equation (Eq. (2.6)) for a three-dimensional, unsteady, incompressible flow are given below.

Convective terms *Viscous effects – Shear stress terms*

Transient term *Pressure term*

$$\rho\left(\frac{\partial u}{\partial t}+u\frac{\partial u}{\partial x}+v\frac{\partial u}{\partial y}+w\frac{\partial u}{\partial z}\right)=-\frac{\partial p}{\partial x}+\rho g_x+\mu\left(\frac{\partial^2 u}{\partial x^2}+\frac{\partial^2 u}{\partial y^2}+\frac{\partial^2 u}{\partial z^2}\right) \quad (2.3)$$

$$\rho\left(\frac{\partial v}{\partial t}+u\frac{\partial v}{\partial x}+v\frac{\partial v}{\partial y}+w\frac{\partial v}{\partial z}\right)=-\frac{\partial p}{\partial y}+\rho g_y+\mu\left(\frac{\partial^2 v}{\partial x^2}+\frac{\partial^2 v}{\partial y^2}+\frac{\partial^2 v}{\partial z^2}\right) \quad (2.4)$$

$$\rho\left(\frac{\partial w}{\partial t}+u\frac{\partial w}{\partial x}+v\frac{\partial w}{\partial y}+w\frac{\partial w}{\partial z}\right)=-\frac{\partial p}{\partial z}+\rho g_z+\mu\left(\frac{\partial^2 w}{\partial x^2}+\frac{\partial^2 w}{\partial y^2}+\frac{\partial^2 w}{\partial z^2}\right) \quad (2.5)$$

$ma_z = Inertia\ Force$ *Surface Force* *Body Force* *Surface Force*

$$\frac{\partial \rho}{\partial t}+\frac{\partial(\rho u)}{\partial x}+\frac{\partial(\rho v)}{\partial y}+\frac{\partial(\rho w)}{\partial z}=0 \quad (2.6)$$

Rewriting Eqs. (2.3), (2.4), and (2.5) in a vector form gives Eq. (2.7):

$$\rho\frac{D\boldsymbol{V}}{Dt}=\rho\left(\frac{\partial \boldsymbol{V}}{\partial t}+(\boldsymbol{V}\cdot\boldsymbol{\nabla})\boldsymbol{V}\right)=-\boldsymbol{\nabla}P+\rho\boldsymbol{g}+\mu\boldsymbol{\nabla}^2\mathbf{V} \quad (2.7)$$

In Eq. (2.7), ρ is the fluid density, V is the characteristic velocity, P is the pressure, g is the gravitational acceleration, μ is the dynamic viscosity, and t is the time.

Rewriting Eq. (2.7) in non-dimensional form gives Eq. (2.8):

$$[St]\frac{D\boldsymbol{V}^*}{Dt^*} + (\boldsymbol{V}^* \cdot \boldsymbol{\nabla}^*)\boldsymbol{V}^* = -[Eu]\boldsymbol{\nabla}^* P^* + \left[\frac{1}{Fr^2}\right]\boldsymbol{g}^* + [\frac{1}{Re}]\boldsymbol{\nabla}^{*2}\boldsymbol{V}^* \tag{2.8}$$

In Eq. (2.8), non-dimensional similarity parameters, such as Strouhal, Euler, Froude, and Reynolds numbers, and terms with asterisks are defined by the following equations:

$$St = \frac{fL}{V} \tag{2.9}$$

$$Eu = \frac{P_0 - P_\infty}{\rho V^2} \tag{2.10}$$

$$Fr = \frac{V}{\sqrt{gL}} \tag{2.11}$$

$$Re = \frac{\rho VL}{\mu} \tag{2.12}$$

$$t^* = ft \tag{2.13}$$

$$P^* = \frac{P - P_\infty}{\rho V^2} \tag{2.14}$$

$$\boldsymbol{g}^* = \frac{\boldsymbol{g}}{g} \tag{2.15}$$

$$\boldsymbol{V}^* = \frac{\boldsymbol{V}}{V} \tag{2.16}$$

$$\boldsymbol{\nabla}^* = L\boldsymbol{\nabla} \tag{2.17}$$

For Eqs. (2.9), (2.10), (2.11), (2.12), (2.13), (2.14), (2.15), (2.16), and (2.17), f is the characteristic frequency, L is the characteristic length, P_0 is the local pressure, P_∞ is the freestream pressure, and ∇ is the gradient term.

Getting back to the meaning of viscosity for the various fliers, it should be noted that, for larger airplanes, inviscid flow can be assumed; however, for birds and insects, viscosity plays a very important role for their mechanisms of flight, which is discussed later.

2.2.2 Scaling and Similarity Parameters for Aerodynamics

For the aerodynamics of the birds‟ flight, certain non-dimensional similarity parameters have more meaning for analysis than others. They are Reynolds number and Strouhal number. Another dimensionless parameter that is used in analysis of the flapping flight, but not used for steady wings, is the reduced frequency.

For the hummingbird flight, viscous effects are important, and it can be characterized by the Reynolds number *Re*. *Re* is an important non-dimensional similarity parameter that allows performing model testing in the smaller scales using wind tunnels. For geometrically similar bodies, flows around them are the same if *Re* number is the same. The formula for *Re* number is given by Eq. (2.12). Rewriting Eq. (2.12) in aerodynamics terms gives Eq. (2.18):

$$Re = \frac{\rho V_\infty c_m}{\mu} \tag{2.18}$$

Here, ρ is the fluid density, V_∞ is the free stream velocity or forward velocity of the body, c_m is the mean chord length (ratio of the wing area to the wing span), and μ is the fluid dynamic viscosity. Thus, for inviscid flows, *Re* number would go to infinity.

Re is important for aerodynamics because lift and drag are functions of *Re* and the Mach number M_a. These relationships are shown in Eqs. (2.19) and (2.20), where C_L and C_D are lift and drag coefficients respectively. M_a is not relevant for birds‟ flight since it is used for the cases when air becomes compressible.

$$C_L = f(shape, Re, Ma, surface\ roughness, angle\ of\ attack) \qquad (2.19)$$

$$C_D = f(shape, Re, Ma, surface\ roughness, angle\ of\ attack) \qquad (2.20)$$

Re defines the ratio of inertia forces to viscous forces. For the case with birds‟ flight, lift and drag are due to inertial forces like in an airplane; however, viscous forces are quite dominant because birds‟ *Re* ranges from 10,000 to 500,000 [75], whereas large airplanes may have *Re* ranges from 10^7 or more. For hummingbirds, whose mass ranges from 3 to 10 grams, *Re* for forward flight ranges from 10,000 to 19,000, and, for hovering, it ranges from 6,000 to 12,000 [10]. At lower *Re*, it is harder to keep the boundary layer attached. In recent studies, there can be found distinctions between low *Re* and ultra-low *Re* fliers. The former applies for birds mostly, and the latter applies for insects, whose flight mechanisms are adapted to „extremely‟ viscous conditions.

An interesting fact about low *Re* can be seen in Fig. 2-14 [40]. It shows lift-drag polars[5] for various airfoils at various *Re* numbers. At lower *Re* , curved plate performs better than a smooth airfoil. In relation to birds, whose wings have relatively thin airfoil profile and are cambered, this shows that birds use the nature-created devices that help them to be effective fliers at low *Re* numbers.

[5] Polar - lift plotted against drag with α marked on the curve.

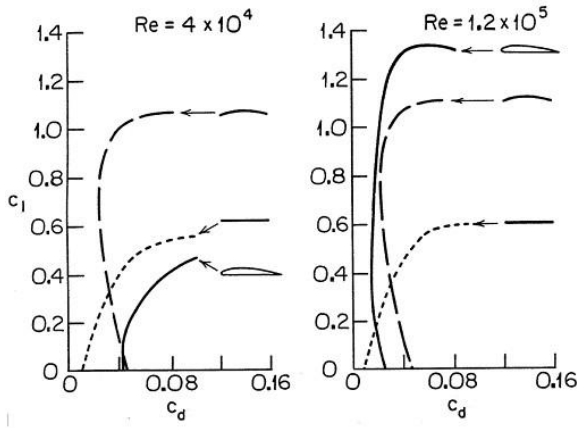

Fig. 2-14. Lift-drag polars for different airfoils at different Reynolds numbers.

Re serves as a means to distinguish types of flows, such as laminar, transitional, and turbulent. As it appears, for mimicking hummingbird flight, the laminar flow should be considered, of which *Re* ranges up to 30,000 [53]. Flow in a laminar boundary layer tends to separate at the higher angle of attack. For small angles of attack, the pressure gradients are not large, and the boundary layer doesn‟t separate. However, as soon as the angle of attack gets larger, laminar boundary layer separates because fluid particles have relatively small velocities, and they cannot overcome the adverse pressure gradient. The separated flow becomes irregular and turbulent. This turbulent flow may reattach itself as a turbulent boundary layer. If this happens, a laminar separation bubble forms. Figure 2-15 shows formation of a laminar separation bubble [53].

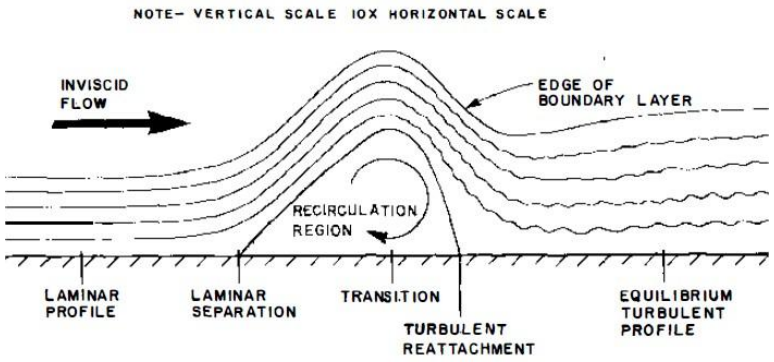

Fig. 2-15. Formation of a laminar separation bubble.

By definition, laminar flow is a steady flow where velocity at a given point in space doesn‟t vary with time [62]. However, birds‟ flight is based on unsteady effects, such as different types of vortices shed from the leading and trailing edges as well as tips of wings, and, therefore, aerodynamic laws for laminar flow may apply at the boundary layer, but may not be applicable in the flow in the vicinity of the bird. Besides that, air flow around the bird may not be laminar, due to wind gusts or roughness of the earth surface. Thus, turbulence laws come into play.

According to aerodynamic experiments on drag around a cylinder that is placed in a moving fluid, at *Re* between 40 and 100,000 – range that covers the *Re* for the hummingbird flight, periodic flow develops downstream from the cylinder. Vortices shed from this cylinder create so-called Karman vortex street – oscillating flow of discrete

frequency. For a flow that has the Karman vortex trail phenomenon, *Re* can be correlated with another dimensionless similarity parameter, Strouhal number.

Strouhal number *St* is defined in Eq. (2.9) and it can be rewritten as Eq. (2.21) for the use in birds‟ flight aerodynamics.

$$St = \frac{2fh_a}{V_\infty} \tag{2.21}$$

In Eq. (2.21), f is the flapping frequency, h_a is the flapping (or heaving) amplitude, and V_∞ is the free stream velocity or forward velocity of the body. Some authors use wing tip amplitude [75] or wake width [5, 77] instead of flapping amplitude. In this case, wing tip amplitude is twice the flapping amplitude.

St describes wing kinematics and defines the ratio of local inertia forces that are due to unsteadiness of the flow to convective inertia forces that are due to changes in velocity from point to point in the flow field. *St* is important in the study of unsteady, oscillating flow.

According to Taylor *et al.* [101], propulsive efficiency of flying animals is maximized at *St* between 0.2 and 0.4. Sea animals indeed operate at this range; however, birds were found to only cruise at this range. Similarly, Triantafyllou *et al.* [105] suggested that the optimal propulsion efficiency of a flapping airfoil occurs at *St* between 0.2 and 0.3, which corresponds to the maximum inverse Kármán vortex street inside the wake.

Similar to *St*, the reduced frequency and its reciprocal (i.e., advanced ratio) are the non-dimensional parameters that give indication on importance of unsteady effects.

According to Ellington [21], the advanced ratio *J* shows the ratio of the body velocity to the mean velocity of the wing tip, and it is given by Eqs. (2.22a) and (2.22b):

$$J = \frac{V_\infty}{2h_a f l} \tag{22a}$$

$$J = \frac{V_\infty}{V_{tip}} \tag{22b}$$

Here, V_∞ is the free stream velocity or forward velocity of the body, h_a is the flapping amplitude given in radians, f is the flapping frequency, and l is the wing length that is equal to half the wing span (i.e., *b/2*). In Eq. (2.22b), V_{tip} is the flapping velocity with respect to the body, or the tip speed, or else plunge velocity.

There is another way to express advanced ratio as given by Eq (2.23) [87].

$$J = \frac{V_\infty}{2\pi f h_a} \tag{23a}$$

$$J = \frac{V_\infty}{\omega h_a} \tag{23b}$$

$$J = \frac{1}{\pi \cdot St} \tag{23c}$$

In Eq. (2.23b), ω is the angular (pitch/plunge) velocity.

The reduced frequency *k* is given by Eq. (2.24):

$$k = \frac{1}{J} = \frac{2h_a f l}{V_\infty} \tag{2.24}$$

There is another way to define the reduced frequency: the ratio of the pitching velocity (ωc) to the free stream velocity which is shown by Eq. (2.25) [67,77]:

$$k = \frac{2\pi f c_m}{V_\infty} = \frac{\omega c_m}{V_\infty} \tag{2.25}$$

Here, ω is the angular (pitch/plunge) velocity, c is the mean chord length, f is the flapping frequency, and V_∞ is the free stream velocity.

Some sources [5, 75] present the reduced frequency for just a half cycle as given by Eq. (2.26).

$$k = \frac{\pi f c_m}{V_\infty} = \frac{0.5\omega c_m}{V_\infty} \tag{2.26}$$

According to Pennycuick [75], the reduced frequency is the ratio of the distance over one wing beat cycle that the bird travels forward to the mean chord length. If wing tips move up and down with large amplitude, the quick change between upstroke and downstroke produces unsteady aerodynamic effects. In this case the value of the reduced frequency is large as a result of low forward velocity and larger flapping velocity. If the motion of the tips is mostly horizontal, flow can be considered quasi-steady. In this case the value of the reduced frequency is small as a result of large forward velocity and smaller flapping velocity. Thus, high values of reduced frequency indicate rapid changes of flow geometry through the wing beat cycle, and, therefore, unsteady aerodynamic effects need to be considered. For low values of reduced frequency, quasi-steady assumption is applicable. Reduced frequency ranges from zero to infinity. According to Pennycuick, as a rough rule of thumb, reduced frequency of less than 0.2 can be considered quasi-steady.

2.2.3 Aerodynamics of the Forward Flight: Classical Theory

The major goal of theoretical aerodynamics is to calculate pressure and shear stresses acting on a body. In order words, it is to calculate lift, drag, and moments. In order to do this, governing equations of motion have to be solved first for the flow field variables, such as pressure, density, velocity vector, etc. Then, this solution is used to obtain lift, drag, and moments acting on a wing.

The research concentrates on fliers with low *Re* numbers. Figure 2-16 shows ranges of *Re* numbers for various fliers [53].

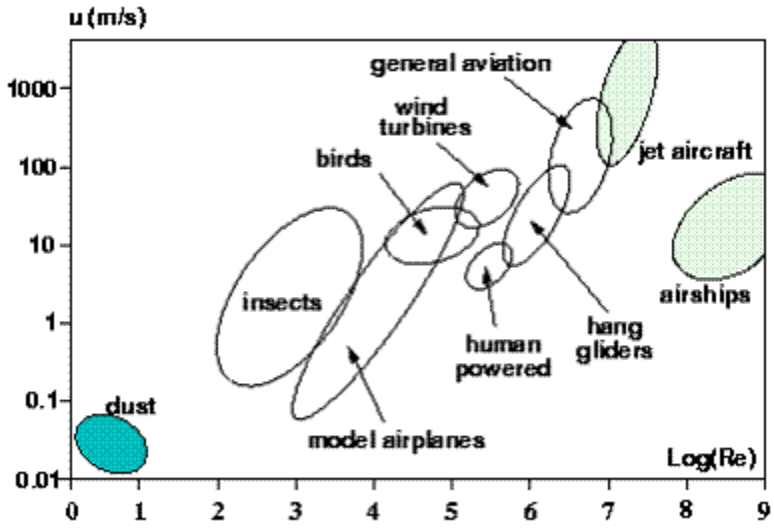

Fig. 2-16. Variation of Reynolds numbers with speed for various natural and man-made fliers.

As can be seen from Fig. 2-16, insects‟ *Re* numbers range from about 10^2 to about 10^4, and birds‟ *Re* numbers range from about 10^4 to about 10^6. Engine-powered planes‟ *Re* numbers range from about 10^6 and higher. For planes with fixed wings classical aerodynamic theory applies. Fundamental concepts of forward flight of the fixed wing

are discussed in this part. These concepts are also applicable for the bird‟s flapping flight, since, as mentioned in Sec. 2.1.2, birds use conventional aerodynamic principles for the arm-wing part of their bodies.

During forward flight, there is a lot going on to make the flight possible. At the wing‟s border, the boundary layer laws start to act due to viscosity of the surrounding fluid. At the very boundary, there is no-slip condition, where as a little further the value of velocity is not zero any more. This creates a velocity gradient that causes shearing stresses in the fluid that surrounds the wing. For Newtonian fluids, shear stress is proportional to the rate of shearing strain – also so called the rate of angular deformation, or velocity gradient – through the coefficient called dynamic viscosity. This relation is called constitutive equation. In other words, a bird, while flying, does work on the surrounding air that causes shear stresses to develop in the surrounding fluid.

Due to the velocity gradient, the fluid particle starts to rotate. And, because of viscosity, this fluid particle would attract other particles that combined would create a vortex. A three-dimensional vortex has a center line, or filament, that consists of a line of fluid particles that rotate, according to Helmholtz‟s theorems, with a constant strength along this line. The flow around the filament stays irrotational, which means that particles don‟t rotate around their own axes. As the radius of the vortex increases, the tangential velocity of fluid particles circulating around the core decreases. The strength of vortex is called circulation. Circulation is the property of the irrotational flow – not the vortex filament. Integrating the component of the local tangential velocity along any closed path that contains the vortex filament gives the circulation.

$$\Gamma = \oint V_{t\ local} \cos\varphi ds \tag{2.27}$$

Here, Γ is the circulation, $V_{t\ local}$ is the component of the local tangential velocity, and φ is the angle between the local velocity vector and the path of integration.

Lift is related to circulation by the Kutta-Joukowski theorem that is given as follows:

$$L' = V_{\infty\ local}\, \rho_\infty \Gamma \tag{2.28}$$

Here, L' is the two-dimensional lift or the lift per unit span, $V_{\infty\ local}$ is the local free stream velocity or forward velocity of the body, ρ_∞ is the density of the fluid, and Γ is the circulation.

The circulation theory of lift is an alternative way of deriving lift equation. The other way is to think about forces that act on the body. Net effect of the pressure, p, and shear stresses, τ, distributions integrated over the entire surface is the resultant force, R, and moment, M, on the body. They are shown in Figs. 2-17(a) and (b) [4].

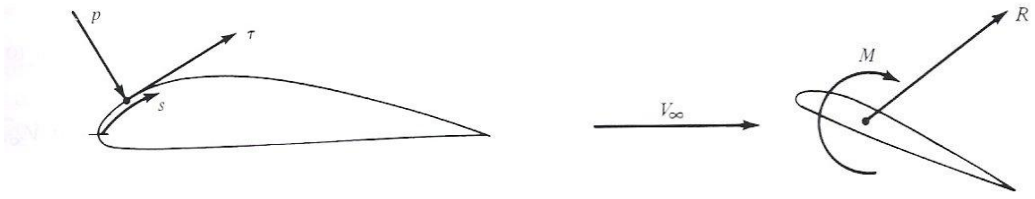

(a) (b)

Fig. 2-17. Aerodynamic loads: (a) pressure and shear stress on the body surface; (b) resultant aerodynamic force and moment on the body.

The resultant force, R, in Fig. 2-17(b) can be divided into components of two sets shown in Fig. 2-18 [4].

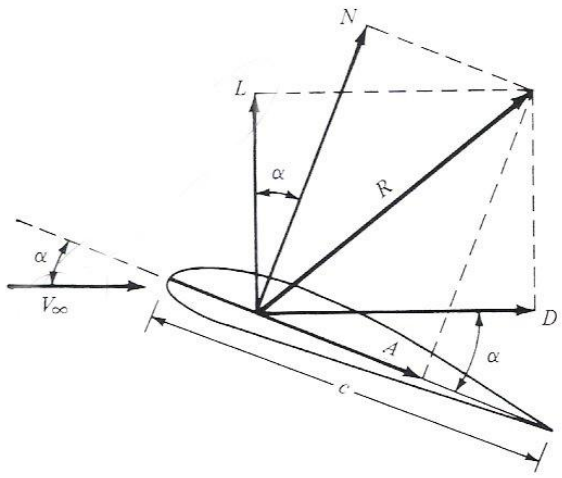

Fig. 2-18. Components of the resultant aerodynamic force.

Here, normal force, N, is the component of R perpendicular to chord, c. Axial force, A, is the component of R parallel to c. Lift, L, is the component of R perpendicular to free stream velocity, V_∞, and drag, D, the component of R parallel to V_∞.

The relation between these two sets of components can be expressed by using the angle of attack, α, that is defined as angle between c and V_∞. The relation is given by Eq. (2.29).

$$\left.\begin{aligned} L &= N\cos(\alpha) + A\sin(\alpha) \\ D &= N\sin(\alpha) - A\cos(\alpha) \end{aligned}\right\} \tag{2.29}$$

According to the well-known experiment with a spinning cylinder, vortex is created by the spinning motion. When this vortex is added to the steady flow, it creates a lift force

that acts on the cylinder. This is called the Magnus Effect. According to physics, the airfoil needs certain velocity and certain angle of attack in order to have lift. At that certain angle of attack, the fluid particles would go faster over the upper surface than over the lower surface. When this happens, the bound vortex is created, which is equivalent to the vortex created by the spinning cylinder. Bound vortex is due to the similar boundary layer laws described earlier. Bound vortex is called so because it is bound to a permanent location in a flow.

Lift can also be explained in a slightly different way using Newtonian mechanics. When the air goes past the body such as an airfoil, it causes the air to change the direction of flow. This change in direction causes the change of momentum. Force is the rate of the momentum change, and, therefore, there is a force acting on the wing, and so there must be another force that counteracts it – the wing pushes down and the air pushes up. This explanation of lift is viable, but it doesn‟t describe the importance of a boundary layer and viscosity, and, therefore, is omitted here.

The above described aerodynamic principles are similar for the fixed wing and for the bird‟s flapping motion. Here, the aerodynamics review continues with explanation of the three-dimensional process on the fixed wing. When the flow over an airfoil starts, strong vorticity develops at the trailing edge of the wing due to velocity gradients. Vorticity is a vector quantity, and it equals to twice the angular velocity of a fluid particle. It is given by Eq. (2.30).

$$\boldsymbol{\zeta} = 2\boldsymbol{\omega} = curl\, \boldsymbol{V} = \boldsymbol{\nabla} \times \boldsymbol{V} \tag{2.30}$$

Where $\boldsymbol{\zeta}$ is the vorticity vector, $\boldsymbol{\omega}$ is the rotation vector, and $\boldsymbol{V}$ is the velocity vector. This initial vorticity causes the starting vortex that has the counterclockwise circulation. Starting vortex is shown in Fig. 2-19 [4].

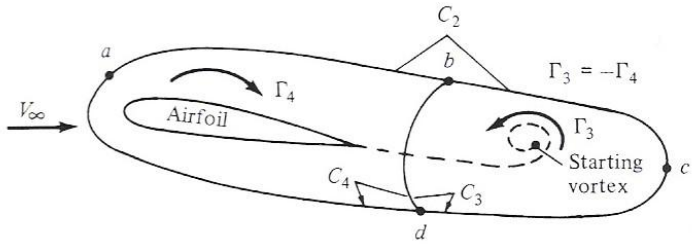

Fig. 2-19. Creation of the starting vortex.

Then the bound vortex, which has clockwise circulation, forms around the leading edge of the wing. According to Helmhotz‟s laws, once the vortex starts, it cannot end in the fluid, and, thus, bound vortex bends around the tip of the wing, and then sheds from the trailing edge and becomes trailing vortex. The system of bound vortex over the leading edge and resulting two trailing vortices is called horseshoe vortex. The horseshoe vortex is shown in Fig. 2-20 [75].

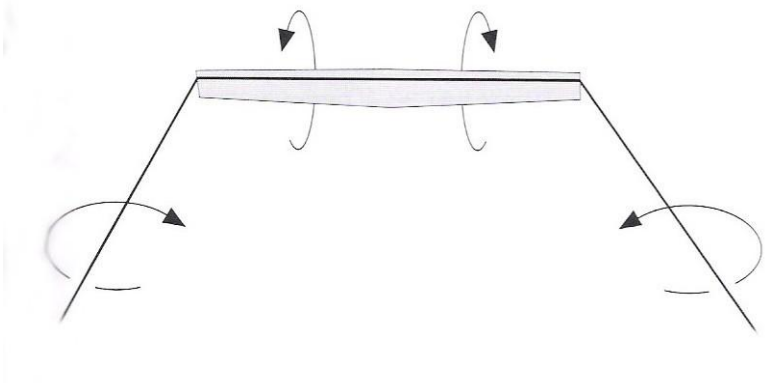

Fig. 2-20. Horseshoe vortex as the system of bound and two free trailing vortices.

After the initiation of the flow, starting vortex acquires the strength that is equal to the strength of the bound vortex. The equilibrium between starting and bound vortices allows the smooth flow from the trailing edge and the steady circulation around the airfoil.

According to the fixed wing classical theory, trailing vortices that have the same strength as the bound vortex cause a downward component of velocity that is called downwash. Figure 2-21 shows a cross-section of the trailing wake [75].

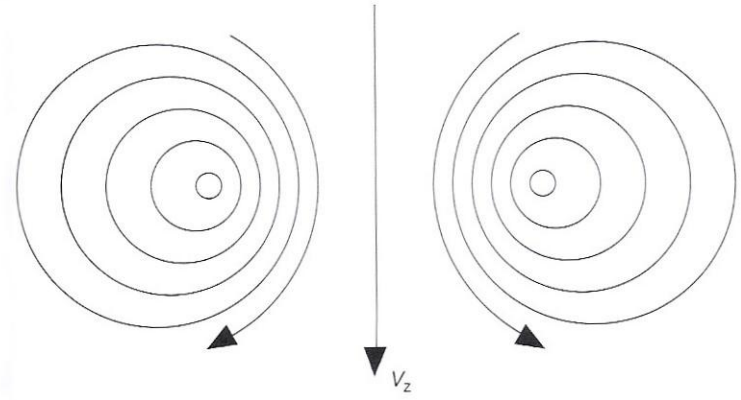

Fig. 2-21. A cross-section of the trailing wake.

Downwash, V_z, is a cumulative velocity, whose strength is larger than the strength of tangential component of velocity from each separate vortex. Downwash merges with the free stream velocity, V_∞, and this causes freestream velocity to deflect downward. This deflected freestream becomes local relative wind. Figure 2-22 shows the effect of downwash on the local flow over a local airfoil section [4].

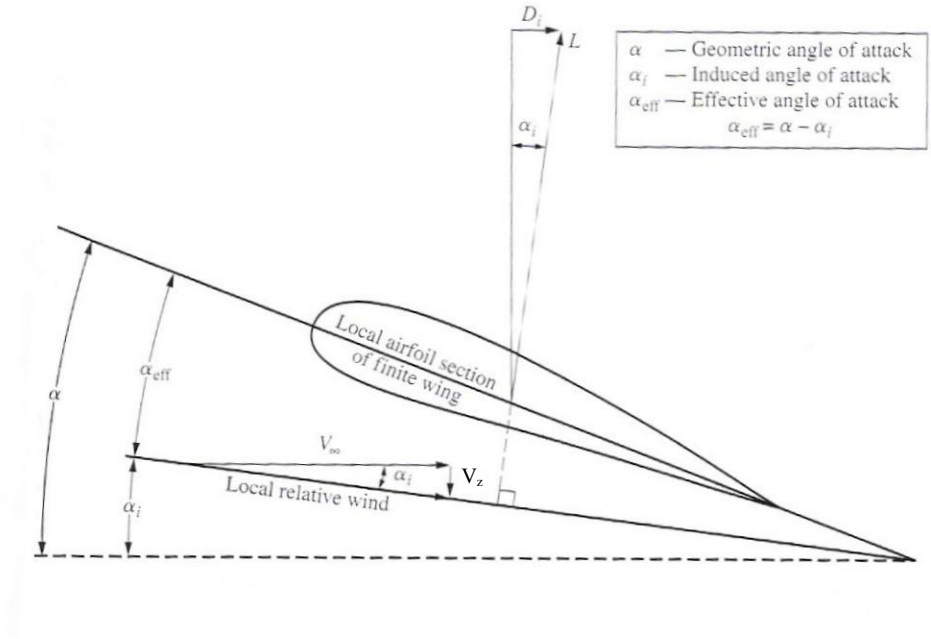

Fig. 2-22. Effect of downwash on the local flow over a local airfoil section.

In Fig. 2-22, α is the geometric angle of attack, α_i is the induced angle of attack, and α_{eff} is the effective angle of attack. Downwash has two important consequences on local airfoil section. First, due to downwash, local airfoil section actually sees a smaller angle than α, it sees α_{eff}. Second, due to downwash, local lift is not perpendicular to V_∞, but rather to local relative velocity. Local lift, L, is inclined from the vertical line by α_i. Thus, there is a component of local lift in the direction of V_∞. This component of local lift is called induced drag, D_i. Coefficient of induced drag is given by Eq. (2.31) [17].

$$C_{D_i} = \frac{{C_L}^2}{\pi(\mathcal{AR})} \tag{2.31}$$

Here, $\mathcal{AR}$ is the aspect ratio that equals to the ratio of the wing length to the chord length, and C_L is the lift coefficient.

There are two other types of drag that affect the performance of flight. They are skin friction drag, D_f, and pressure drag (or form drag), D_p. These types of drag force occur due to the act of air viscosity. In particular, skin friction drag is due to shear stress that acts on the surface, and equals to the component of the integral of the shear stress over the body in the drag direction. Skin friction drag in two-dimension is given by Eq. (2.32) [4].

$$D_f' = \int_{LE}^{TE} (\tau_{upper} \cos\theta) ds_{upper} + \int_{LE}^{TE} (\tau_{lower} \cos\theta) ds_{lower} \tag{2.32}$$

In Eq.(2.32), TE stands for trailing edge, LE stands for leading edge, τ_{upper} is the shear stress on the upper surface, τ_{lower} is the shear stress on the lower surface, and θ is the angle between shear stress that acts tangential to the surface and the horizontal.

For low Reynolds numbers, *i.e.* for laminar flows, the skin friction drag on an airfoil is approximated to the skin friction drag over the flat plate at zero angle of attack. The two-dimensional skin friction drag coefficient, c_f, is given by Eq. (2.33) [4].

$$c_f = \frac{1.328}{\sqrt{Re_c}} \tag{2.33}$$

Here, Re_c is the Reynolds number based on the chord length, c, and is given by Eq. (2.34).

$$Re_c = \frac{\rho_\infty V_\infty c}{\mu_\infty} \tag{2.34}$$

Here, ρ_∞ is the freestream density, V_∞ is the freestream velocity, and μ_∞ is the freestream dynamic viscosity. Figure 2-23 shows skin friction drag over a flat plate [4].

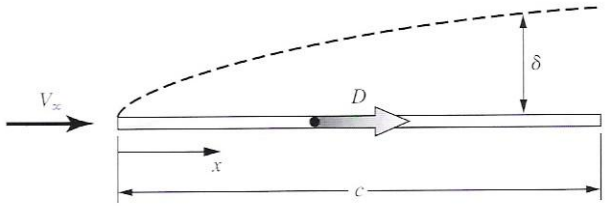

Fig. 2-23. Friction drag over a flat plate.

Drag force is given by Eq. (2.35).

$$D' = c_D \left(\frac{1}{2}\rho_\infty {V_\infty}^2\right) c = c_D(q_\infty)c \tag{2.35}$$

Here, c_D is the drag coefficient, ρ_∞ is the freestream density, V_∞ is the freestream velocity, q_∞ is so-called dynamic pressure, and c is the cord length.

Substituting Eqs. (2.33) and (2.34) into Eq.(2.35) gives skin friction drag force as shown in Eq. (2.36).

$$D'_f = c_f \left(\frac{1}{2}\rho_\infty {V_\infty}^2\right) c = c_f q_\infty c \tag{2.36}$$

Pressure drag is due to flow separation. On the upper surface of the wing, flow with low pressure prevails. At the trailing edge, flow from upper surface meets with flow from lower surface. This causes the upper surface pressure to increase. This increasing change in pressure in the direction of the flow is called adverse pressure gradient. Fluid particle in the boundary layer travels through this increasing pressure region and loses kinetic energy. Thus, its velocity decreases and eventually becomes zero or even may become negative, which would cause the particle to move in the opposite direction. At the point where velocity becomes zero, separation of the boundary layer from the surface occurs, which creates a swirling wake downstream. Flow separation results in increased pressure drag and loss of lift. Figure 2-24 shows flow separation caused by adverse pressure gradient [4].

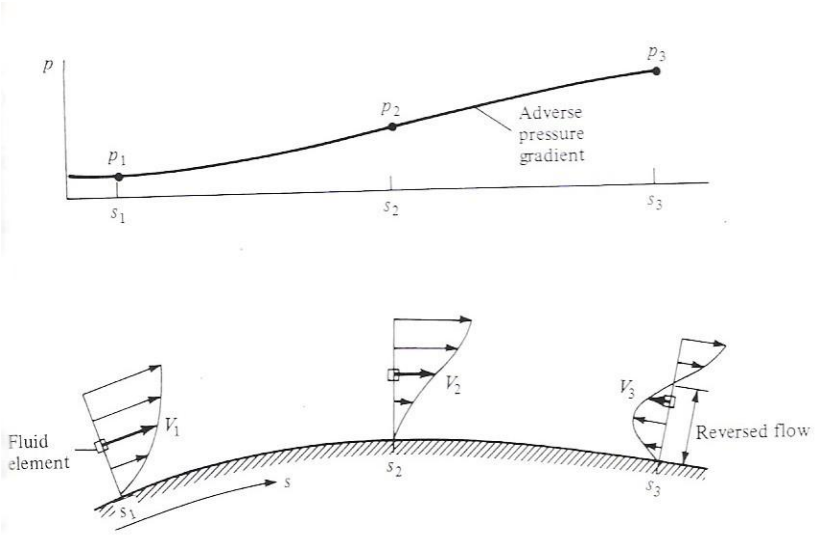

Fig. 2-24. Flow separation caused by adverse pressure gradient.

Pressure drag equals to the component of the integral of the pressure distribution over the body in the drag direction. Skin friction drag in two-dimension is given by Eq. (2.37) [4].

$$D'_p = \int_{LE}^{TE} (-p_{upper} \sin\theta) ds_{upper} + \int_{LE}^{TE} (p_{lower} \sin\theta) ds_{lower} \quad (2.37)$$

In Eq. (2.37), TE stands for trailing edge, LE stands for leading edge, p_{upper} is the pressure on the upper surface, p_{lower} is the pressure on the lower surface, and θ is the angle between pressure that acts perpendicular to the surface and the vertical.

Therefore, there are three drag components that contribute to the total drag. For a two-dimensional body, total drag consists of frictional drag and pressure drag only. For a three-dimensional body, total drag is the sum of frictional, pressure, and induced drags. The extreme example of the action of all three types of drag is found when a plane stalls. At low velocity, the higher angle of attack is required to maintain lift, which causes the flow separation, which, in turn, causes increase in pressure drag, loss of lift, and increase induced drag with the friction drag already present.

2.2.4 Aerodynamics of the Forward Flight: Flapping Flight

Now, aerodynamics of the forward flapping flight is considered with respect to its similarities and differences with the fixed wing theory. Here, principal parameters of oscillating airfoil should be defined. Figure 2-25 shows the model of oscillating airfoil with corresponding parameters [5].

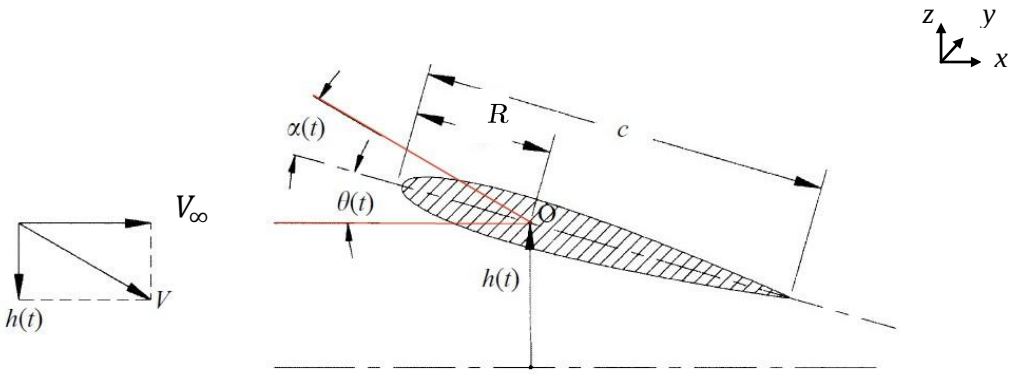

Fig. 2-25. Principal parameters of an oscillating airfoil.

Depicted airfoil is assumed to have three types of motion: forward motion, angular (or pitching) motion, and transverse (or heaving, or else plunging) motion. The airfoil is moving with constant forward velocity, V_∞ . It has harmonic angular motion about point O with angular displacement denoted as $\theta(t)$, displacement amplitude as θ_0, and angular velocity as ω. Harmonic transverse displacement is denoted as $h(t)$, transverse amplitude as h_0 (or earlier in Eq. 2.21 as h_a), and heaving frequency is the same as for angular motion, ω. The pitch motion has a phase lead, ψ, over the heave motion. The foil has chord length c, and point O is located distance R from the leading edge. Angle $\alpha(t)$ is effective or instantaneous angle of attack.

Here, clarifications should be made on the effective angle of attack. That angle is what the airfoil actually sees, but it is not necessarily the angle relative to horizontal. Figure 2.26(a) shows the geometric angle of attack, α, that is the sum of induced angle of attack, α_i, and effective angle of attack, α_{eff} [4]. Figure 2.26(b) shows usually sketched airfoil that is located at angle α_{eff} to the horizontal [5]. It"s obvious that α_{eff} in Fig. 2.26(b) is not the angle to the horizontal, but rather the angle to the local velocity vector, $V_{induced}$,

that is created by the sum of freestream velocity vector, V_∞, and downward component of the velocity, V_z, due to downwash. Therefore, caution should be exercised when considering geometric angle of attack or effective angle of attack.

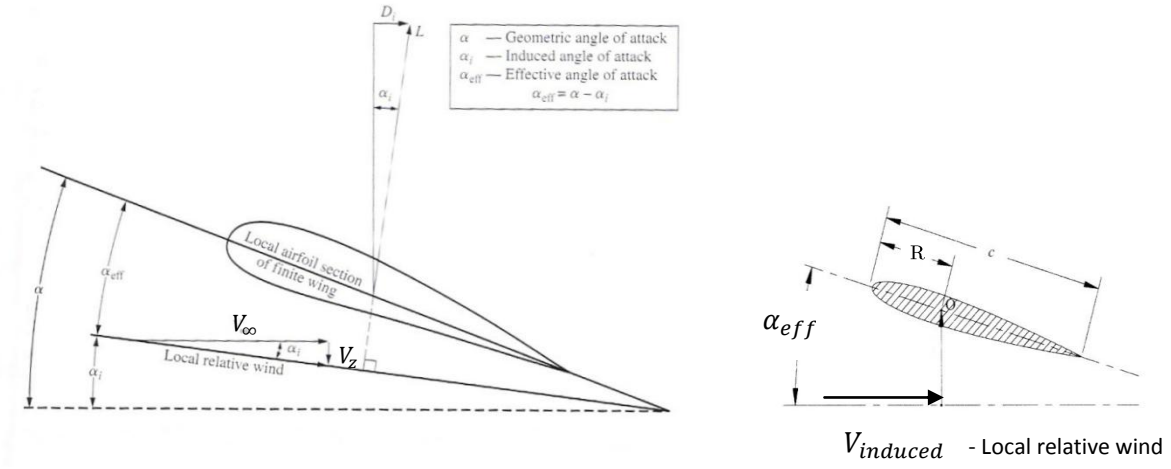

(a) (b)

Fig. 2-26. Distinction between geometric and effective angle of attack: (a) geometric, effective, and induced angles of attack; and (b) effective angle of attack.

Back to Fig. 2-25, the oscillating or flapping airfoil is under effect of time-varying forces $F_x(t)$ in the *x*-direction and $F_z(t)$ in the *z*-direction, and time-varying torque $Q(t)$. The *x*-direction is forward or thrust direction, and the *z*-direction is transverse or lift direction. The period of oscillation is represented by τ. Thus, the thrust force, T, is found by time-averaging the force $F_x(t)$ and is given by Eq. (2.38).

$$T = \frac{1}{\tau}\int_0^\tau F_x(t)dt \tag{2.38}$$

Dividing Eq. (2.38) by the wing span, b, we get thrust force per unit span given by Eq. (2.39).

$$T = \frac{1}{\tau b}\int_0^{\tau} F_x(t)dt \tag{2.39}$$

Average input power per cycle is found by adding the power required to produce lift force and power required for torque production. Power is given by Eq. (2.40).

$$P = \frac{1}{\tau}\int_0^{\tau}\left(F_z(t)\cdot V_z + Q(t)\cdot\dot{\theta}(t)\right)dt$$

$$= \frac{1}{\tau}\int_0^{\tau}\left(F_z(t)\cdot\frac{dh}{dt}(t) + Q(t)\cdot\frac{d\theta}{dt}(t)\right)dt \tag{2.40}$$

It‟s important to notice that under steady-state flapping conditions, integral of the second term is equal to zero, and Eq. (2.40) becomes the following Eq. (2.41):

$$P = \frac{1}{\tau}\int_0^{\tau} F_z(t)\cdot\frac{dh}{dt}(t)dt \tag{2.41}$$

By non-dimensionalizing Eq. (2.38) and Eq. (2.40), we obtain 3-D coefficient of thrust, c_T, and 3-D coefficient of power, c_P. They are given by Eqs. (2.42) and (2.43) respectively.

$$c_T = \frac{T}{\frac{1}{2}\rho {V_\infty}^2 S} = \frac{T}{qS} \tag{2.42}$$

$$c_P = \frac{P}{\frac{1}{2}\rho {V_\infty}^3 S} = \frac{P}{qV_\infty S} \tag{2.43}$$

In Eqs. (2.42) and (2.43), T is the thrust force, V_∞ is the forward velocity, ρ is the fluid density, and S is the reference area, which, for example for a rectangular wing, equals to the product of wing span, b, and chord, c.

Also, it‟s important to define the propulsive efficiency, η_P, which is the ratio of useful power over input power or, in other words, the ratio of thrust coefficient over the power coefficient. Propulsive efficiency is given by Eq. (2.44).

$$\eta_P = \frac{TV_\infty}{P} = \frac{c_T}{c_P} \tag{2.44}$$

In Eq. (2.44), thrust force, T, is taken from Eq. (2.38).

Hummingbirds and insects produce lift forces on both upstroke and downstroke. The difference between these two classes of fliers is the percentage of lift force generated at each component of the stroke. Hummingbirds generate 75 percent of lift on the upstroke and 25 percent on the downstroke; and insects generate lift force equally on upstroke and downstroke – 50/50 percent. Lift is just the component of the force the natural flier creates to propel itself through the air. Another component of that force that acts forward is a thrust force. According to Platzer [77], the force created by a wing that is decomposed into lift and thrust was first discovered by Knoller and Betz.

Alternatively, according to Platzer [77], aerodynamic forces, and, in particular, the thrust force can be calculated from the momentum of the air flow that is created by the wake. This was first explained by von Karman and Burgers [41]. According to Pennycuick [75], this method can be used only in theory, because it‟s very challenging to get reliable results. Nevertheless, observation of the wakes is much easier than calculation of forces,

and the thrust force can be „observed" from a reversed von Karman wake that carries the fluid momentum away from the wing, thus pushing the wing forward. A reverse von Karman wake is where vortices are along the opposite direction of a normal wake. Platzer [77] uses to relate the product of reduced frequency, *k*, and non-dimensional flapping amplitude, h , to the Strouhal (*St*) number as

$$kh = 2\pi(\frac{h_a}{A})St \tag{2.45}$$

where

$$h = \frac{h_a}{c} \tag{2.46}$$

In Eq. (2.45) and (2.46), h_a is the flapping or plunge amplitude, c is chord length, and A is the wake width.

Equation (2.45) relates a *pure* plunging or transverse motion to the *general* flapping motion. For a pure plunging motion that is uniform along the wing span, the wake width is $2h_a$, and, therefore, the ratio $\frac{h_a}{A}$ is $\frac{1}{2}$. Yet, for a flapping motion that is pivoted at one end as for birds and insects, the average length swept by a wing would be approximately half of that swept by the wing tip, so that the ratio $\frac{h_a}{A}$ is approximately $\frac{1}{4}$. Thus, Taylor"s finding of an optimal operating Strouhal number range of 0.2–0.4 (discussed earlier in Sec. 2.2.2) is equivalent to a kh range of 0.3–0.6 for a pure plunging motion.

At low *St* numbers, wakes that form normal Karman vortex street create drag, and, as *St* number increases, normal Karman vortex street turns into reversed Karman vortex street

that produces thrust force. Platzer [77] demonstrates the results for an airfoil that oscillates in the pure plunging motion presented in Fig. 2-27.

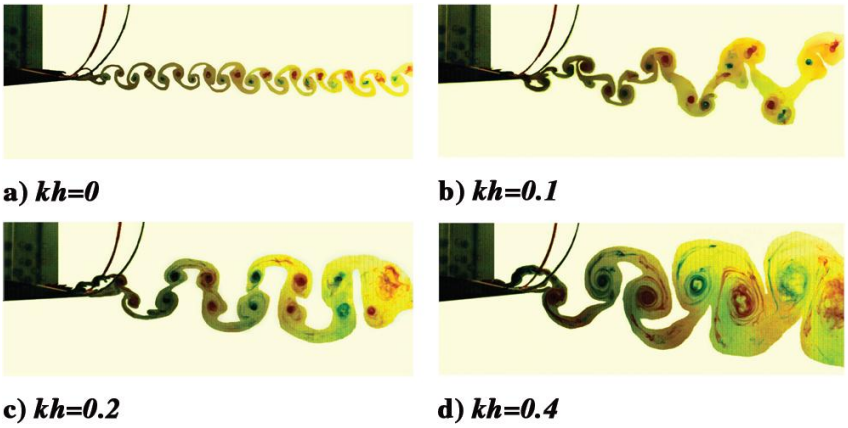

Fig. 2-27. Transition from normal to reversed Karman vortex street: (a) normal Karman vortex street; (b) and (c) transition; and (d) reversed Karman vortex street.

In Fig. 2-27, for a pure plunging motion, as kh[6] increases, the transition from normal to reversed Karman vortex street occurs. In Fig. 2-27(b) and Fig. 2-27(c), when transition occurs, shedding of the vortex pairs can be observed. The upper row of vortices is in the reverse Kármán vortex street, and their direction of rotation is counterclockwise. The lower row of vortices is in the normal Kármán vortex street, and their direction of rotation is clockwise. Apparently, flow is being caught between these two vortex rows, and, therefore, it creates a jet and, as a reaction, a thrust on the airfoil.

Dickson and Dickinson [19] investigated the forces in forward flight on a dynamically scaled robotic model of the fruit fly *Drosophila melanogaster*. They found that the tip velocity ratio, the ratio of the chordwise component of flow velocity at the tip caused by translation and revolution, is a more effective parameter than the advance ratio (given by

[6] In reference to Eq. (2.44), here, for pure plunging motion, $kh = 2\pi St$

Eqs. (2.22) and (2.23)). Also, the tip velocity ratio is useful for comparing forces during forward flight to forces during hovering flight. Another finding presented by the authors is that the force produced by the wing can be decomposed into two parts: an added mass force and a translational component.

As research on numerous numerical and experimental studies shows, the classical aerodynamic theory may not totally apply. It rather can serve as a tool to help to develop new theories that can explain the flapping flight by natural fliers.

2.2.5 Aerodynamics of the Hovering Flight

Although this research will focus on the forward flight, hovering is discussed in this section to give start to the following research. We describe different mechanisms that allow birds and insects to hover.

Due to low flight speeds, viscosity prevails in the flight mechanisms of birds, bats and insects. Nature fliers have different mechanisms that let them stay airborne. In 1973, Weis-Fohg published his experimental results on the flight of a small wasp Encarsia Formosa [114]. He found that the insect produced very large lift coefficient (2 or 3) at extremely low *Re* numbers (10-20). Such slow flight happens during hovering. However, Weis-Fogh flight mechanism is different from normal hovering. Normal hovering uses figure-eight motion where flip of the wings occurs at the top and the bottom of the figure eight. Weis-Fogh mechanism used clap, fling and flip motions to produce hovering. Normal hovering is used by hummingbirds, and Weis-Fogh hovering is used by smaller flies, such as small insects. Weis-Fogh mechanism was later explored by many researches.

Sohn and Chang [93], for example, studied clap-fling motion of Weis-Fogh mechanism, where as Maxworthy [58] compared the two types of hovering: normal and Weis-Fogh. Since Weis-Fogh mechanism is used by very small insects that use extremely low *Re* numbers, the more detailed discussion is going to be omitted and can be a focus of later research on hovering.

Another flying mechanism used by natural fliers is delayed stall mechanism. It is used primarily by larger insects, such as beetles, some birds, such as hummingbirds, and some bats. Delayed stall mechanism was proposed as an alternative to the quasi-steady Wes-Fogh mechanism that couldn"t account for all unsteady effects present in flight. According to Kim and Choi [42], delayed stall is described as

> *'When a wing starts suddenly from rest at an angle of attack larger that the stall angle, a large vertical vortex structure is generated at the leading edge of the wing, and this forceful leading-edge vortex increases lift until the vortex is shed from the wing'.*

Kim and Choi [42] state that initially delayed stall mechanism was verified experimentally on the model airplane wing; however, the research showed that lift improvement by the delayed stall did not continue after a few chord lengths of motion, and lift dropped after the leading-edge vortex (LEV) was shed. However, amazingly, natural fliers fly without any knowledge of physics. Kim and Choi [42] studied 2-D hovering mechanism and found that delayed stall had to go along with two other flight mechanisms that are responsible for supporting lift during stroke reversal. Previously proposed by Dickinson *et al.* [18], rotational circulation and wake capturing were found to be 2-D stabilizers for LEVs. Kim and Choi suggest that 3-D stabilizers, such as

spanwise flow and downwash, discovered by Ellington *et al.* [22] should also play important roles in stabilizing LEVs.

The 2-D study of Kim and Choi [42] was based on the previous finding of Wang *et al.* [111] that showed that 2-D computation can be used instead of 3-D computation without getting too much inconsistency in force calculation. Unsteady mechanisms of flapping flight generation can be studied by using 2-D simulation.

In summary, delayed stall mechanism of flight is due to the LEVs that provide greater circulation and, therefore, boost lift. However, LEVs can stay only for short duration, after which the lift drops unless there are no stabilizers. The LEVs‟ 2-D stabilizers are rotational circulation and wake capturing; and 3-D stabilizers – spanwise flow and downwash. Kim and Choi [42] also found that angle of attack (AOA) is directly connected with delayed stall; and the optimal AOA of producing maximal vertical force is the linear function of the stroke plane. Also, they found that shape of the wing cross-section is not important in the insect flight.

2.2.6 Unsteady Effects

As was mentioned earlier, different parts of bird wing may use different aerodynamics: arm wings use the conventional aerodynamic principles, such as attached flow, and hand wings use LEV and other unsteady aerodynamics to generate lift. Flight of birds as well as insects depends on unsteady aerodynamics. Unsteadiness comes from the following phenomena: flapping, changing wing morphology, viscous effects of the air, and possible winds. The first three categories are important for experimental settings, when unsteady

effects can be neglected, and quasi-steady aerodynamics can be used instead, and when unsteadiness plays a significant role in shaping flow over birds‟ wings and cannot be neglected.

There are a few unsteady effects that help birds and insects to stay aloft. They are all interrelated among themselves. However, in order to study the birds‟ flight, it‟s necessary to break down those effects and explain each of them. The most attention in the recent studies has been given to such effects as trailing edge vortices (TEV), leading edge vortices (LEV), suction effect, reversed Karman vortex street, delayed stall, and some others. These effects have been covered in earlier sections, and here, they are being summarized over.

Trailing Edge Vortices: (see also Sections 2.2.3 and 2.2.5)

Rayner [81] was among the earliest to propose that bird wings create circulation during downstroke only, and that the lift force equals to the ratio of the momentum of the vortex ring and wingbeat period. This assumption was tested by Spedding [96] who used the flow visualization particle image velocimetry (PIV) technique and showed that circulation is created during downstroke as well as during upstroke. In a different study [94], Spedding also showed that the tested bird needed only half of the momentum predicted by Rayner. Thus, it was shown that, during flapping flight, the bird produces a pair of continuous trailing vortices of constant strength – similarly, as described above, for the fixed wing. In particular, the wake produced by a bird in Spedding study [95] was similar to the one produced by the elliptically loaded airfoil of the same wing span. And, therefore, fixed wing theory was used to calculate lift coefficients and other efficiency

parameters. Figure 2.28 shows trailing vortices produced by a bird in Spedding‟s experiment [95].

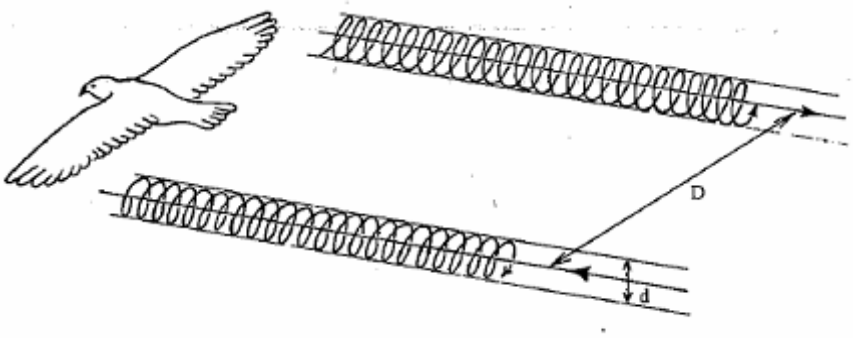

Fig. 2.28. Trailing vortices in a gliding kestrel experiment.

This type of trailing vortices is possible during the speedier flight. However, according to Pennycuick [75], at a slow speed, discrete vortex rings are observed during the upstroke. This is explained by the fact that, because the speed over the wing is so low during the upstroke, the circulation cannot be sustained. The vortex is shed from the wing in the form of a ring that can be explained by the Helmholt‟s second law that says that line vortex cannot disappear in the fluid and, in this case, should form a vortex ring. Figure 2.29(a) shows the observed phenomena of the formation of the vortex ring during the slow flight, and Fig. 2.29(b) shows the trailing vortices during the faster flight.

(a)

(b)

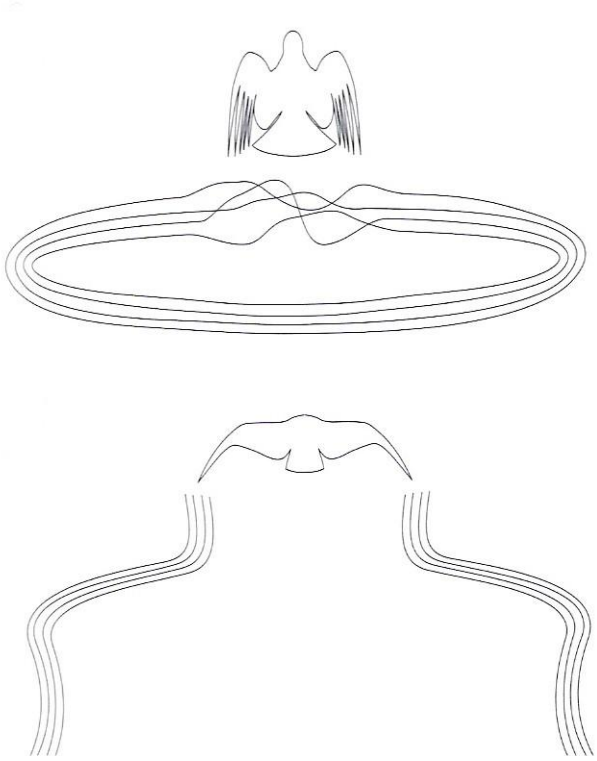

Fig. 2.29. (a) Vortex ring shed during slow flight; and (b) trailing vortices during faster flight.

According to the classical aerodynamic theory, the subsonic flow over airfoils is considered irrotational; vorticity is present only at the thin boundary layer immediately adjacent to the surface of the wing. From several studies that used particle image velocimetry (DPIV) technique to study the flow immediately downstream of the bird, Pennycuick [75] pointed out that there is vorticity beyond the boundary layer and, rather than being defined by the separate vortex filaments, it was distributed. Thus, these studies show that flow around the bird is not irrotational, which makes other calculations, such as force calculations, very difficult.

In comparison to the fixed wings, birds flex their wings during flight. And considering that the trailing vortices were of the same strength during upstroke and downstroke, the bird developed more lift during downstroke then during upstroke that produces the thrust force necessary to move the bird forward.

As learned from the kinematics study on hummingbirds, they do not really flex their wings due to the specifics of their skeletal structure of ball and socket joint. Ability to flex wings – sweeping them back – allows birds to use leading edge vortices to create high lift at lower speeds that is discussed next. Thus, hummingbirds should use some other nature-created „devices" to create lift and thrust forces during forward flight.

Leading Edge Vortices: (see also Sections 2.2.3 and 2.2.5)

Due to sharp leading edges, flow separation occurs and forms an attached vortex along the entire leading edge. This is the so-called leading edge vortex (LEV). Figure 2-30 shows the drawing of LEV on the wings of a swift in gliding flight [108]. LEVs are the main reason birds and insects can create high lift at low *Re* numbers over a wide range of angles of attack. Leading edge flow separation creates LEV that causes aerodynamic force normal to the wing chord. At high angles of attack, the drag component of this force is quite large. Many birds use swept-back wings during gliding flight. According to Pennycuick [71], the swept-back angle can fluctuate and is shown to be related to gliding speed. At high angles of attack, LEV on swept-back wings produces forces that allow safe landing, which requires high lift and high drag at low speeds.

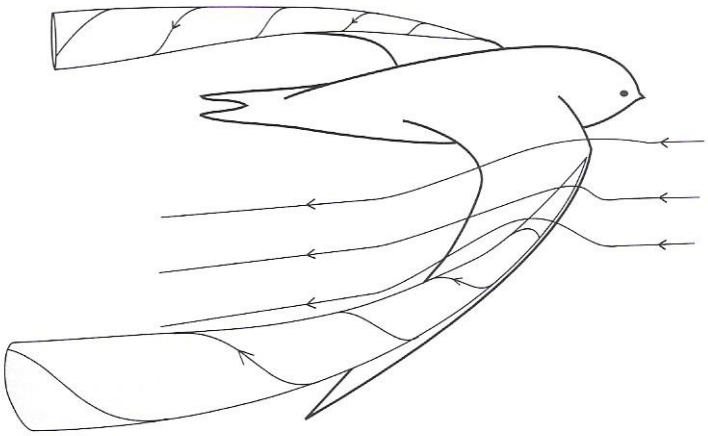

Fig. 2-30. Drawing of the LEV on the wings of a swift in gliding flight.

From Fig. 2-30, it can be seen that the LEV-system deflects the oncoming flow downward that produces downwash flow that generates lift. LEV separation starts at the wing wrist, and then follows the length of the wing almost to the tip while going slightly inward and up. The LEV core diameter, the LEV strength, and the maximum downwash flow velocity increase from wrist to the tip. LEV, as shown, has a conical shape.

After detaching from the wing tip, LEV generates two trailing vortices that become part of the wake behind a bird. These TEVs are not distinguishable from the TEVs generated by the wing tip produced by a conventional attached flow that acts on the wings. This happens because both vortices have the same rotational sense. That is the reason why the studies of the flow in the wake behind a bird are not suitable to determine the lift generating mechanism used by the wings as discussed earlier in Sec. 2.2.4. Figure 2-31 shows the flow patterns due to LEVs at different *Re* numbers [86].

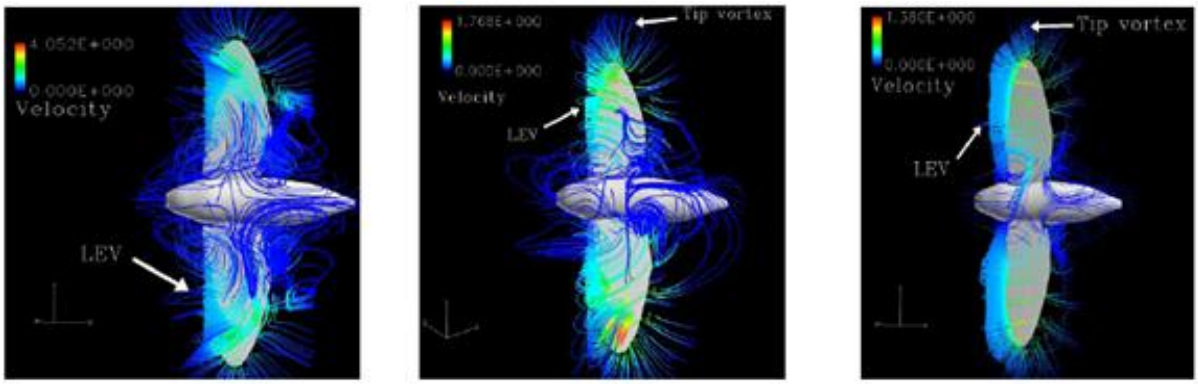

(a) *Re*=6000 (b) *Re*=120 (c) *Re*=10

Fig. 2-31. Streamlines and vorticity patterns associated with LEVs at various Reynolds numbers.

From Fig. 2-31, it can be seen that the higher is the *Re* number, the greater is the vorticity of the flow around the wing.

In some birds, such as hummingbirds, LEVs are present; however, they are not sustained [113]. In other birds, LEVs are sustained. One reason for this difference was explained earlier – the ability to sweep wings. However, what happens when a bird sweeps its wings was not explained. Liu [54] explains that axial flow generated by a spanwise pressure gradient is the stabilizing mechanism in the leading edge vortex sustainability.

Suction Effect:

For thin airfoils in inviscid conditions, flow does not separate around the leading edge. This results in „leading-edge suction" – an extremely low pressure that occurs due to the large change in velocity required for flow around the leading edge. According to

Polhamus [78], LE suction creates part of the lift force that is estimated from the potential flow lifting-surface theory with Kutta condition at the trailing edge. The other part of the lift, described in the next paragraph, is equal to the force necessary to maintain the balance of the potential-type flow around the spiral vortex. Figure 2-32(a) shows a suction vector ($\mathbf{F}_S$) that acts parallel to the chord and sums with the normal force ($\mathbf{F}_N$) to produce the total lift ($\mathbf{L}$) [16].

For thin airfoils in viscid conditions and at high angles of attack, flow separates from the leading edge, and leading-edge vortex develops that cancels the leading-edge suction [107]. However, to maintain lift, a normal suction force is required to keep the vortex attached on the upper surface of the airfoil. This change in pressure distribution is analogous to 90° rotation of the leading edge suction vector shown in Fig. 2-32(b) [16].

(a)

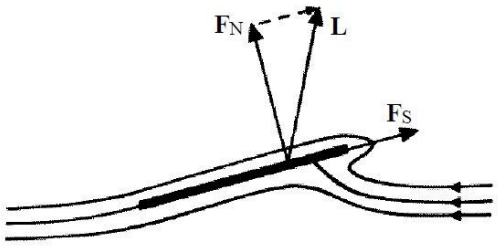

(b)

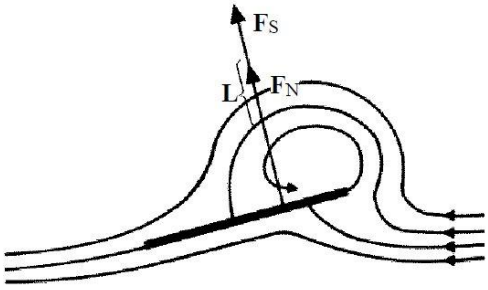

Fig. 2-32. (a) Inviscid conditions: attached flow causes leading-edge suction; (b) viscid conditions: formation of leading-edge vortex causes cancelling leading-edge suction effect.

Reversed Karman Vortex Street: (see also Section 2.2.4)

As mentioned in Sec. 2.2.2, the reduced frequency and its reciprocal, advanced ratio, are the non-dimensional parameters that give indication on importance of unsteady effects. Wang [110] suggested that the flapping frequency could be an indicator of the unsteady aerodynamics. As explained earlier, wakes produced at lower flapping frequencies form drag-producing Karman vortex street. As the flapping frequency increases, wakes form into a thrust-producing reversed Karman vortex street. This effect of producing thrust at higher plunging velocities is called Knoller-Betz [46, 106, 117] (or Katzmayer [67]) effect.

There are different types of wakes that can occur behind flapping wings. Depending on the flapping frequency, merging of leading and trailing edge vortices can produce three types of wakes: von Karman at lowest range, deflected at middle range, and reverse von Karman at highest range of flapping frequencies [46, 47]. The deflected wake occurs when vortices shed from the trailing edge interact nonlinearly. When leading and trailing edge vortices do not merge, the wake is either dissipated or neutral. Hedenström *et al.* [34, 97] conducted PIV experiments on bird wakes. This paper lists some parameters used in the study, specifically the reduced frequency, forward velocity, flapping frequency, and chord length.

Delayed Stall: (see also Section 2.2.5)

In the early twentieth century, experimental work was done to measure the transient lift on a stalled airfoil [112]. It was found that its maximum value was about twice higher

than the maximum steady state value. This short increase in lift is related to the formation of the leading-edge vortex on the upper surface of the wing before it rolls off, a phenomenon known as the delayed stall or dynamic stall. Delayed stall is used by some large insects, birds and bats.

Other Unsteady Aerodynamic Mechanisms:

Delayed stall is associated with other unsteady aerodynamic mechanisms, such as rotational lift and wake capture. These mechanisms were studied experimentally and numerically by Nagai *et al.* [63]. Sane and Dickinson [84] also covered the above mechanisms in their study on influences of wing kinematics on the production of unsteady aerodynamic forces in insect flight.

Among other unsteady mechanisms, there is a clap and fling mechanism (also called the Weis-Fogh mechanism) [61], as discussed in Sec. 2.2.5. This mechanism is usually utilized by small insects, such as butterflies, that fly at lower *Re* up to 100. At higher *Re* , this mechanism loses its effectiveness, and, therefore is not suited for MAV design. Another point about the clap and fling mechanism as well as rotational lift and wake capture mechanisms is that available research usually attributes the above mechanisms to the insect flight and not much for the bird flight.

2.3 Kinematics of Flapping Flight

Wing-stroke kinematics of birds and insects is usually divided into translational and rotational phases. Translational phase consists of upstroke and downstroke. Rotational phase consists of pronation and supination. Pronation happens before the downstroke, and supination happens before the upstroke. In case with mechanical experimental devices, if the wing is rigid, it"s hard to achieve pronation or supination because of it.

Birds" and insects" flight kinematics is quite different from kinematics of man-made machines. Quite a lot of studies exist that cover kinematics of avian and insect flight. Some of them are done on real fliers, some on the modeled ones, and some done numerically. One particular biological research done by Tobalske *et al.* [103] studied three-dimensional kinematics of the Rufous hummingbird (*Selasphorus Rufus).* The study provides some important kinematical parameters. Those parameters along with other added kinematical parameters are explained in Figs.2-33 [103], 2-7, 2-25, and 2-26 and are listed in Table 2-2. The paper gives a greater understanding of a bird"s motions during flight and can serve as a means to compare kinematics of a mechanically created bird with kinematics of a real hummingbird.

(a)

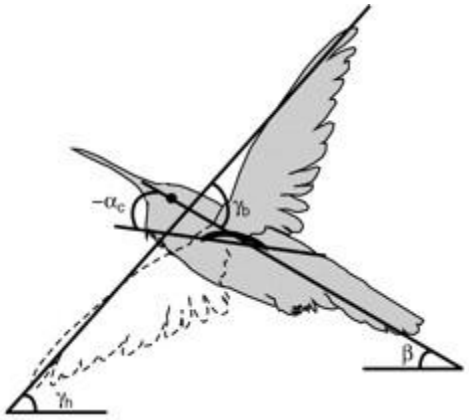

(b)

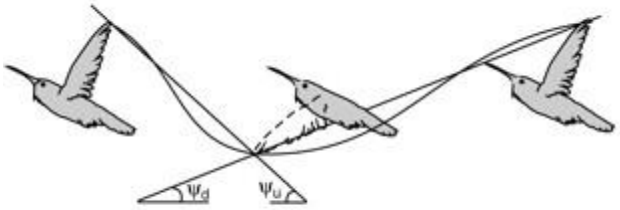

(c)

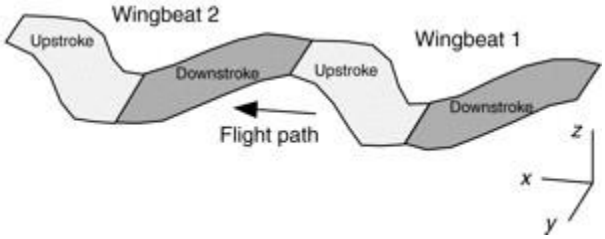

Fig. 2-33. Angles and areas measured from wing and body motion of Rufous hummingbirds during flight: (a) α_c is the chord angle relative to the body, β is the body angle relative to horizontal, γ_b is the anatomical stroke-plane angle relative to the body, and γ_h is the tracking stroke-plane angle relative to horizontal; (b) ψ_d and ψ_u are global stroke-plane angles during downstroke and upstroke; (c) global stroke-plane area is outlined by the wingtips for each wing beat: downstroke – dark gray and upstroke – light gray.

Table 2.2. Kinematic parameters for flapping flight.

Parameter	Explanation	Notes
α	Geometric angle of attack relative to horizontal	See Fig. 2-26
α_{eff}	Effective angle of attack – angle to the local velocity vector, $V_{induced}$	$\alpha_{eff} = \alpha - \alpha_i$ See Fig. 2-26
α_i	Induced angle of attack relative to horizontal	$\alpha_i = tan^{-1}(V_Z/V_\infty)$ See Fig. 2-26
α_c	Chord angle relative to the bird‟s body	Fig. 2-32 (a)
β	Body angle relative to horizontal	Fig. 2-32 (a)
γ_b	Anatomical stroke-plane[7] angle relative to the body	Fig. 2-32 (a)
γ_h	Tracking stroke-plane angle relative to horizontal	Fig. 2-32 (a)
ψ_d	Global downstroke-plane angle relative to horizontal	Fig. 2-32 (b)
ψ_u	Global upstroke-plane angle relative to horizontal	Fig. 2-32 (b)
h_a	Wing beat amplitude or heaving, or flapping, or plunging amplitude	
b	Wing span	Fig. 2-7
c	Mean wing chord	Fig. 2-7
$\mathcal{AR}$	Aspect ratio	$\mathcal{AR} = b/c$
τ	Wing beat period, or period of oscillation	
l	Wing length	$l = b/2$
f	Wing beat frequency	$f = 1/\tau$

[7] Stroke plane is defined by three points located on the wing base, on the wingtip at maximum, and on the wingtip minimum angular position. During hovering, the stroke plane is located near horizontal, and, during forward flight, the stroke plane is located near vertical.

V_∞	Forward or free stream velocity	
V_Z	Downward component of the velocity due to downwash.	See Fig. 2-26
$V_i \; or \; V_{induced}$	Induced velocity or local wind to the wing - the sum of free stream velocity vector, V_∞, and downward component of the velocity, V_z, due to downwash.	See Fig. 2-26
ω	Angular pitching/plunging velocity with respect to the body.	$\omega = 2\pi f$ See Fig. 2-25
V_{PITCH}	Linear pitching velocity of the wing with respect to the body. (It would be more appropriate to multiply angular velocity by distance *R*, and not the chord distance, since distance *R* is from the center point of pivoting, as shown in Fig. 2-24. However, published sources [112] list chord as distance; therefore, it will be used here.)	$V_{PITCH} = \omega c$ See Fig. 2-26
$V_{PLUNGE} = = V_{tip}$	Linear plunge velocity or tip velocity	$V_{PLUNGE} = 2\, h_a f l$ See Fig. 2-26
k	Reduced frequency ratio	$k = {}^{V_{PLUNGE}}/_{V_\infty}$
J	Advanced ratio	$J = {}^{1}/_{k}$

For reference and comparison purposes, it would be useful to have a few figures on some angles of attack. In particular, Fig. 2-34 shows the global stroke-plane angles: ψ_d – during downstroke, and ψ_u- during upstroke. Referencing to Fig. 2-33(b), we see that, as velocity increases, there is a great change in stroke angle during upstroke, and there almost no change during downstroke.

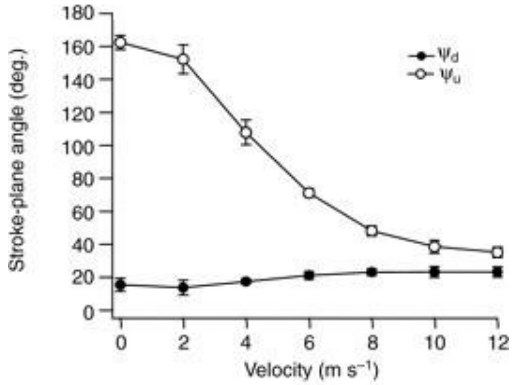

Fig. 2-34. Global stroke-plane angles for different velocities: ψ_d – during downstroke, and ψ_u – during upstroke.

Therefore, from Fig. 2-34, we see that, during hovering and slower speed flight, kinematics and aerodynamics of the upstroke and downstroke are not symmetrical. According to Tobalske *et al*. [103], for hovering hummingbirds, wake measurements indicate that about 75 percent of the weight support is provided during downstroke, and only 25 percent during upstroke.

Figure 2-35 shows the angle of attack at mid-downstroke and mid-upstroke for the range of velocities from zero to twelve meters per second.

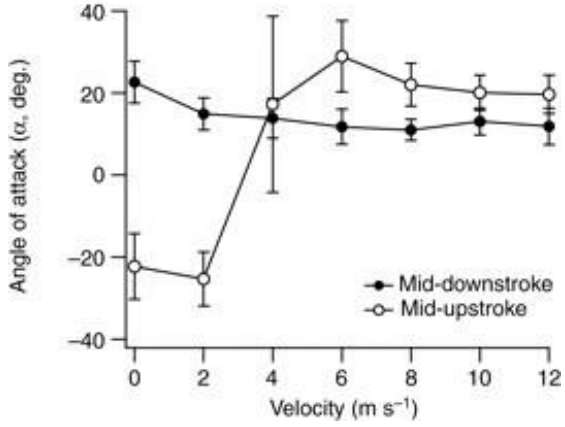

Fig. 2-35. Angle of attack α for different velocities.

Similar to Fig. 2-34, Fig. 2-35 shows that, during downstroke, the angle of attack does not change too much with velocity, just slightly at hovering. However, during upstroke, the angle of attack has slight drop at two meters per second, and then has steep rise between two and six meters per second, and, finally, it becomes somewhat stable after six meters per second. Once again, we see that, at slower speeds, the kinematics is not symmetrical during upstroke and downstroke.

Figure 2-36 shows some other kinematic parameters of the hummingbird flight, including the wing beat frequency given in Hertz and the amplitude given in degrees at different velocities.

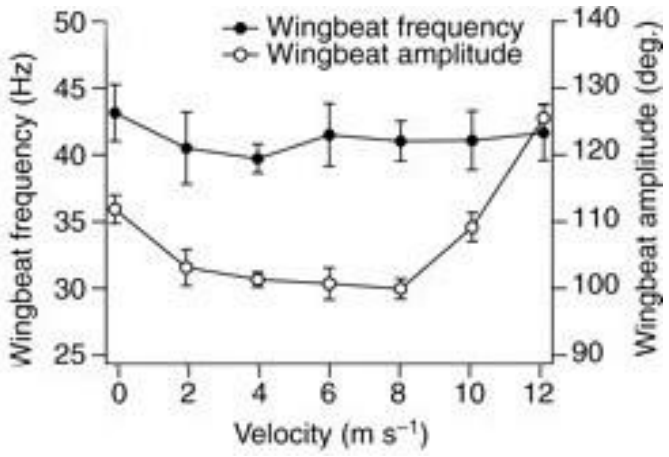

Fig. 2-36. Wing beat frequency (Hz) and wing beat amplitude (degrees) of the Rufous hummingbird flight for different velocities.

It can be noticed from Fig. 2-36 that the wing beat frequency is almost independent of velocity. However, the amplitude does depend on velocity.

Figure 2-37 shows an average angular velocity of the wing during downstroke and upstroke at different velocities.

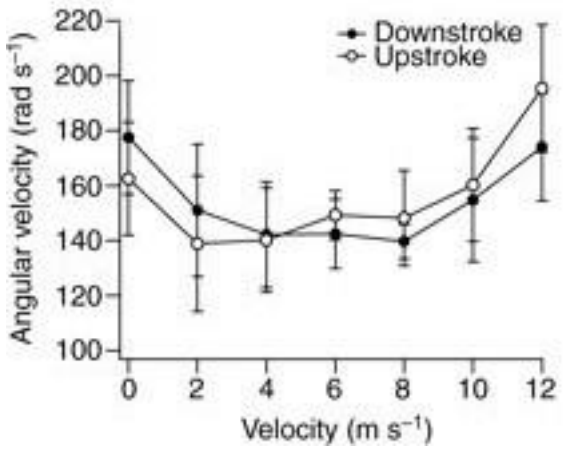

Fig. 2-37. Average angular velocity of the wing of the Rufous hummingbird during downstroke and upstroke at different velocities.

Figure 2-37 shows that, in general, angular velocities during upstroke and downstroke do not differ too much from each other. However, looking in details, during low velocities range, angular velocity values were smaller during upstroke than during downstroke. At four meters per second, values of the angular velocity of the wing during the upstroke became larger than those during the downstroke.

Tobalske *et al.* [103] also present other results, such as displacements of the hummingbird wingtip and wrist at different velocities in two projections – dorsal and lateral. Overall, results of experimental work done on real birds can be used as great references for the comparison of the kinematics of real and mechanical birds.

Frampton *et al*. [24] studied the conditions – bending and twisting of the wing – for generation of optimal thrust. Their results showed that the phase angle between bending

motion and torsional motion is critical for the production of thrust. It was found that, when bending and twisting are in phase, it results in the largest thrust; whereas, when twisting lagging bending by 90 degrees, it results in the best efficiency.

Greenewalt [29] studied the kinematics of the hummingbird, and some results of his study are presented in Fig. 2-38. It shows the wing pattern during forward flight at different speeds as well as during hovering and backward flight. The projection given is in the lateral view. Here we see that, as the speed decreases, the vertical loop progressively becomes horizontal, and, during zero velocity, horizontal loop becomes „figure-8" motion.

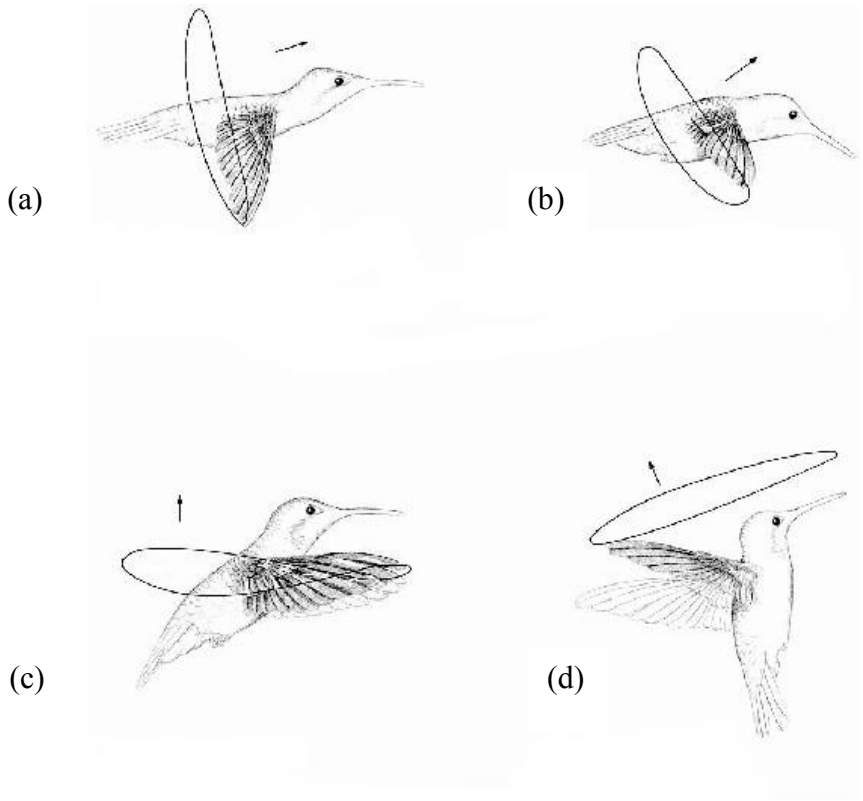

Fig. 2-38. Hummingbird wing patterns: (a) forward flight at top speed, 26 miles per hour; (b) forward flight, 8.6 miles per hour; (c) hovering; (d) backward flight.

Another interesting study performed by Liu *et al.* [55] was done on larger birds - seagull, merganser, teal, and owl. Wing geometry was measured using a three-dimensional laser scanner, and videos of the flying birds were made. That allowed authors to express wing kinematics, specifically the three characteristic angles, in the Fourier series as a function of time. The authors claim that their method of obtaining wing kinematics can help computationally generate the aerodynamic study of flapping flight.

Kinematics of bird flight is a very broad topic. Here, the effort was made to gather as much information on kinematics of the hummingbird flight. Next figures present some information on hummingbirds in relation to other flying creatures. Figure 2-39 represents a graph from Greenewalt [29] that shows the total weight given in milligrams versus the wing length given in millimeters. Interestingly, hummingbirds are represented separately from other birds and are also separate from insects. According to the author, the dotted long line shows the trend among all flying creatures. The scale is logarithmic, and the general trend line has a slope of about three that indicates that the total weight is proportional to the wing length cubed and is presented as follows:

$$Total\ Weight = (Wing\ Length)^3 \tag{2.47}$$

It can be seen that hummingbirds are located somewhere in the middle of the general trend with their own distinguished separate trend line. The slope of this line is larger than the slope of the general trend line, which means that the relation shown by Eq. (2.47) doesn‟t necessarily work for hummingbirds, whose trend looks more like exponential.

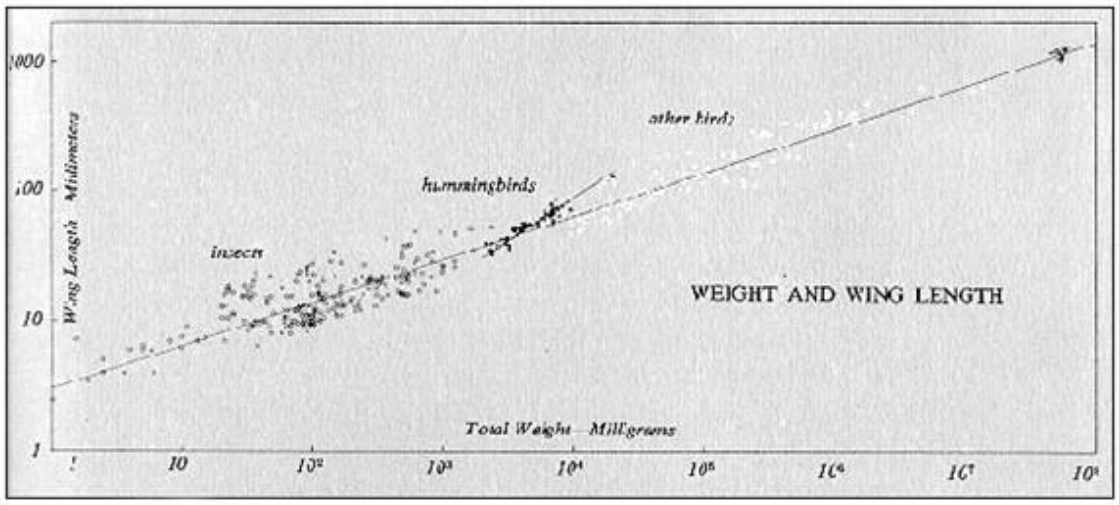

Fig. 2-39. Flying creatures: total weight vs. wing length.

Figure 2-40 also represents a graph from Greenewalt [29] that shows the wing length given in millimeters versus the wing beat rate given in cycles per second. Similar to Fig. 2-39, Fig. 2-40 shows a general trend line for flying creatures including insects, hummingbirds and other birds. The scale is logarithmic, and the slope of the given trend line is negative that indicates negative power coefficient.

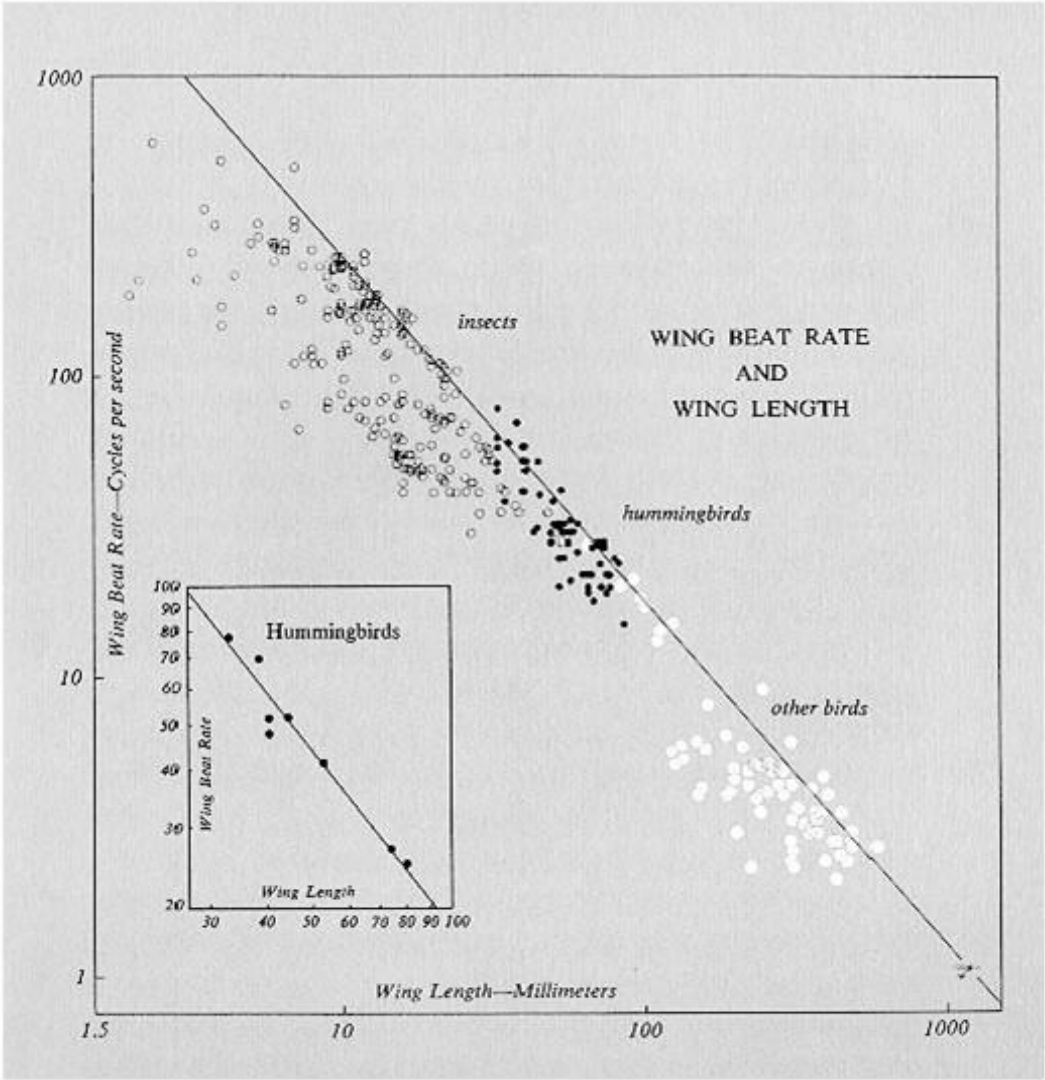

Fig. 2-40. Flying creatures: wing length vs. wing beat rate.

Similar to Fig. 2-39, hummingbirds on Fig. 2-40 are located between insects and other birds. Both Figs. 2-39 and 2-40 show general trends and give an overview of hummingbirds in comparison to other flying creatures. Such biological observations can be useful in MAV design.

Figure 2-41 shows the Rufous hummingbird wing kinematics in dorsal and lateral projections [103]. Numbers from 0 to 12 next to each bird indicate velocity change that is given in meters per second.

(a)

(b)

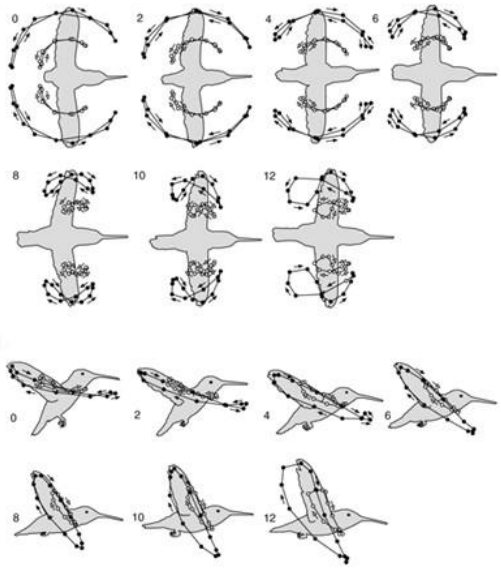

Fig. 2-41. (a) Dorsal projection at different velocities; (b) lateral projections at different velocities.

In particular, Figs. 2-41 (a) and (b) show wrists and wingtip paths for different velocities from different projections. It can be noticed that in dorsal view, as velocity increases, the downstroke path traces less the upstroke path. The „figure-8" motion can be seen on both projections. The difference is that in dorsal view „figure-8" motion becomes progressively noticed as velocity increases, and in lateral view, „figure-8" motion is apparently at the zero velocity when the bird is hovering.

2.4 Hummingbird in Flight

As a whole, Chapter 2 is dedicated to the review of the literature concerning with the bird and insect flight. However, after consideration of the biological literature, an effort was made to collect most of the available information on hummingbirds. The reasons were that hummingbirds fit the dimensions of MAVs; they are true hoverers; and the range of Reynolds numbers they fly fits better for the design of MAV with the given constraints. Below is tabulated information that, first, compares hummingbird‟s morphology and flight parameters to other species; and second, gives the comparison of various hummingbirds among themselves. Table 2-3 shows some morphological characteristics of bumblebee, hawkmoth, and hummingbird for comparison [87].

Table 2-3. Morphological and flight parameters of selected natural fliers.

Parameters	**Bumblebee** (Bombus terrestris)	**Hawkmoth** (Manduca sexta)	**Hummingbird** (Lampornis clemenciae)
Morphological parameters			
Total mass, [mg]	170	1600	8400
Wing mass (both wings), [mg]	0.9	90	600
Wing length, [mm]	13.2	48.5	85
Wing area, [mm^2]	100	1800	3500
Flight parameters			
Flapping frequency, [Hz]	150	25	25
Stroke amplitude, [rad]	2	2	2.5
Chord Reynolds number	1,200 - 3,000	5,000	10,000 - 15,000

As one can see, morphological parameters differ significantly in the expected order of the size of the flier. The hummingbird has the largest dimension that still fits the MAV criteria. Flight parameters show that the flapping frequency in forward flight is much higher for bumblebee than for hawkmoth and hummingbird, which have the same flapping frequency. The stroke amplitude does not vary too much among the given fliers. And, finally, Reynolds numbers vary significantly among the given fliers. *Re* is the largest for hummingbird, which means that inertia and viscous effects are rather equally important. Next, Table 2-4 expands the comparison of various fliers and gives overview of broader selection of parameters then Table 2-3. Table 2-4 shows morphological, flight,

scaling, and non-dimensional parameters of Chalcid Wasp, Fruit fly, Honeybee, Hawkmoth, and Rufous Hummingbird [88].

Table 2-4. Morphological, flight, scaling, and non-dimensional parameters of selected biological fliers.

Parameter	**Chalcid Wasp (*Encarsia formosa*)**	**Fruit fly (*Drosophila melanogaster*)**	**Honeybee (*Apis mellifica)***	**Hawkmoth (*Manduca sexta*)**	**Rufous Hummingbird (*Selasphorus rufus*)**
Mean chord length: [mm]	0.33	0.78	3.0	18.3	12
Semi-span: [mm]	0.70	2.39	10.0	48.3	54.5
Aspect ratio	4.24	6.12	6.65	5.3	9
Total mass:[g]	$2.6e^{-7}$	$0.96e^{-3}$	0.1	1.6	3.4
Flapping frequency:[Hz]	370	218	232.1	26.1	41
Flapping amplitude: [rad]	2.09	2.44	1.59	2.0	2.02
Mean wing tip velocity: [m/s]	1.08	2.54	7.38	5.04	8.66
Reynolds number	23	126	1412	5885	6628
Reduced frequency	0.355	0.212	0.297	0.296	0.172

Table 2-4 shows that hummingbird has a relatively large aspect ratio. Also, the mean chord length and the mean tip velocity are presented in Table 2-4. Finally, the reduced frequency parameter for hummingbird is less than 0.2 in comparison to other species

shown in Table 2-4. This tells (see Sec. 2.2.2) that the flow can be considered as quasi-steady. However, it can be noticed that data for Rufous hummingbird in Table 2-4 differs from the data given in Table 2-3. This means that reliability of certain conclusions cannot be certain, which indicates that more information is required to make aggregated judgment regarding hummingbird flight parameters. The following Table 2-5 shows the comparative morphology of four species of hummingbirds during hovering [9, 10, 79].

Table 2-5. Morphological and flight parameters of selected hummingbirds during hovering.

Parameters	**Hummingbird Species**			
	Blue-throated	Magnificent	Black-chinned	Rufous
Morphological parameters				
Body length [mm]	133	115	95	89
Wingspan [mm][8]	180	173	107	102
Wing length [mm]	85	79	47	42
Mass [g]	8.4	7.4	3	3.3
Wing shape	pointed	pointed	pointed	pointed
Aspect ratio	8.2	8.4	7.1	7.4
Flight parameters				
Mean tip velocity [m/s]	10.4	9.9	10.5	12.3
Flapping frequency [Hz]	23.3	24	51.2	51.7
Stroke amplitude [degree]	151	150	126	163
Stroke amplitude [rad]	2.63	2.61	2.2	2.84
Wing loading [N/m^2]	23.5	24.7	23.5	33.6
Reynolds number	11,400	9,800	7,400	7,400
Mean lift coefficient	1.46	1.67	1.42	1.41

[8] Approximated from the wing length.

Table 2-5 shows that flight speed does not vary across the represented birds. However, the flapping frequency seems to vary inversely with size. The stroke amplitude and the wing loading do not show any dependency on size. Reynolds number and lift coefficient appear to be in direct relation with size. It is interesting to note that, while hovering, one may assume that the flight velocity is zero; however, as nature shows, it is not so. In general, Table 2-5 gives more information of morphological and flight parameters of the birds that represent the design interest.

Here is the summary on hummingbirds. They are the only birds that can hover for extended periods. They produce lift on both downstroke and upstroke. The downstroke produces 75% of the lift and the upstroke produces 25% in comparison to insects and other birds (see Fig. 2-42 [82]).

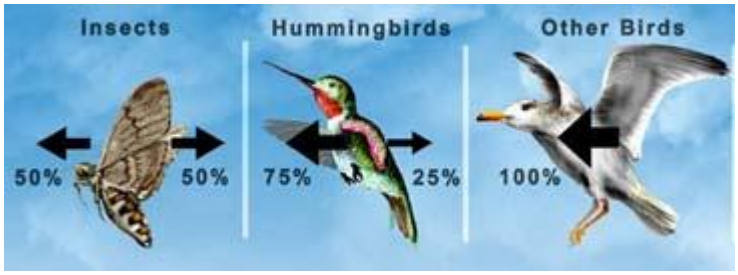

Fig. 2-42. Lift production on downstroke vs. upstroke in insects, hummingbirds, and birds.

Hummingbirds have an important similarity with insects – both groups produce leading edge vortices, and, therefore, experience delayed stall. Hummingbirds produce LEVs only during the downstroke, and then LEVs are shed at the transition to upstroke. Studies show that at low angles of attack hummingbirds produce lift to drag ratio of 8 to 16 [2]. This suggests that hummingbirds are extremely good at generating lift.

2.5 Flapping Flight as a Fluid-Structure Interaction Problem

This section describes the importance of aeroelasticity analysis and provides a brief overview of research done on aeroelastic analysis of flapping flight. Various forces, internal and external, act on a wing during the flight. The interactions among inertial, structural, and aerodynamic forces are nonlinear and complex. Analyzing bird‟s flight as a fluid-only problem is not going to provide adequate or even acceptable results. The problem should be addressed in a consistent way through aeroelastic studies.

Most of the previous work that can be associated with the MAV development is on rigid flapping wings and relates mostly to the insect flight. Insect wings have anisotropic quality in both chordwise and spanwise directions due to their membrane–vein pattern. The leading edge of their wing is usually reinforced. For most cases, the spanwise bending stiffness is about 1–2 orders of magnitude greater than the chordwise bending stiffness; and the spanwise flexural stiffness scales with the third power of the wing chord, while the chordwise stiffness scales with the second power of the wing chord [88].

Flexible wings allow for passive profile variation that has several advantages. First, flexible wings experience the delayed stall. As experiments showed [86], at low angles of attack, flexible wings perform like rigid wings with similar aspect ratio. As angle of attack increases, rigid wings stall between 12 and 15 degrees; and flexible wings experience delayed stall with stalling between 30 and 45 degrees, which, for rigid wings, is associated with much lower aspect ratio. The low aspect ratio means much lower lift. Therefore, flexible wings are capable of a greater aerodynamic performance than rigid wings: they stall like rigid wings with the aspect ratio between 0.5–1.0 and create lift like

rigid wings with the aspect ratio of 2.0. Second, flexible wings can adjust to the wind gust, which allow for a smoother flight platform. Third, it was also shown that, for a membrane wing, there is less variation of L/D ratio versus AoA, meaning that a flexible wing offer more stable flight behavior. Fourth, increased camber allows for increased lift. However, there can be some disadvantages. Depending on the degree of membrane pre-tension, the drag can be large for the flapping flight. Membrane wings can reduce effective AoA that would decrease lift.

Studies were performed on wings with different degrees of flexibility: chordwise, spanwise, and combined. Shyy *et al.* [88] gives a great review of recent work in aeroelasticity presented conveniently in the table format. Those tables provide the type of the wings used in the study, its kinematics, *Re* and *St* numbers, and structural parameters. Similarly, Table 2-6 gives an overview of various aeroelastic research studies on flexible wings with corresponding numerical methods that are used to solve fluid-structure problems. Items in Table 2-6 are sorted in accordance with increasing *Re* number.

Table 2-6. Aeroelastic approaches on studying flexible wing flight.

Author(s)	**Wing Type and Shape**	**Fluid Solver**	**Structural Solver**	***Re* number**	***St* number or reduced freq., *k***	**Wing Kinematics**
Luo *et al.* [57]	Dragonfly wings	sharp-interface immersed-boundary method (IBM)	Nonlinear finite element (FE) solver: plate elements	5×10^1	0.94	

Tang *et al.* (2007) [99]	2-D teardrop plate	Pressure -based algorithm	linear beam solver	1×10^2 and 9×10^3		Pure plunging
Ishihara *et al*. [38]	dipteran wing as thin rigid elastic plate	2-D nonlinear FE used for the analysis of both the fluid and the structure		2×10^2	0.054	Pitch and plunge
Shao *et al.* [85]	3-D NACA0012 airfoil	(IBM)	Physical Virtual Model (PVM)	2×10^2	0.35 and 0.6	Plunge and pitch
Pederzani and Haj-Hariri [76]	Membrane airfoil	A mixed Eulerian–Lagrangian approach		5×10^2	5.5	Plunge
Aono *et al.* [7]	Flexible membrane wings: Zimmerman	Pressure -based algorithm	Nonlinear FE using triangular shell elements.	6.2 $\times 10^2$ and 2.6 $\times 10^3$	0.56 and 2.35	Pure plunge
Smith [90]	moth wings	unsteady panel method	Finite element: linear elastic beam and membrane elements	1×10^3	$k \geq 0.2$	flapping
Singh [89]	Insect-like wings	unsteady aerodynamic analysis based on indicial functions	FE	10^3 *to* 10		Pitch and plunge

Toomey and Eldredge [104]	Elliptical shape	Viscous vortex particle method (VVPM) with coupled fluid-body dynamics.		1.2×10^3 to 6.1×10^3		Pitch and plunge
Gordnier [26]	2-D flexible membrane airfoil	Finite-difference solver	Nonlinear finite-difference based membrane solver	2.5×10^3		stationary
Smith and Shyy [92]	2-D flexible sail-shaped membrane airfoil	Pressure-based method	Nonlinear finite-difference based membrane solver	4×10^3		stationary
Young *et al.* [118]	Locust wings	3-D CFD simulation based on detailed wing kinematics.		4×10^3		Real flight
Agrawal and Agrawal [1]	Hawkmoth-like membrane wing	Reversed design from kinematics	FE Abacus: linear shell elements	7×10^3	0.2	Real flight
Chandar and Damodaran [11]	Teardrop plate	incompressible flow solver based on overlapping grids using an implicit partitioned algorithm.		9×10^3	0.5	Plunge
Gopalakri-shnan [25]	Rectangular membrane	Arbitrary Lagrangian Eulerian (ALE) method		1×10^4	1.7	Pitch and plunge
Zhu [119]	3-D rectangular foil	3-D boundary integral method	nonlinear thin-plate model	2.025×10^4	0.2	Pitch and plunge

Tang *et al.* [100]	NACA0012	Finite-volume	3-D FE beam solver	3×10^4		Pure plunging
Aono *et al.* [6]	flexible rectangular wing	pressure-based finite-volume fluid flow solver	a quasi-3D FE solver based on a geometrically nonlinear beam and linear plate elements	3×10^4	1.82	Pure plunge
Chimakurthi *et al.* [12]	NACA0012, airfoil: flexible and rigid	pressure-based algorithm implemented in STREAM	In-house developed UM/NLABS method or Nonlinear FE solver MSC.Marc	3×10^4	0.4 to 1.82	plunging
Stanford and Ifju [98]	Membrane wing	finite volume formulation	Linear FE analysis: triangular plate elements	4×10^4 and 7×10^4		stationary
Guvernyuk and Dynnikova [31]	NACA0012	Lagrangian vortex method		4.4×10^4		Pitching
Kim *et al.* [43, 44]	Rectangular wing	Numerical model based on modified strip theory	FE method based on Flexible Multi-body Dynamics	8.25×10^4		Flapping

Lian *et al.* [51]	membrane wing	pressure-based approach	3-D FE method with triangular element			stationary
Hamamoto *et al.* [32]	deformable dragonfly wing	FE analysis based on the arbitrary Lagrangian–Eulerian method: common mesh system can be used for the analysis of both the fluid and the structure				hovering
Bergou *et al.* [8]	2-D rigid plate	Immersed-Interface Method	Blade-element theory			pitching
Liani *et al.* [52]		unsteady panel method	Lagrange's equations of motion for a 2-D spring-mass wing system			Pitch and plunge
Willis *et al.* [115]		A multiple method approach: HallOpt, ASWING, FastAero, 3DG. All these methods are used in complex.				

2.5.1 Overview of Structural Models to Analyze Flapping Flight

As can be noted from Table 2-6, for structural part, finite element approach is prevailing over the variety of other approaches. Nonlinear analysis is preferred since the flapping flight of natural fliers is a highly nonlinear phenomenon.

2.5.2 Overview of Aerodynamic Models to Analyze Flapping Flight

For the fluid part that computes aerodynamic forces and moments acting on a wing, there are several approaches that may be utilized. They all can be divided into quasi-steady methods and methods that are capable of solving for unsteady flow. All methods have their limitations. However, depending on the application, they can offer some advantages.

The well-known quasi-steady methods are momentum (or momentum-jet) method, blade-element method, and hybrid momentum (or vortex method) [91]. Quasi-steady methods are used by biologists to predict energy consumption as a function of forward speed, which allows the prediction of animal size. All of them hold the assumption that instantaneous aerodynamic forces developed by flapping motion are similar to the forces developed during steady motion at the same instantaneous velocity. Quasi-steady methods do not account for the unsteady flow, such as development of free vortices, which are actually produced by birds‟ wings.

Methods for analyzing unsteady flow include the lifting-line method, lifting-surface or vortex lattice method, unsteady panel method or boundary element method, modified strip method, pressure-based methods, Cartesian grid methods, immersed boundary method, immersed interface method, and some others, as shown in Table 2-6.

The unsteady lifting-line method has several modifications. The recent one is the low-frequency unsteady lifting-line method for harmonically oscillating wing of large aspect ratios. This approach is based on Prandtl‟s classical lifting-line theory, which is a 2-D theory. This method gives reasonable preliminary results for high-angle-of-attack post-stall region. There are a few major limitations of this method. First, it only applies for

small amplitude motions with high aspect ratio wings. Second, it serves as 3-D adaptation of the 2-D theory. At high AoA, which pertains to bird‟s flight, the flow is highly 3-D, and the use of 2-D lift coefficient data becomes unreasonable. Third, although this method gives reasonable preliminary results on wake and force resolutions, it does not offer the detailed geometric and kinematic effects of the wing.

In comparison to the lifting-line method, the lifting-surface or advanced vortex lattice method offers the detailed view of geometry and kinematics of the wing during flight by representing the wake and the wing by a lattice of vortex filaments. There are some limitations. This method is restricted to the small-amplitude harmonic motion. Also, the method relies on experimental results and uses derived „shape factors‟ to account for dynamic effects. And, finally, the lifting-surface method cannot offer detailed free-wake analysis.

The unsteady aerodynamic panel method is also called the classical boundary element method and is based on the potential flow theory [91], which assumes inviscid conditions. It is valid for $R_e \geq 10^4$, which is valid only for birds‟ flight, not including hummingbirds. There are three major advantages of this method. First, it accommodates the details of the trailing wake. Second, it offers distributed aerodynamic effects for rigid flapping wings. Third, it provides flexibility and interference effects.

The modified strip method is a 2-D method that uses the thin airfoil theory to analyze harmonically oscillating wings. The strip theory was initially used to analyze helicopter blades. The method employs the 3-D modified Theodorsen function, $C(k)$, to account for

wings of finite aspect ratio and such aerodynamic effects as partial leading-edge suction force, post-stall phenomena, friction drag, and vortex wake [14]. The modified strip theory is convenient to implement; however, it was successfully proven only for small-amplitude oscillations, such as in analysis of the stability of helicopter rotors, where the deflections of the rotors are of a small magnitude [91]. On the other hand, recent improvements in this theory allow consideration of dynamic stall at high relative angle of attack [44], and, as research showed, the improvements allowed for more accurate prediction of unsteady aerodynamics of the flapping flight.

Pressure-based methods develop an artificially derived pressure or correction equation by manipulating the mass continuity and momentum equations [51]. Most popular pressure-based methods are SIMPLE and PISO that are used to solve 3-D Navier–Stokes equations for incompressible flows in curvilinear coordinates.

Cartesian grid methods [50], such as the immersed boundary method and the immersed interface method, are used to solve incompressible Navier-Stokes equations in complicated geometries with moving elastic boundaries.

CHAPTER 3

Theoretical Aeroelasticity for Fluid-Structure Interaction Problems

This chapter presents the theoretical framework used in this research for nonlinear aeroelastic analysis of bird flight. In particular, we present an aerodynamic model based on an enhanced modified strip theory and a fully nonlinear finite element model of wing structures based on geometrically exact total-Lagrangian beam and membrane elements.

3.1 Aerodynamic Model: Enhanced Modified Strip Theory

This research adopts an improved modified strip theory to analyze flapping flight since it is appropriate for calculation of unsteady aerodynamics and is convenient to implement. This model was validated by comparing it with experimental results for an oscillating flat plate wing. This section reviews this improved modified strip theory in details.

Model Assumptions:

DeLaurier [14] developed this theory with the assumptions that (1) the span is not variable; (2) wing's aspect ratio is so large that the flow is considered chordwise, in the free stream direction; (3) each chordwise strip on the wing is assumed to act as if it is part of the elliptical planform wing, of the same aspect ratio, performing simple harmonic whole wing motions identical to that of the strip's; (4) flapping is a continuous sinusoidal motion with equal times between the upstroke and downstroke; (5) the relative angle of attack between the free stream velocity U and the resultant flow relative velocity V_{rel} at

the ¼-chord location is small; and (6) the flapping motion is perpendicular to the flapping axis, but local deformation is allowed.

Model Free Body Diagrams in 2-D and 3-D Views:

A wing section with aerodynamic forces and motion variables is shown in Fig. 3-1 [14, 67].

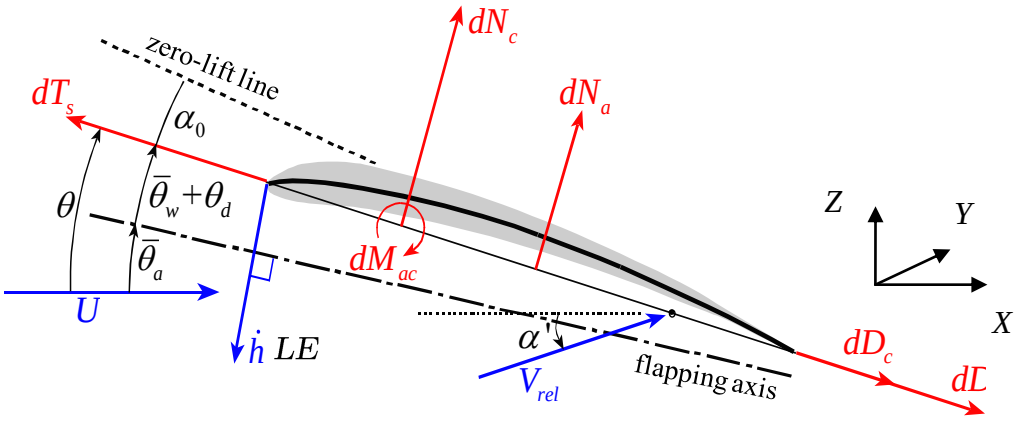

Fig. 3-1. A wing section with aerodynamic forces and motion variables.

Leading edge (LE) is the reference point. Each section is able to move up and down with a plunge velocity $\dot{h}$, and rotate about the global *Y-axis* at point LE with a pitch angle θ. The plunge velocity $\dot{h}$ for any section is *not* necessarily perpendicular to the free stream velocity U. If the wing is root-flapping, as shown in Fig. 3-2 [43, 67], then $\dot{h}$ would be perpendicular to the flapping axis.

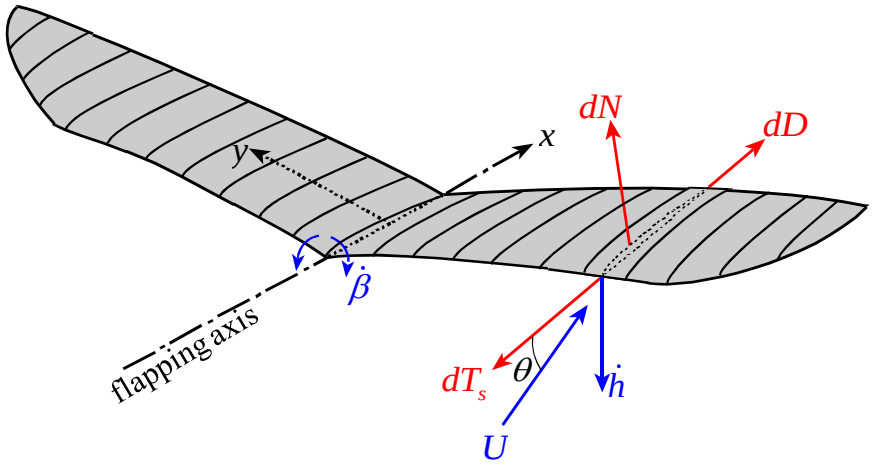

Fig. 3-2. Root flapping wing geometry and aerodynamic forces.

Model Derivation:

As was mentioned in Sec. 2.4.2, this method is based on a modified Theodorsen function for wings of a finite aspect ratio, which is given in Eq. (3.1).

$$C(k)_{Jones} = \frac{C'(k)\,AR}{(2+AR)} \tag{3.1}$$

Here, AR is the aspect ratio that is given by Eq. (3.2); k is the reduced frequency that is given by Eq. (3.3); and $C'(k)$ is given by Eq. (3.4).

$$AR = \frac{b}{c_{mean}} \tag{3.2}$$

$$k = \frac{c\omega}{2U} \tag{3.3}$$

$$C'(k) = F'(k) + iG'(k) \tag{3.4}$$

In Eq. (3.2), b is the wing span and c_{mean} is the mean chord length. In Eq. (3.3), ω is the flapping or plunging frequency given in radians per second. And, for Eq. (3.4), the terms are given as follows:

$$F'(k) = 1 - \frac{C_1 k^2}{(k^2 + C_2^2)} \tag{3.5}$$

$$G'(k) = -\frac{C_1 C_2 k}{(k^2 + C_2^2)} \tag{3.6}$$

In Eqs. (3.5) and (3.6), C_1 and C_2 are constants given by Eqs. (3.7) and (3.8).

$$C_1 = \frac{0.5\ AR}{(2.32 + AR)} \tag{3.7}$$

$$C_2 = 0.181 + \frac{0.772}{AR} \tag{3.8}$$

The modified Theodorsen function is used to compute unsteady normal-force coefficient, δC_n, which is given by Eq. (3.9) and derived for the elliptical planform wing mentioned in assumption (3).

$$\delta C_n = 2\pi\ C(k)_{Jones}\ \alpha_{@3/4} \tag{3.9}$$

Here, $\alpha_{@3/4}$ is the relative angle of attack at $^3/_4$-chord length due to the wing's motion; and it is given by Eq. (3.10). This angle accounts for the wing's finite-span unsteady vortex wake by means of a strip theory.

$$\alpha_{@3/4} = \frac{\dot{h}\cos(\theta - \bar{\theta}_a) + \frac{3}{4}c\dot{\theta} + U\,sin(\theta - \bar{\theta})}{U}$$

$$\approx \frac{\dot{h}\cos(\theta - \bar{\theta}_a) + \frac{3}{4}c\dot{\theta} + U\,(\theta - \bar{\theta})}{U}$$

$$= \frac{\dot{h}\cos(\theta_d + \bar{\theta}_w) + \frac{3}{4}c\dot{\theta} + U(\theta_d)}{U} \tag{3.10}$$

Here, θ is the pitch angle of chord with respect to U; $\bar{\theta}$ is the section's mean pitch angle; $\bar{\theta}_a$ is the angle of the flapping axis with respect to U; $\bar{\theta}_w$ is the mean pre-twisted angle of chord with respect to the flapping axis; and θ_d is the dynamically-varying pitch angle. The relation between these angles is given by Eq. (3.11).

$$\theta = \bar{\theta} + \theta_d = (\bar{\theta}_a + \bar{\theta}_w) + \theta_d \tag{3.11}$$

Next we derive aerodynamic forces acting on a wing. Instantaneous lift and thrust forces for each segment are given by Eq. (3.12) and Eq. (3.13) as

$$dL = dN\cos(\theta) + dF_x\sin(\theta) \tag{3.12}$$

$$dT = -dN\sin(\theta) + dF_x\cos(\theta) \tag{3.13}$$

Here, dN is the section's instantaneous normal force that is given by Eq. (3.14); and dF_x is the section's instantaneous total chordwise (*x-direction*) force that is given by Eq. (3.15).

$$dN = dN_c + dN_a \tag{3.14}$$

$$dF_x = dT_s - dD_c - dD_f \tag{3.15}$$

In Eq. (3.14), dN_c is the section's normal circulatory force and dN_a is the section's normal force due to apparent mass effect, which acts at midchord. In Eq. (3.15), dT_s is the thrust force due to leading edge suction; dD_c is the chordwise pressure drag due to camber shape; and dD_f is the chordwise friction drag due to viscous effects.

The analysis will be different depending on whether the flow is attached or separated. The condition for attached flow is given by Eq. (3.16). If the range for the attached flow is exceeded, flow becomes separated.

$$(\alpha_{stall})_{min} \leq \left[\alpha' + \bar{\theta} - \frac{3}{4}\left(\frac{c\,\dot{\theta}}{U}\right) \right] \leq (\alpha_{stall})_{max} \tag{3.16}$$

This criterion allows for the approximation of the localized post stall behavior, and, in this case, it is applied at the leading edge.

In Eq. (3.16), α_{stall} is the *dynamic* stall angle; α' is the flow's relative angle of attack at $^3/_4$-chord length; $\bar{\theta}$ is the section's mean pitch angle; c is the chord length; $\dot{\theta}$ is the pitch velocity; and U is the free stream or flight velocity.

For a totally *attached* flow, section's reaction forces are calculated differently. Normal circulatory force is given by Eq. (3.17).

$$dN_c = C_n(y)\left(\frac{1}{2}\,\rho U V_{rel@1/4}\right)\, c\, dy \tag{3.17}$$

Here, ρ is the fluid density; U is the flight velocity; c is the chord length; $V_{rel@1/4}$ is the flow's relative velocity at the $^1/_4$-chord length that is given by Eq. (3.18); and $C_n(y)$ is the normal force coefficient that is calculated using Eq. (3.19).

$$V_{rel@1/4} = \sqrt{[Ucos\,\theta - \dot{h}\,\sin(\theta - \bar{\theta}_a)]^2 + [U(\alpha' + \bar{\theta}) - \frac{1}{2}c\dot{\theta}]^2} \quad (3.18)$$

$$C_n(y) = 2\pi(\alpha' + \alpha_0 + \bar{\theta}) \quad (3.19)$$

Here, α_0 is the angle of the zero lift line, as shown in Fig. 3-1.

Equations (3.16), (3.18), and (3.19) all contain the flow's relative angle of attack at $^3/_4$-chord length, α'. To find it, equate unsteady normal-force coefficient, δC_n, in Eq. (3.9) with the normal force coefficient, $C_n(y)$.

$$\begin{aligned} C_n(y) &= \delta C_n \\ 2\pi(\alpha' + \alpha_0 + \bar{\theta}) &= 2\pi\, C(k)_{Jones}\, \alpha_{@3/4} \\ (\alpha' + \alpha_0 + \bar{\theta}) &= C(k)_{Jones}\, \alpha_{@3/4} \\ \alpha' &= C(k)_{Jones}\, \alpha_{@3/4} - (\alpha_0 + \bar{\theta}) \end{aligned} \quad (3.20)$$

After substitution of Eq. (3.1) and rearranging the terms, α' is given by Eq. (3.21).

$$\alpha' = \frac{C'(k)\,AR}{(2+AR)}\ \alpha_{@3/4} - \frac{w_{0@3/4}}{U} \quad (3.21)$$

Here, $w_{0\,@3/4}$ is the downwash velocity at $^3/_4$-chord length; and $\frac{w_0}{U}$ is the downwash term due to mean lift produced by α_0 and $\bar{\theta}$. This downwash term can be calculated in

different ways; and, in accordance with the strip theory, the downwash term is approximated as the downwash for an *untwisted* elliptical planform wing given in Eq. (3.22).

$$\frac{w_0}{U} = \frac{2(\alpha_0+\bar{\theta})}{(2+AR)} \tag{3.22}$$

However, if the wing has significant spanwise variation of $\alpha_0 + \bar{\theta}$, then the other way to calculate downwash should be considered, such as the extended lifting-line theory for *twisted* wings [45].

Equation (3.21) can be rewritten when considering the assumed harmonic motion of the wing. If $\alpha_{@3/4}$ is approximated by Euler's formula as

$$\alpha_{@3/4} = Ae^{i\omega t} \tag{3.23}$$

where A is the constant, then α' can be written as Eq. (3.24).

$$\alpha' = \frac{AR}{(2+AR)}\left[F'(k)\,\alpha_{@3/4} + \frac{c}{2U}\frac{G'(k)}{k}\dot{\alpha}_{@3/4}\right] - \frac{w_{0@3/4}}{U} \tag{3.24}$$

Another component of the normal force is due to the apparent mass effect that acts at midchord and is given by Eq. (3.25).

$$dN_a = \frac{\rho\pi c^2}{4}\dot{v}_2\,dy \tag{3.25}$$

Here, $\dot{v}_2$ is the midchord normal acceleration that is given by Eq. (3.26). $\dot{v}_2$ is the linearized time derivative of the midchord normal velocity, V_n, given by Eq. (3.27).

$$\dot{v}_2 = U\dot{\alpha}_{@3/4} - \frac{1}{4}c\ddot{\theta} \approx \dot{V}_n \tag{3.26}$$

$$V_n = \dot{h}\cos(\theta - \bar{\theta}_a) + \frac{1}{2}c\dot{\theta} + U\,sin(\theta) \tag{3.27}$$

Thus, adding Eqs. (3.17) and (3.25) gives the normal force for the attached flow.

Next, components for Eq. (3.15) for the *attached* flow are computed. The thrust force due to leading edge suction, dT_s, is given by Eq. (3.28).

$$dT_s = \eta_s 2\pi \left(\alpha' + \bar{\theta} - \frac{1}{4}\frac{c\,\dot{\theta}}{U}\right)^2 \frac{\rho\, U\, V_{rel@1/4}}{2} c\, dy \tag{3.28}$$

Here, η_s is the leading edge suction efficiency that accounts for the fact that, due to viscosity in the real conditions, the leading-edge suction is less than 100 percent. The 100 percent suction is predicted by potential flow theory.

The chordwise pressure drag due to the camber shape, dD_c, is given by Eq. (3.29).

$$dD_c = -2\pi\alpha_0(\alpha' + \bar{\theta}) \frac{\rho\, U\, V_{rel@1/4}}{2} c\, dy \tag{3.29}$$

Finally, the chordwise friction drag due to viscous effects, dD_f, is given by Eq. (3.30).

$$dD_f = (C_d)_f \frac{\rho\, {V_x}^2}{2} c\, dy \tag{3.30}$$

Here, $(C_d)_f$ is the skin friction drag coefficient [37]; and V_x is the tangential velocity to the section and is given by Eq. (3.31).

$$V_x = U\cos(\theta) - \dot{h}\,sin(\theta - \bar{\theta}_a) \tag{3.31}$$

Thus, substituting Eqs. (3.28), (3.29) and (3.30) into Eq. (3.15) gives the total chordwise force for the attached flow.

For a *separated* flow, section's reaction forces are calculated next. By analogy, the normal circulatory force for separated flow is given by Eq. (3.32).

$$(dN_c)_{sep} = (C_d)_{cf}\left(\frac{1}{2}\,\rho\tilde{V}V_n\right)\,c\,dy \tag{3.32}$$

Here, $(C_d)_{cf}$ is the drag coefficient due to cross-flow; and $\tilde{V}$ is given by Eq. (3.33).

$$\tilde{V} = \sqrt{{V_x}^2 + {V_n}^2} \tag{3.33}$$

Another component of the normal force that is due to the apparent mass effect that acts at midchord and is approximated by Eq. (3.34).

$$(dN_a)_{sep} = \frac{1}{2}dN_a \tag{3.34}$$

Thus, adding Eqs. (3.32) and (3.34) gives the normal force for a separated flow.

For a separated flow, all chordwise force components are considered negligible. Thus,

$$(F_x)_{sep} = 0 \tag{3.35}$$

Now, integrating segment's instantaneous lift and thrust from Eqs. (3.12) and (3.13) along the wing span gives instantaneous lift and thrust for the entire wing.

$$L(t) = 2\int_0^{b/2}\cos(\beta)\,dL \tag{3.36}$$

$$T(t) = 2\int_0^{b/2} dT \tag{3.37}$$

Here, b is the wing span; and $\beta(t)$ is the section's instantaneous dihedral angle.

Next, integrating instantaneous lift and thrust over the cycle gives average lift and thrust for the wing.

$$\bar{L} = \frac{1}{2\pi}\int_0^{2\pi} L(\varphi)d\varphi \tag{3.38}$$

$$\bar{T} = \frac{1}{2\pi}\int_0^{2\pi} T(\varphi)d\varphi \tag{3.39}$$

Here, φ is the cycle angle that is given by Eq. (3.40).

$$\varphi = \omega t \tag{3.40}$$

In addition to lift and thrust, instantaneous input power required to move the section though the air is given by Eq. (3.41) for an attached flow and by Eq. (3.42) for a separated flow.

$$dP_{in} = dF_x\dot{h}\sin(\theta - \bar{\theta}_a) + dN\left(\dot{h}\,cos(\theta - \bar{\theta}_a) + \frac{1}{4}c\dot{\theta}\right) + dN_a\left(\frac{1}{4}c\dot{\theta}\right) - dM_{ac}\dot{\theta} - dM_a\dot{\theta} \tag{3.41}$$

$$(dP_{in})_{sep} = (dN_{total})_{sep}\left(\dot{h}\,cos(\theta - \bar{\theta}_a) + \tfrac{1}{2}c\dot{\theta}\right) \tag{3.42}$$

For the attached flow shown in Eq. (3.41), dM_{ac} is the section's pitching moment about its aerodynamic center and is given by Eq. (3.43); and dM_a is the sum of apparent camber and apparent inertia moments and is given by Eq. (3.44).

$$dM_{ac} = C_{mac}\frac{\rho U V_{rel@1/4}}{2}\,c^2\,dy \tag{3.43}$$

$$dM_a = -\left(\frac{1}{16}\rho\pi c^3\dot{\theta}U + \frac{1}{128}\rho\pi c^4\ddot{\theta}\right)dy \tag{3.44}$$

In Eq. (3.43), C_{mac} is the moment coefficient. For a separated flow, $dM_{ac} = dM_a = 0$.

Thus, for the entire wing, the total required instantaneous power, $P_{in}(t)$, the average input power through the cycle, $\bar{P}_{in}$, the average output power through the cycle, $\bar{P}_{out}$, and the average propulsive efficiency, $\bar{\eta}$, are given by Eqs. (3.45), (3.46), (3.47), and (3.48) as

$$P_{in}(t) = 2\int_0^{b/2} dP_{in} \tag{3.45}$$

$$\bar{P}_{in} = \frac{1}{2\pi}\int_0^{2\pi} P_{in}(\varphi)d\varphi \tag{3.46}$$

$$\bar{P}_{out} = \bar{T}U \tag{3.47}$$

$$\bar{\eta} = \frac{\bar{P}_{out}}{\bar{P}_{in}} \tag{3.48}$$

Improvements of the Modified Strip Theory:

As not accounted for by DeLaurier, aerodynamic forces at high angles of attack, that happen either at high plunging velocity or at low free stream velocity in comparison to the plunge velocity, are studied by Kim *et al.* [44]. The relative angle of attack, γ, is shown in Fig. 3-3 [44] and is given by Eq. (3.49). It is calculated by using the normal component of velocity at $^1/_4$-chord length and the tangential component of the velocity.

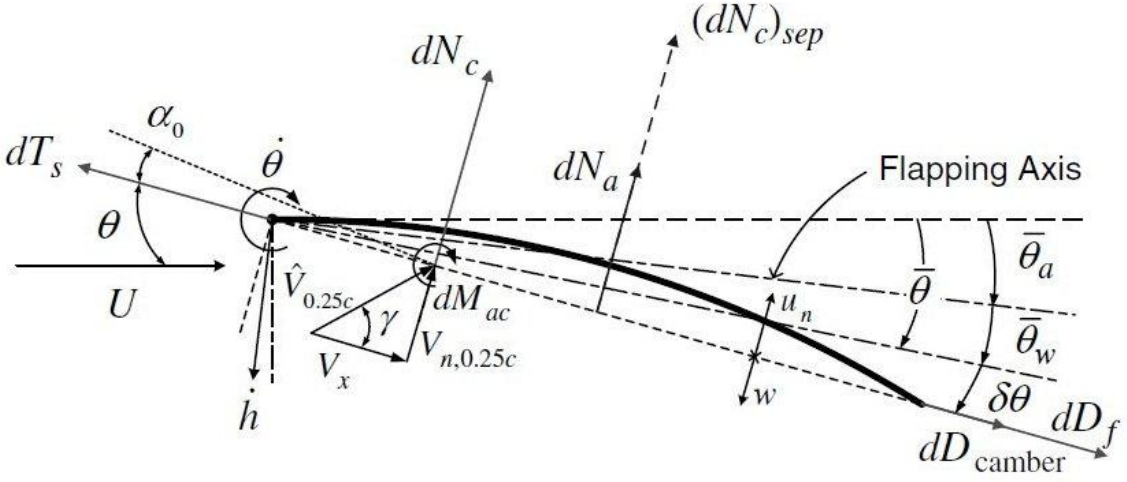

Fig. 3-3. Wing section aerodynamic forces and motion variables: accounting for high angle of attack.

$$\gamma = tan^{-1}\left(\frac{V_{n,0.25c}}{V_x}\right)$$

$$= tan^{-1}\left(\frac{\dot{h}\cos(\theta-\bar{\theta}_a)+\frac{1}{4}c\dot{\theta}+U\,sin(\theta)-w}{U\,cos(\theta)-\dot{h}\sin(\theta-\bar{\theta}_a)}\right) \tag{3.49}$$

Here, w is the downwash velocity at the $^1/_4$-chord length. In Eq. (3.49), sin (θ) can be expressed by using trigonometric series as given in Eq. (3.50).

$$\sin(\theta) = \delta\theta + \bar{\theta} + \mathcal{O}(\theta^3) \tag{3.50}$$

Here, $\delta\theta$ is the section's zero-mean dynamic pitch angle; $\bar{\theta}$ is the section's mean pitch angle as shown in Fig. 3-3; and the term $\mathcal{O}(\theta^3)$ represents the sum of higher-order terms.

Using Eq. (3.24) for flow's relative angle of attack at $^3/_4$-chord length, α', and Eq. (3.50), the normal component of velocity at $^1/_4$-chord length is given in Eq. (3.51).

$$V_{n,0.25c} = U\left(\frac{\dot{h}\cos(\theta-\bar{\theta}_a)+\frac{3}{4}c\dot{\theta}+U(\delta\theta)-w}{U}\right)+U[\,\bar{\theta}+\mathcal{O}(\theta^3)]-\frac{1}{2}c\dot{\theta}$$

$$= U[\alpha'+\,\bar{\theta}+\mathcal{O}(\theta^3)]-\frac{1}{2}c\dot{\theta} \tag{3.51}$$

Then, γ can be expressed as follows:

$$\gamma = tan^{-1}\left(\frac{U[\alpha'+\bar{\theta}+\mathcal{O}(\theta^3)]-\frac{1}{2}c\dot{\theta}}{U\,cos(\theta)-\dot{h}\sin(\theta-\bar{\theta}_a)}\right) \tag{3.52}$$

Accounting for the relative angle of attack, some aerodynamic forces for attached flow given by Eqs. (3.17), (3.28), and (3.29) are rewritten as follows:

$$dN_c = C_n(y)\cos(\gamma)\left(\frac{1}{2}\,\rho\,U\,\hat{V}_{rel@1/4}\right)\,c\,dy \tag{3.53}$$

$$dT_s = \eta_s 2\pi\left(\alpha'+\bar{\theta}-\frac{1}{4}\,\frac{c\,\dot{\theta}}{U}\right)^2\sin(\gamma)\left(\frac{1}{2}\rho\,U\,\hat{V}_{rel@1/4}\right)c\,dy \tag{3.54}$$

$$dD_c = -2\pi\alpha_0(\alpha'+\bar{\theta})\cos(\gamma)\left(\frac{1}{2}\rho\,U\,\hat{V}_{rel@1/4}\right)c\,dy \tag{3.55}$$

Here, $\hat{V}_{rel@1/4}$ is given by Eq. (3.56).

$$\hat{V}_{rel@1/4} = \sqrt{V_x{}^2+V_{n,0.25c}{}^2} \tag{3.56}$$

The other forces, dN_a and dD_f, given by Eqs. (3.25) and (3.30) respectively, do not change.

The condition, given by Eq. (3.16) that defines whether the flow is attached or separated, allows for the approximation of the localized post stall behavior. In the attempt to improve DeLaurier model, instead of just one criterion, Kim *et al.* [44] propose three criteria for analyzing dynamic stall and post stall behavior of the wing. These criteria are given by Eqs. (3.57.a), (3.57.b), and (3.57.c).

$$\text{Attached flow:} \quad (\alpha_{stall})_{min} \leq \left[\gamma - \frac{1}{4}\left(\frac{c\,\dot{\theta}}{U}\right)\right] \leq (\alpha_{stall})_{max} \qquad \text{(a)}$$

$$\text{Dynamic stall:} \quad (\alpha_{dynamic})_{min} \leq \left[\gamma - \frac{1}{4}\left(\frac{c\,\dot{\theta}}{U}\right)\right] \leq (\alpha_{dynamic})_{max} \qquad \text{(b)} \qquad (3.57)$$

$$\text{Post stall:} \quad defined\ beyond\ the\ dynamic\ stall\ range \qquad \text{(c)}$$

In Eq. (3.57a), $(\alpha_{stall})_{min}$ and $(\alpha_{stall})_{max}$ are the minimum and maximum *static* stall angles obtained from the steady aerodynamic data. In Eq. (3.57b), $(\alpha_{dynamic})_{min}$ and $(\alpha_{dynamic})_{max}$ are the minimum and maximum *dynamic* stall angles that are valid only for the attached flow condition and are given by Eqs. (3.58a) and (3.58b).

$$(\alpha_{dynamic})_{min} = \xi_{min}(\alpha_{stall})_{min} \qquad \text{(a)}$$

$$(\alpha_{dynamic})_{max} = \xi_{max}(\alpha_{stall})_{max} \qquad \text{(b)} \qquad (3.58)$$

In Eqs. (3.58a) and (3.58b), ξ_{min} and ξ_{max} are defined by Eqs. (3.59) and (3.60) respectively.

$$\xi_{min} = \begin{cases} 1 + \left|\dfrac{tan^{-1}\left(\frac{\dot{h}\cos(\theta-\bar{\theta}_a)}{V_x}\right)}{(\alpha_{stall})_{\min}}\right| + \dfrac{0.51\frac{\theta}{\theta_{mag}}\sqrt{\frac{c\dot{\theta}_{mag}}{2U}}}{(\alpha_{stall})_{\min}} & for\ (\alpha_{dynamic})_{min} \geq 2(\alpha_{stall})_{min} \\ 2 & for\ (\alpha_{dynamic})_{min} < 2(\alpha_{stall})_{min} \end{cases} \qquad (3.59)$$

$$\xi_{max} = \begin{cases} 1 + \left| \frac{tan^{-1}\left(\frac{\dot{h}\cos(\theta - \bar{\theta}_a)}{V_x}\right)}{(\alpha_{stall})_{\min}} \right| + \frac{0.51\frac{\theta}{\dot{\theta}_{mag}}\sqrt{\frac{c\dot{\theta}_{mag}}{2U}}}{(\alpha_{stall})_{\min}} & for\ (\alpha_{dynamic})_{max} \leq 2(\alpha_{stall})_{max} \\ 2 & for\ (\alpha_{dynamic})_{max} > 2(\alpha_{stall})_{max} \end{cases}$$

(3.60)

Depending on the condition given in Eq. (3.57), the aerodynamic forces applied differently on the section of the wing. Figures 3-4(a), 3-4(b), and 3-4(c) represent these forces for different conditions [44]

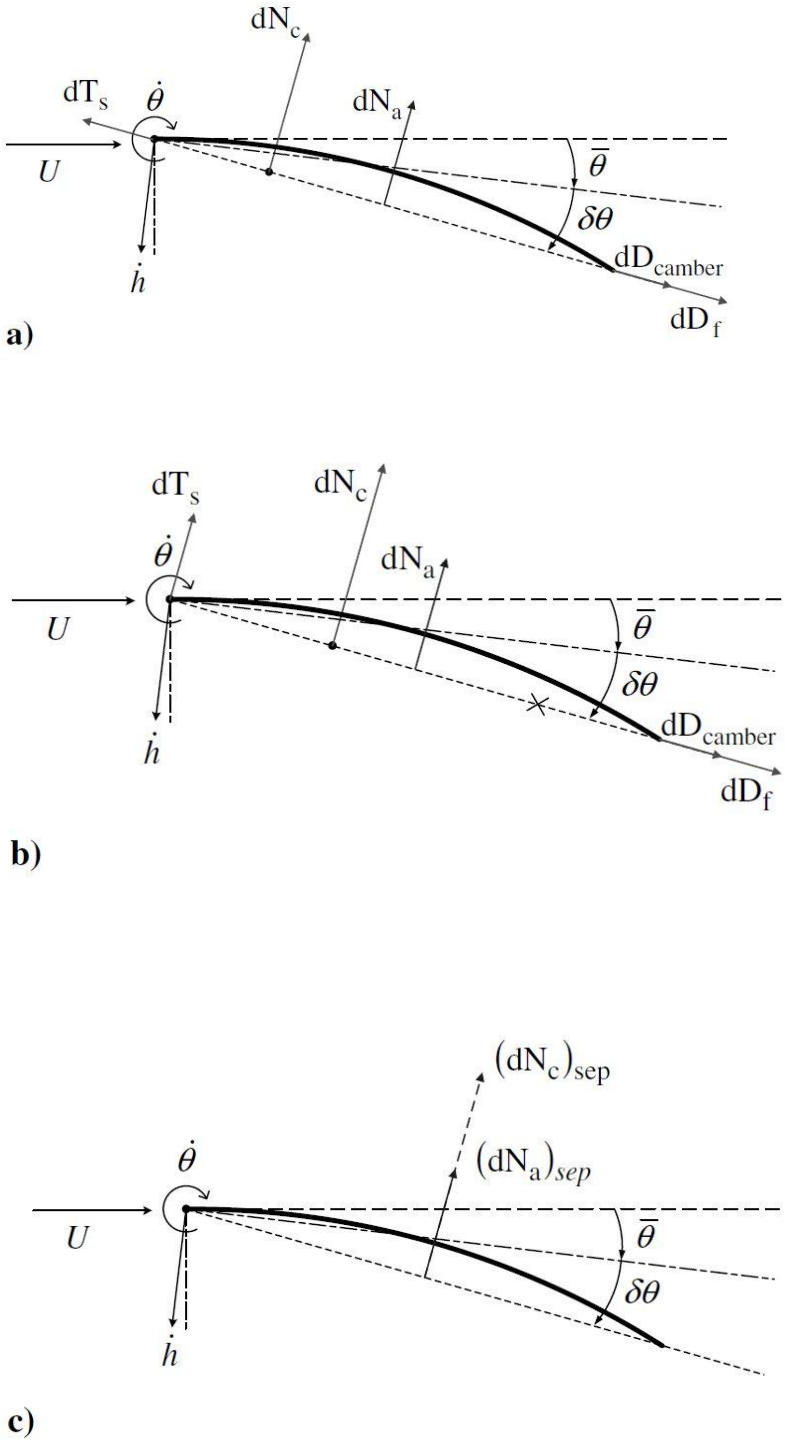

Fig. 3-4. Wing section aerodynamic forces according to the stall condition: (a) attached flow range; (b) dynamic stall range; (c) post stall range.

As can be seen from the figures above, normal circulatory force, dN_c, is applied at $^1/_4$-chord length in Fig. 3-4 (a); at $^1/_3$-chord length in Fig. 3-4 (b); and at $^1/_2$-chord length in Fig. 3-4 (c). Also, in Fig. 3-4 (b), to account for the leading-edge vortex, the direction of the thrust force due to the leading-edge suction, dT_s, is assumed as perpendicular to the chord.

In the attached flow range, the section's instantaneous total normal force is calculated using Eqs. (3.53) and (3.25); and the section's instantaneous total chordwise force is calculated using Eqs. (3.54), (3.55), and (3.30). In the post stall range, or, in other words, when the flow becomes separated, the section's instantaneous aerodynamic forces stay the same as defined by Eqs. (3.32), (3.34) and (3.35).

3.2 Structural Model for Current Research: Fully Nonlinear Finite Element Analysis

Theoretical Basis:

The structural module that is used for current research is the Geometrically Exact Structural Analysis (GESA). GESA is based on a total-Lagrangian displacement-based finite element method, is written in Matlab, and is capable of solving for nonlinear large static and dynamic deformations of flexible structures [66].

For geometrically nonlinear structures, the total-Lagrangian formulation is commonly used because there is a natural undeformed state to which the structure would return when it is unloaded. GESA uses the total-Lagrangian (TL) approach since it is more

appropriate for nonlinear analysis because (1) the accuracy of the current iteration solution does not depend on the accuracy of the previous converged solution; (2) stresses and strains equations do not need any coordinate transformation before next iteration. However, researchers often use Green-Lagrange strains and Piola-Kirchhoff stresses with a total-Lagrangian formulation. Unfortunately, Green-Lagrange strains are energy strains instead of geometric strains, and they cannot fully account for geometric nonlinearities. On the other hand, Pai [66] showed that Jaumann strains and stresses with the use of a total-Lagrangian formulation can fully account for any order of geometric nonlinearities. Eq. (3.61) shows the strain-displacement relation of Jaumann strains.

$$B_{mn} = \frac{1}{2}\left(\frac{d\boldsymbol{u}}{dx_m} \circ \boldsymbol{i}_n + \frac{d\boldsymbol{u}}{dx_n} \circ \boldsymbol{i}_m\right) \tag{3.61}$$

Here, $\boldsymbol{u}$ is the local displacement vector of an arbitrary point with respect to its deformed location; dx_j are unstrained lengths; and $\boldsymbol{i}_j$ are unit vectors along the convected coordinate axes if shear strains are zero. If shear strains are nonzero, a co-rotated point reference frame is proposed to be used applying the symmetry of Jaumann strains.

In particular, GESA applies the *extended Hamilton principle* given by Eq. (3.62) derived from the *Newton's second law* by means of *D'Alembert's principle* and *the principle of virtual work*.

$$\int_{t_1}^{t_2}[\delta \mathrm{T} - \delta\Pi + \delta W_{nc}]dt = 0 \tag{3.62}$$

Here, the term δ means variation; δT is the variation of kinetic energy; $\delta\Pi$ is the variation of potential (or elastic) energy; and δW_{nc} is non-conservative virtual work due to external loading.

GESA is a displacement-based finite element code, which means that its formulation is based on unknown displacements vs. a formulation that is based on unknown stresses or strains. The governing equations include three equilibrium equations given by Eq. (3.63) in vector form, six stress-strain constitutive equations given by Eq. (3.64) in the matrix form, and six strain-displacement relations given by Eq. (3.61) in vector form.

$$\frac{d\boldsymbol{t}_1}{dx} + \frac{d\boldsymbol{t}_2}{dy} + \frac{d\boldsymbol{t}_3}{dz} + (b_1\boldsymbol{i}_1 + b_2\boldsymbol{i}_2 + b_3\boldsymbol{i}_3) = \rho(\ddot{u}_1\boldsymbol{i}_1 + \ddot{u}_2\boldsymbol{i}_2 + \ddot{u}_3\boldsymbol{i}_3) \qquad (3.63)$$

Here, $\boldsymbol{i}_n$ are the unit vectors along xyz-coordinate system; b_n are body force densities; u_n are displacements; ρ is the mass density; $\boldsymbol{t}_n$ are traction vectors given in index form as $\boldsymbol{t}_n = \sigma_{mn}\boldsymbol{i'}_m$ with $n = 1,2,3$, and where σ_{mn} are Jaumann stresses, and $\boldsymbol{i'}_m$ are the unit vectors along the alternative $x'y'z'$- coordinate system.

$$\{\sigma_i\} = [Q]\{e_i\} \qquad (3.64)$$

Here, σ_i are Jaumann stresses; e_i are Jaumann strains; and $[Q]$ is a 6 x 6 material stiffness matrix.

Because GESA employs a displacement-based formulation, compatibility conditions are not required. Thus, there are a total of 15 governing equations are used to solve for 15 unknowns that include three displacements, six independent stresses, and six independent strains.

To analyze dynamics of large structural deformations, nonlinear transient dynamic analysis is performed. There are two commonly used approaches for transient analysis: mode superposition and direct integration. It is suggested by Pai [66] that the *direct time integration* method is a preferred one. In particular, GESA employs the *Newmark-β*

method for direct time integration. The *Newmark-β* method is an *implicit* method, which uses interpolation and can be unconditionally stable if appropriate parameters are used. Hence, it is the most popular implicit method used in recent finite element code developments.

Using GESA Code:

To do any analysis using GESA, one has to prepare a main program that consists of three parts. Part I usually requires no change. Part II requires creating the finite element mesh of the structure to generate global nodal coordinates, the connectivity matrix, the coordinate transformation matrix for each element or each node if it is a nonlinear problem, and assign the material, geometry, and element type numbers to each element; input the material properties to create material property matrix E; input the geometrical properties of elements used to create geometry property matrix A; input boundary conditions using the matrix BCC; input loading conditions; specify output degrees of freedom (DOFs) and display angles and dimensions; and, finally, input iteration control parameters for nonlinear problems and initial conditions for transient problems. Part III requires choosing the specific solution sequence. There are five main solution sequences available. They are linear analysis that includes static and modal analyses, steady-state response, and transient analysis; two nonlinear static analyses; nonlinear dynamic analysis for transient problems using the Newmark-β method; and modal analysis for statically deformed geometry. Figure 3-5 shows the flowchart for finite element analysis using GESA.

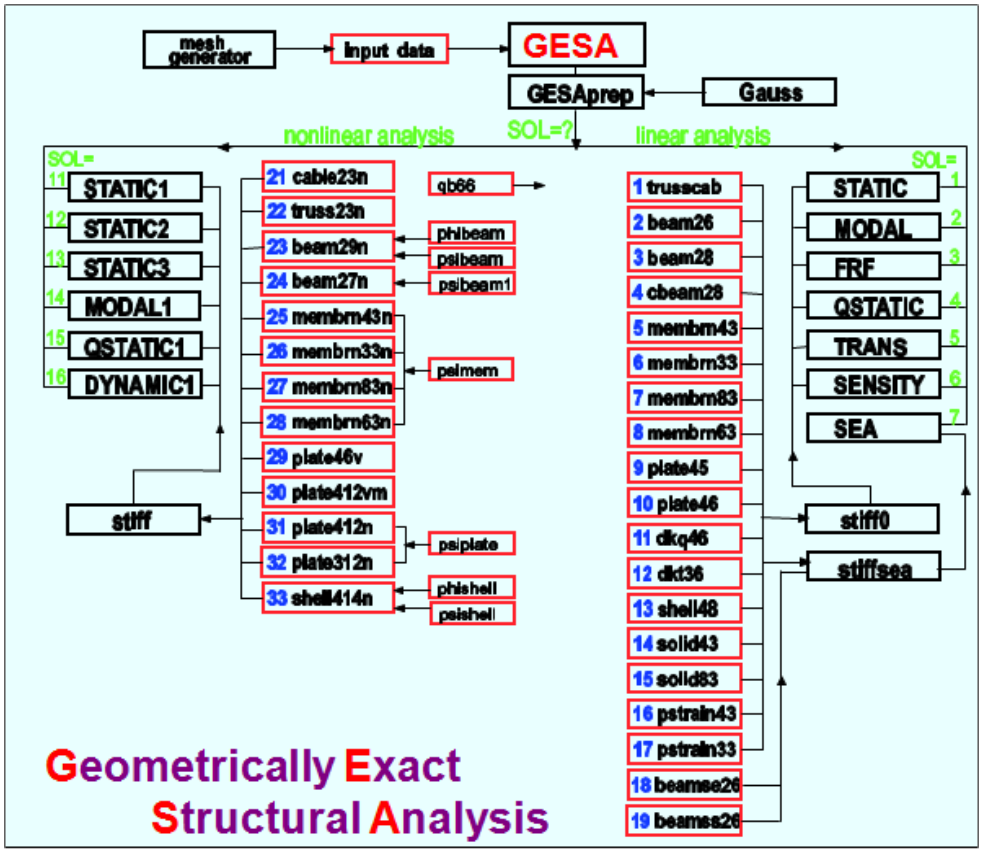

Fig. 3-5. Finite element analysis flowchart using GESA.

Coupling the Structural and Aerodynamic Modules:

The aeroelastic analysis of the MAV's flapping flight is accomplished by coupling the aerodynamic module and the structural module in iterative procedure. At first, GESA has to calculate wing deformation using assumed loading conditions. Then, at time step t_i, the deformation data is used as input into the aerodynamic module to attain the aerodynamic forces and moment of the wing that are being inputs into structural model to calculate deformations. The iteration is carried out until the structural response satisfies a particular convergence criterion.

CHAPTER 4

Numerical Simulations

Numerical simulations of the flapping flight are separated into two parts. At first, the simulation was performed without coupling the structural module with the aerodynamic module. The intent was to perform the experiment discussed later in Chapter 5 and compute aerodynamic forces and moments that act on the wing during the flight, eventually validating the results by numerical modeling. As it turned out, this approach did not allow the computing of the aerodynamic forces. The second numerical simulation was performed by combining the structural module with the aerodynamic module. The iterative approach allowed perform fully nonlinear simulations of the flapping flight and compute displacements and time-varying aerodynamic forces that act on the wing at any time instant.

4.1 Linear Dynamic Analysis

Because of time constraints and limited funding, the flying object chosen for experimental tests did not exactly fit the constraints of MAV design. It was a simple, radio-controlled ornithopter. The mesh of its wing structure was created using the geometry of this mechanical flyer, as shown in Fig. 4-1.

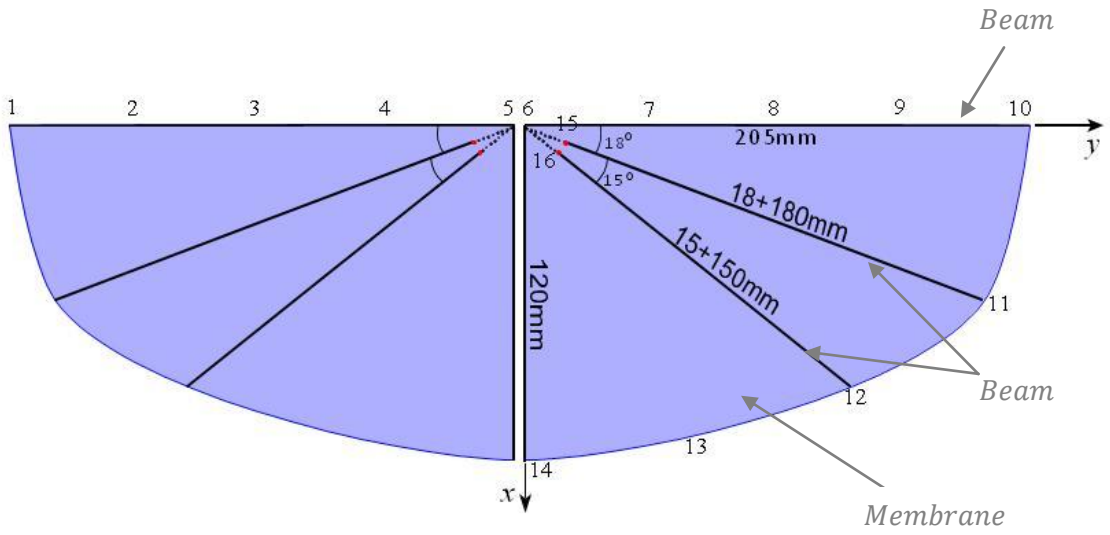

Fig. 4-1. Wings geometry for the linear dynamic analysis.

This geometry is shown with nodes, which correspond to the stickers that were placed for the experimental part that is described later in Chapter 5. Here, it is convenient for discussion to use sticker-nodes vs. mesh-nodes to talk about the structural part. There are three rods that make up the wing. The thickest one is the rod connecting nodes 6 and 10 that is denoted as $\overline{6-10}$. The other two rods connect nodes 15 and 11 denoted as $\overline{15-11}$ and nodes 16 and 12 denoted as $\overline{16-12}$.

The proposed material for all rods is graphite epoxy; and for membrane – Kapton film. Table 4-1 shows the summary of geometry and material properties for each beam element, and Table 4-2 shows the summary of geometry, material properties, and pretension values for membrane elements.

Table 4-1. Geometry and material properties for beam elements.

Rod	Ele–ment	Geometry			Material Properties		
		Length, $L\ (m)$	Width, $b\ (m)$	Thickness, $h\ (m)$	Density, $\rho\ (kg/m^3)$	Young Modulus, E (Pa)	Poisson's ratio, ν
$\overline{6-10}$	beam	0.205	1.5e–03	1.5e–03	1570	119e+09	0.3
$\overline{15-11}$	beam	0.18	0.3e–03	0.3e–03	1570	119e+09	0.3
$\overline{16-12}$	beam	0.15	0.3e–03	0.3e–03	1570	119e+09	0.3

Table 4-2. Geometry, material properties, and pretension values for membrane element.

Case	Ele–ment	Geom–ry	Material Properties			Pretension		
		Thickness, $h\ (m)$	Density, $\rho\ (kg/m^3)$	Young Modulus, E (Pa)	Poisson's ratio, ν	τ_1	τ_2	τ_{12}
1	plate	2.54e–05	1420	2.55e+09	0.34	0	0	0
2	memb	2.54e–05	1420	2.55e+09	0.34	0.02	0.02	0
3	membr	2.54e–05	1420	2.55e+09	0.34	1e–06	1e–06	0

The proposed mesh was created using three LINE2 mesh generators for the beams and three TRIANG3_3 mesh generators for the membrane. The wings were symmetric about x-axis. The mesh of undeformed geometry for the whole structure is shown in Fig. 4-2.

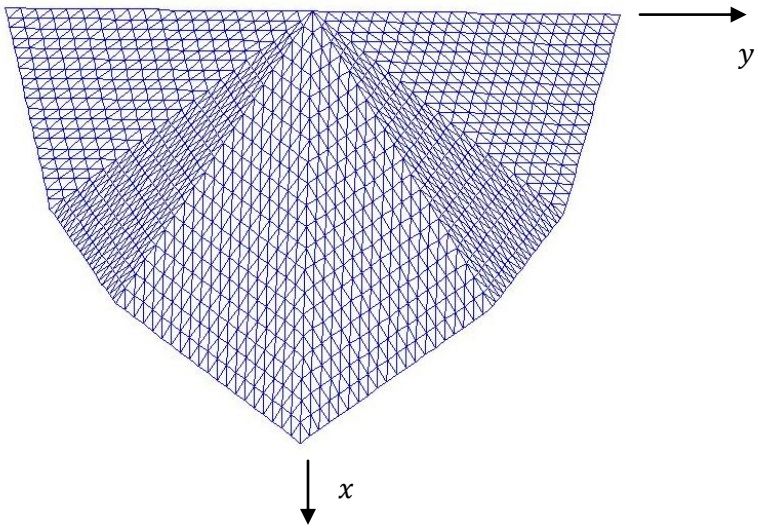

Fig. 4-2. The finite element mesh of the undeformed geometry of the tested ornithopter.

It is possible to make the analysis of the whole structure. However, for computational efficiency, only the right wing is modeled. There are 20 *eBeam26* elements used to model each beam on the wing. The membrane is assumed to be clamped on the x-axis only. All three beams are assumed to have only the rotational degree of freedom about the x-axis, torsional angle ϕ (see Fig. 4-8), at the origin, on node 6. The wing is analyzed using linear modal analysis for the three separate cases shown in Table 4-2, depending on how the membrane is represented.

For the first case, *ePlate36* elements with no pretension are used to model the membrane part of the wing. The Kapton film on the tested bird is actually slack, i.e., no pretension. If membrane elements without pretention are used to model the actual membrane, no mode shapes and no natural frequencies can be computed. The reason is that, because there is no pretension, the membrane cannot resist any transverse loads, including inertial loads. There are other plate elements are available in the GESA code. However, *ePlate36* is the only plate element of triangular shapes. The other plate elements are of rectangular

or quadrilateral shapes. Figure 4-3 shows the results of the linear modal analysis for beam/plate case: the first three vibration modes.

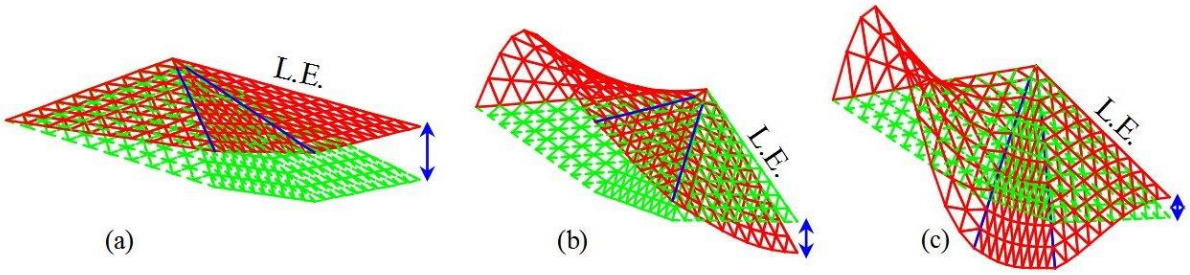

Fig. 4-3. Linear modal analysis of the beam-plate model: (a) first mode shape; (b) second mode shape; (c) third mode shape.

In Fig. 4-3, leading edge (L.E.) is the rod $\overline{6-10}$. It can be noticed from the figure that the other two rods, $\overline{15-11}$ and $\overline{16-12}$, do not bend. The first three corresponding natural frequencies are as follows: 0 Hz, 1.41 Hz, and 3.00 Hz. There is no possibility to achieve those natural frequencies experimentally even if a vacuum chamber is used. This is because the shape of the actual membrane is considerably affected by gravity, and, therefore, it cannot act like a flat plate. Thus, a new modeling has to be done.

For the second case, the membrane is modeled using membrane elements without slack, i.e., with a small pretension. If *eMembrn33*[9] elements are used, Figure 4-4 shows the results of the linear modal analysis for a beam-membrane model with pretension.

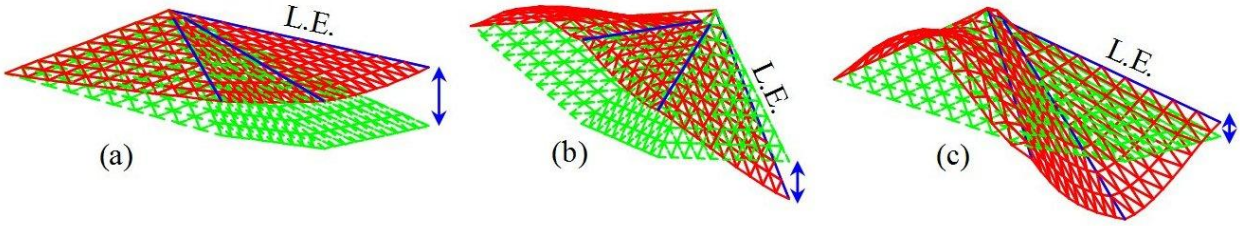

Fig. 4-4. Linear modal analysis for the beam-membrane model with pretension: (a) first mode shape; (b) second mode shape; (c) third mode shape.

[9] The linear *eMembrn33* element is not mentioned in Ref. [66]; only the nonlinear *eMembrn33n* element is available. Element *eMembrn33* has been developed later.

Similar to Fig. 4-3, rods $\overline{15-11}$ and $\overline{16-12}$ in Fig. 4-4 do not bend. The first three corresponding legible natural frequencies are as follows: 0.744 Hz, 2.84 Hz, and 4.31 Hz. These frequencies differ from those of the beam-plate case. Ideally, the first natural frequency should be zero, like that in the beam-plate case, because the first mode shape should be a rigid-body flapping mode. This error is due to the assumed pretension for the membrane. Pretension makes no slack at the trailing edge. Hence, there is a need to analyze the beam-membrane model with a very small pretension.

It should be noted that for cases with membrane the mode shapes shown are actually for the mode shape three, four, and five. This pertains to Fig. 4-4 and Fig. 4-5. This is due to the fact that the first two natural frequencies computed are not real numbers; and, therefore, the first two mode shapes are ignored.

For the third case, the membrane is modeled using membrane elements with a pretention much smaller than that in the second case, as shown in Table 4-2. Figure 4-5 shows the results of the linear modal analysis of the beam-membrane model with a minimal pretension.

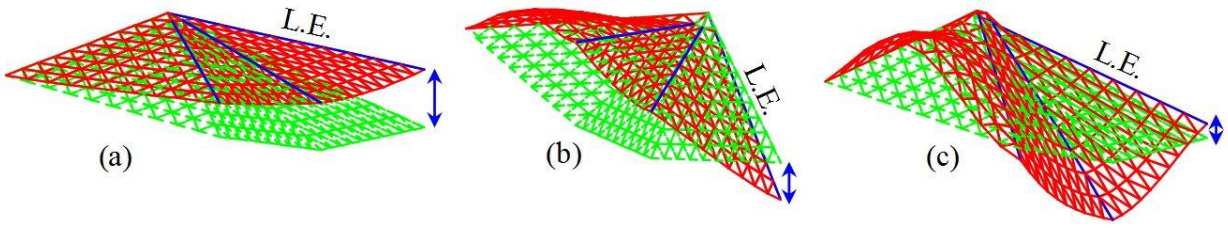

Fig. 4-5. Linear modal analysis of the beam-membrane with a minimal pretension: (a) first mode shape; (b) second mode shape; (c) third mode shape.

As the results in Fig. 4-5 show, the mode shapes are the same as those in the second case. However, the natural frequencies are very different. The first three corresponding legible natural frequencies for the third case are 0.0054 Hz, 0.0201 Hz, and 0.0306 Hz. These frequencies are smaller than those of the second case. In other words, the value of pretension determines the values of natural frequencies of the membrane. The smaller is the pretension, the smaller are the natural frequencies. This dependency is due to the fact that the bending strain energy is not accounted for in membrane elements.

Ideally, to match with the reality, the first natural frequency should be zero, like in the beam-plate model, because the first mode shape should be the one that resembles the rigid-body flapping. However, the error is due to two factors. First, the assumed pretension of the membrane gives no slack, especially at the trailing edge where the membrane is not attached to any rod. Second, in finite element modeling, the three beams and the x-axis split the membrane into separate partitions. The beams are much stiffer than the membrane. Thus, even with the small pretension, each partition is dominated by its local first mode shape with fixed local boundaries. Therefore, there is no possibility to simulate the first mode shape as the one for the rigid-body flapping.

In reality, slack membrane does not interact with the beams through elastic energy. Its morphing shape serves as a device only for gathering and transferring loads to the beams. Those loads include, first, the aerodynamic forces that occur due to the pressure difference between upper and lower surfaces of the wing and, second, the apparent air mass effect. Thus, the membrane's small inertia force can be treated as part of the aerodynamic load.

Regarding the mode shapes for all three cases, the experimental results discussed later in Chapter 5 show that the time-varying wing deformations at a low flapping frequency, particularly less than 5 Hz, consist of primarily the first three mode shapes for the beam-membrane model. Rods $\overline{15-11}$ and $\overline{16-12}$ in all three cases do not bend. Those rods serve as means to provide the change in the effective angle of attack though the inertia forces that are transferred by the membrane to the rod $\overline{6-10}$ and the x-axis.

Additionally, the linear transient analysis was performed at experimentally obtained flapping frequency of 5 Hz. The direct linear numerical simulations show that the beam-membrane model with uniform pretension of 0.02 N/m performs mostly as the beam-plate model with no pretension.

4.2 Fully Nonlinear Dynamic Analysis

The approach to use both experimental and numerical results in conjunction did not solve the problem of finding aerodynamic forces that act on a wing. Thus, as a different approach, there is a proposition to incorporate the aerodynamic model with the structural model. The aerodynamic solver uses the enhanced modified strip theory discussed in Chapter 3. The deformation data calculated by the structural module is used as input into the aerodynamic module, and then the computed aerodynamic forces are used as input into the structural module. The iteration continues until the structural response satisfies a certain convergence criterion. The initial input data for the structural module has to be taken from the experimental results. And, since the forces predicted by the enhanced modified strip theory of Kim *et al.* [44] agree well with the experimental results of

Okamoto and Azuma [64], the initial parameters as well as the wing type and shape are taken from those experimental results. The previous experimental work was done on a harmonically plunging rigid flat plate-like wing. Therefore, the geometry is different from the numerical simulations discussed in Sec. 4.1, and, thus, the corresponding mesh will have to be changed. The geometric, kinematic, aerodynamic, and material properties for the nonlinear numerical simulation are presented in Table 4-3.

Table 4-3. Geometric, kinematic, aerodynamic, and material properties for the nonlinear numerical simulation.

Parameter	Symbol/Formula	Value	Units
Wing span	b	0.32	m
Mean chord length	c_m	$25.4E$-03	m
Wing aspect ratio	$\mathcal{AR} = b/c_m$	12.6	
Wing thickness	$\hat{t}$	$0.45E$-0.3	m
Young's modulus	E	$127E$+09	Pa
Wing mass density	$\hat{\rho}$	4430	kg/m^3
Poisson's ratio	ν	0.36	
Free stream velocity	U	3.7	m/s
Air density	ρ	1.225	kg/m^3
Air dynamic (or absolute) viscosity	μ	$1.7892E$-05	$kg/(s \cdot m)$
Reynolds number	$Re = \frac{\rho U c_m}{\mu}$	6434	
Reduced frequency	$k = \frac{\pi f c_m}{U}$	0.26	
Excitation frequency of the plunging motion at the wing root	$\beta = (\Gamma) sin(\omega t)$ where Γ is the maximum flapping angle magnitude	$(\pi/9)\sin(\omega t)$	rad
Plunge angular velocity[10]	$\omega = 2\pi f$	$2\pi(12)$	rad/s
Flapping frequency	$f = 1/T$	12	Hz
Angle of the zero lift line	α_0	0	deg
Max *dynamic* stall angle	$(\alpha_{stall})_{max}$	8.67	deg
Min *dynamic* stall angle	$(\alpha_{stall})_{min}$	-8.67	deg
Leading edge suction efficiency	η_s	0.18	
Drag coefficient due to skin friction	$(C_d)_f$	0.068	
Drag coefficient due to cross-flow	$(C_d)_{cf}$	2.65	
Pitch angle of the flapping axis with respect to *U*	$\bar{\theta}_a$	0	deg
Mean pitch angle of chord with respect to the flapping axis	$\bar{\theta}_w$	0	deg

The wing is supposed to be rigid; thus, it is proposed to be modeled as a beam only. The proposed material shown in Table 4-3 is the graphite epoxy with slightly different

[10] Here, ω represents plunge angular velocity. However, in Table 2.2 in Chapter 2, ω represents pitch/plunge angular velocity.

material properties than shown in Table 4-1. The modeled geometry of the plate-like rectangular wing is shown in Fig. 4-6.

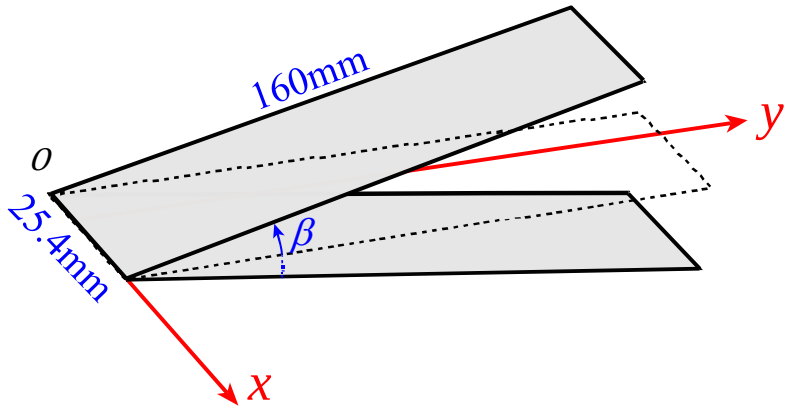

Fig. 4-6. The plate-like rectangular wing geometry for the nonlinear dynamic analysis.

The proposed mesh was created using LINE2 mesh generator. The numerical model is developed using the nonlinear beam element *eBeam29n*. There are 20 beam elements used to model the beam. At the origin, point O, the beam is assumed to have all DOFs fixed except the fifth one, w_x. The mesh of the undeformed geometry for the wing structure is shown in Fig. 4-7.

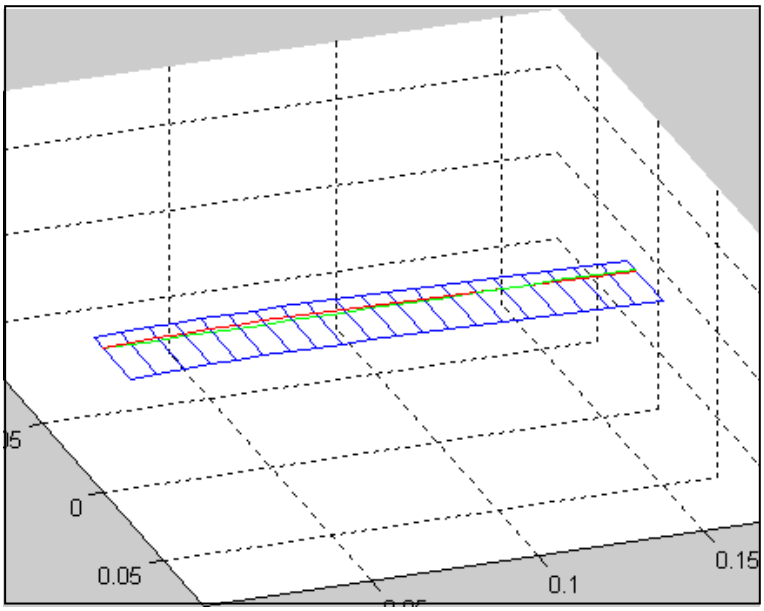

Fig. 4-7. The finite element mesh of the undeformed geometry of the plate-like wing.

Initially, the first three natural frequencies of the given wing are found. They are 15.2Hz (bending), 95.3Hz (bending), and 178.8Hz (torsion). Next, the dynamic analysis is performed. The flapping of the wing is modeled for three cases. First, the flapping is modeled without the aerodynamic forces and with the assumed modal damping ratio of 0.01 for each mode to account for material damping in the structure. Second, the flapping is modeled with coupled aerodynamic forces at $\bar{\theta}_a = 0^\circ$ and with no material damping. Third, it is modeled with coupled aerodynamic forces at $\bar{\theta}_a = 6^\circ$ and with no material damping. Nonlinear transient analysis by direct numerical integration using the Newmark-β method is performed, and results are shown next. The requested output nodes are 6, 11, 16, and 21 that correspond to the $^1/_4$ length of the wing, $^1/_2$ length of the wing, $^3/_4$ length of the wing, and the whole length of the wing, respectively.

The requested degrees of freedom (DOF) for the output are transverse, w, longitudinal, v, and in some cases the torsion angle about the beam's local x-axis, ϕ. Those DOFs are shown in Fig. 4-8.

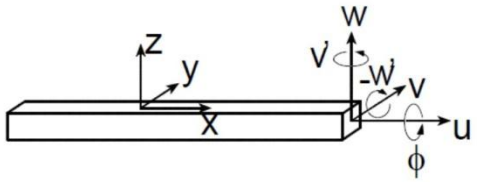

Fig. 4-8. DOFs at each node of an initially straight beam.

It should be noted that Fig. 4-8 is the simplified case of initially straight beam when only six DOFs are required. When the initially curved beam is used as in the case of using *eBeam29n* elements, three more DOFs at each node become necessary.

The results for the case without aerodynamic forces and with modal damping are shown in Fig. 4-9. The results for the cases with coupled aerodynamic forces and without modal damping are shown in Fig. 4-10 for $\bar{\theta}_a = 0^\circ$ and in Fig. 4-11 for $\bar{\theta}_a = 6^\circ$.

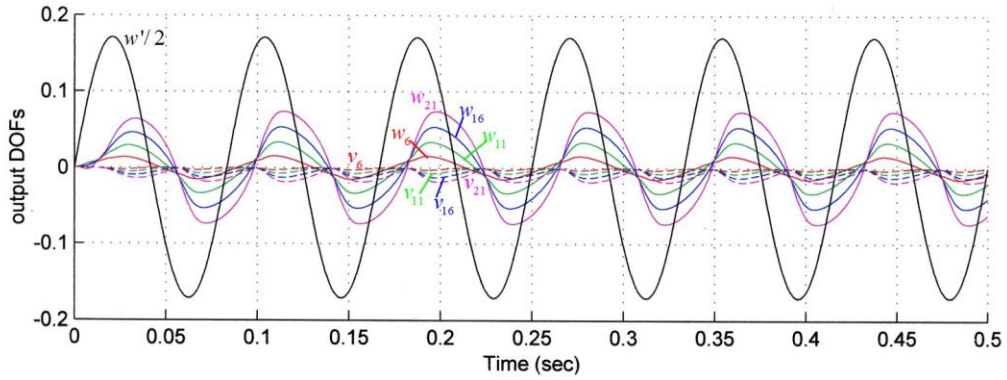

Fig. 4-9. Transverse and longitudinal displacements of nodes 6, 11, 16, and 21 for the case with no aerodynamic loads and modal damping ratio of 0.01.

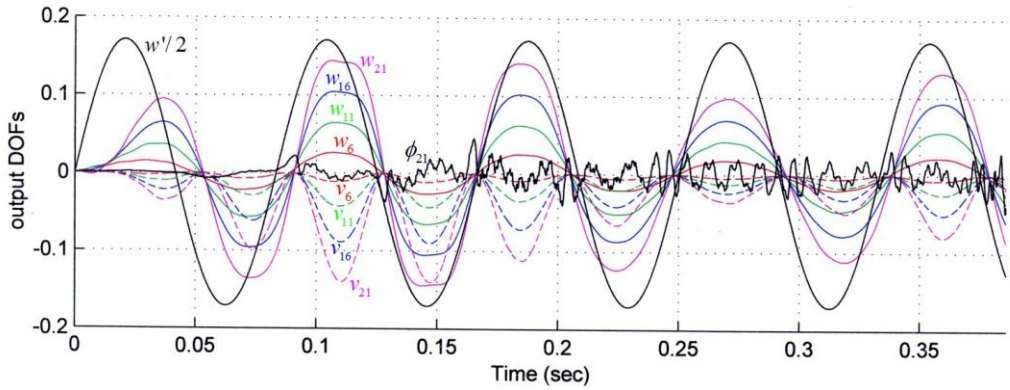

Fig. 4-10. Transverse and longitudinal displacements of nodes 6, 11, 16, and 21 for the case with aerodynamic loads with $\bar{\theta}_a = 0^\circ$ and no modal damping.

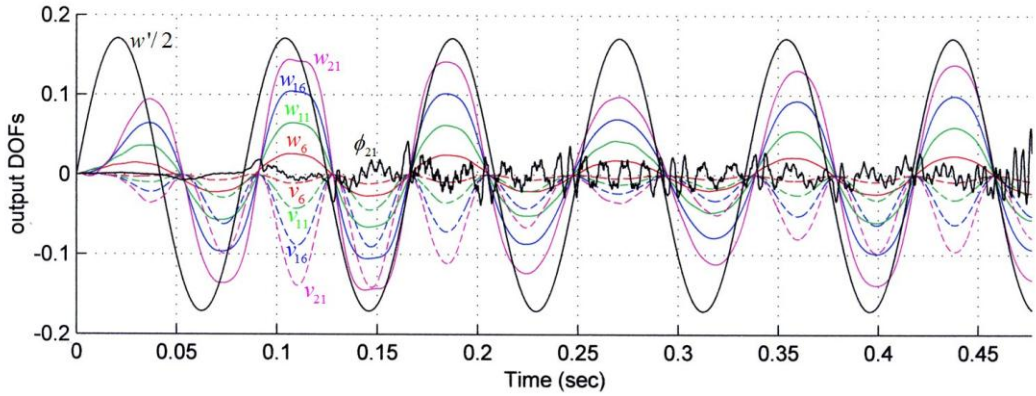

Fig. 4-11. Transverse and longitudinal displacements of nodes 6, 11, 16, and 21 for the case with aerodynamic loads with $\bar{\theta}_a = 6^\circ$ and no modal damping.

The transverse, w, and longitudinal, v, displacements of nodes 6, 11, 16, and 21 are shown in Figs. 4-9, 4-10, and 4-11, respectively. The rotational DOF of node 21, ϕ_{21}, is shown in Figs.4-10 and 4-11.The w' on all figures shows the harmonic flapping motion at the wing root, and it is equal to $w' = \sin(\beta)$.

It can be seen that in Fig. 4-9, as for the case with no coupled aerodynamics, the transverse and longitudinal vibration amplitudes increase with the increase in the distance from the wing root, as expected. The transverse amplitude is about 0.07 meters for node 21 and 0.01 meters for node 6. The maximum longitudinal amplitude of node 21 is 0.01 meter, and the minimum is about zero. The maximum longitudinal amplitude of node 6 is slightly below zero, and the minimum is about zero. The transverse vibrations oscillate around the absolute zero, and each longitudinal vibration oscillates around its own 'zero'. The maximum amplitude of longitudinal vibrations is the same for all nodes, and the minimum is the largest for the wing tip at node 21 and the smallest at node 6.

Also, it can be noticed from Fig. 4-9 that the transverse vibrations are of much larger amplitude than the longitudinal ones at the same node. In addition, the period of vibration is larger for the transverse vibrations than for the longitudinal ones, and the picks of wing deformation are constantly delayed with respect to the wing root excitation. Furthermore, the shown vibrations are not harmonic. This is due to the fact that multiple linear modes are excited and vibration amplitudes are relatively high.

Figures 4-10 and 4-11 represent the nonlinear fluid-structure analysis performed by using time-varying aerodynamic loads from the enhanced modified strip theory. It can be seen that cases with coupled aerodynamics shown in Figs. 4-10 and 4-11 and the case where aerodynamics is not included shown in Fig. 4-9 have some similarities and some differences. First, similarly to Fig. 4-9, the trend of vibration amplitude increase with the increase in the distance from the wing root in both directions continues for Figs. 4-10 and 4-11. However, the vibration amplitudes in both directions are usually larger than those for the case with no coupled aerodynamics. The largest transverse amplitude is about 0.13 meters at node 21, and about 0.03 meters at node 6. The largest longitudinal amplitudes at node 21 is 0.14 meters, and the minimum is about zero. The largest longitudinal amplitudes at node 6 are similar to those in Fig. 4-9, but the maximum is slightly below zero and the minimum is about zero. The influence of aerodynamic loads is obvious. Adding aerodynamics creates damping that lowers the first natural frequency of 15.2Hz to be close to the flapping frequency of 12Hz. This, in turn, causes the vibration amplitudes become larger than in the case without aerodynamic loads.

Second, similar to Fig. 4-9, the period of vibration on Figs. 4-10 and 4-11 is larger for the transverse vibrations than for the longitudinal ones. However, the picks of wing deformation are not delayed with respect to the wing root excitation as in the case with no aerodynamic loads. Third, similar to Fig.4-9, Figs. 4-01 and 4-11 show that the transverse vibrations oscillate about the absolute zero, and each longitudinal vibration oscillates about its own ‘zero’. However, the magnitude of those vibrations varies constantly, whereas the magnitude of vibrations in Fig. 4-9 for each node in each direction stays

relatively constant. As shown in Figs. 4-10 and 4-11, the displacement of the torsion angle of the wing tip located at node 21, ϕ_{21}, indicates the unsteadiness of the wing motion even after five flapping cycles.

Comparison of Figs. 4-10 and 4-11, which differ only by the pitch angle of the flapping axis with respect to the flight velocity, shows that at $\bar{\theta}_a = 6^{\circ}$, the unsteadiness of the flexural and torsional motions is more pronounced than that at $\bar{\theta}_a = 0^{\circ}$, and the transient time before the wing's motion gets stable at particular flapping frequency is greater than that at $\bar{\theta}_a = 0^{\circ}$.

4.3 Summary of Numerical Results

Results from the first series of numerical experiments show that, if the wing is modeled as a beam-membrane structure, at a relatively low flapping frequency, the aerodynamic forces that act on the wing will include the membrane's inertia forces. As confirmed by experimental results, at a low flapping frequency, particularly less than 5 Hz, the time-varying dynamic change of the wing mostly contains the first three mode shapes achieved by numerical simulation of the beam-membrane model. At a flapping frequency of 5 Hz, the direct linear numerical simulations show that the beam-membrane model with a uniform pretension of 0.02 N/m behaves most like the beam-plate model. Also, because rods $\overline{15-11}$ and $\overline{16-12}$ did not structurally participate in the dynamic change of the wing shape, the wing can be modeled with just the rod $\overline{6-10}$ in the beam-membrane model.

Results from the second series of nonlinear numerical experiments show the following. First, because aerodynamic damping reduces the first natural frequency to become close to the flapping frequency, the efficient flapping of a MAV should be at the frequency that is close to the first aerodynamically-damped frequency. However, because MAV's flight speed changes and because the frequency depends on the flight speed, the first aerodynamically-damped frequency would need to be adjusted according to the flight speed. Second, the comparison of the wing deformation with and without aerodynamic loads showed the delay of wing deformation peaks for the case with no aerodynamics and no delay with added aerodynamics. This indicates that the aerodynamic forces dominate the wing deformation over the structural deformation. This leads to the conclusion that aerodynamics is a major part, and, apparently, should be designed first. Third, the aerodynamic forces computed by the enhanced modified strip theory are the concentrated loads. Ideally, the smoothly distributed load along the chord of each strip is required.

Unfortunately, the distribution profile is not known, which could lead to a different deformed geometry profile. Thus, the proposed framework for the design of MAV is a reverse design process. First, it is reasonable to assume the aerodynamically efficient wing deformations for each time instant, and then design a wing structure that would satisfy the time-variable wing deformations assumed at the first step.

CHAPTER 5

Experimental Procedure and Results

Experimental testing appears to be an inalienable part of the study of such dynamically complicated motions as the flight of MAVs. In order to validate the numerically derived results, the experiment is administered. Such experiment, by nature, may require a lot of resources that can become cost prohibiting. Ideally, it would be useful to make an experiment on a real flying creature. Such experiments [74, 103, 116] have given researchers a better understanding of their flight kinematics. In our case, the experiment is done on an inexpensive flying mechanical bird with the help of a system of high-speed cameras in conjunction with signal processing techniques. The interest of this research is in the dynamics of flight, and, therefore, we intend to capture displacements of the wing, and then compute its acceleration, which would allow us to obtain forces that act on the wing. Initially, the experiment was going to provide the necessary parameters to calculate aerodynamic forces. Fig. 5-1 shows a schematic drawing of the forces acting on a flying bat that is attached to a string.

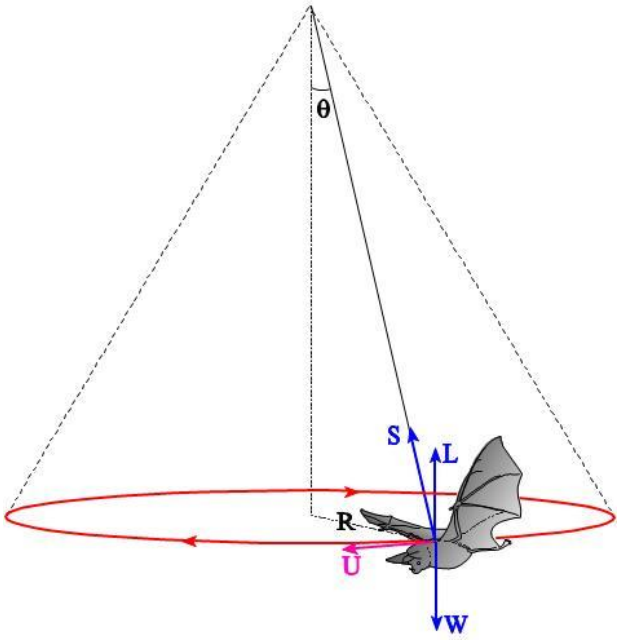

Fig. 5-1. The schematic drawing of the forces that act on a flying bat that is attached to a string.

Here, S is the tension force in the string; L is the lift force; W is the weight of the bat; R is the radius of the flying path; U is the free stream velocity or the flight speed; and θ is the angle of the string with respect to the vertical. The lift force can be computed as given by Eqs. (5.1) and (5.2).

$$S\,sin(\theta) = m\frac{U^2}{R} \tag{5.1}$$

$$L + S\cos(\theta) = W \tag{5.2}$$

Here, m is the mass of the bat. This simple approach did not turn out to be feasible. The proposed experiment contains gathering the data of wing displacements in order to calculate various kinematic parameters that can be used later as inputs for numerical

studies, and the time-varying displacement graphs can be used for comparison with numerical predictions.

This chapter describes the details of the experimental design for this research. It overviews the equipment used and the methodology, explains the experimental setup, and, finally, presents experimental results.

5.1 Measuring Equipment and Experimental Methodology

The requirements for our experimental equipment are such that they should allow us to accurately measure large time-varying 3D displacements of the wing without using contact sensors that can reduce the measurement accuracy. Prior studies of flight motion kinematics show the tendency to employ high-speed cameras in experiments. The plan to utilize camera-based motion analysis systems versus other noncontact sensors, such as laser sensors, eddy-current-based proximity sensors or others, is based on our previous work experience. For example, laser sensors are hard to follow when large rotational displacements are present, and eddy-current-based proximity sensors are only accurate for small displacements.

To accurately measure 3D wing motion of our mechanical bird, an EAGLE-500 motion analysis system is proposed and is shown in Fig. 5-2.

Fig. 5-2. EAGLE-500 camera-based motion analysis system.

This camera system consists of eight cameras, which employ recently developed complementary metal-oxide-semiconductor (CMOS) sensors that allow relatively high accuracy in tracking large rigid and elastic deformations of large mechanical systems, such as humans and animals. The proposed camera system is capable of making between 0.1 and 2000 frames per second (FPS) and is based on the principle of tracking of reflective spherical markers of a relatively large diameter, in average of about 20 millimeters. For measurements, the cameras have to be placed around the testing object in a user-defined testing volume. Then cameras have to be calibrated. The test object is then to be placed in this defined measurement volume. The EAGLE-500 camera system works in conjunction with real-time signal processing software EVaRT4.6 that processes and records the instantaneous *xyz* coordinates of the center of each retro-reflective marker.

Figure 5-3 shows the camera system as processed by the EVaRT4.6 signal processing software.

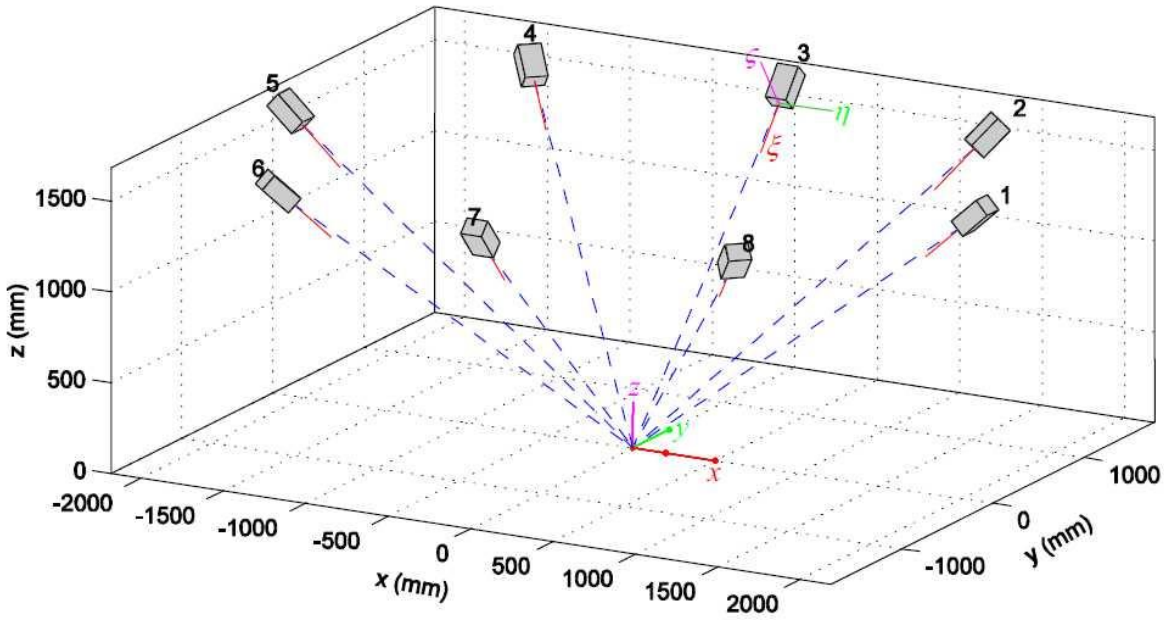

Fig. 5-3. EAGLE-500 camera motion analysis system as seen by EVaRT4.6 signal processing software.

The best experimental results are obtained if, at any instant, each marker is seen by at least two cameras, which allows having a continuous time trace for each marker. After the measurement is done, each marker's displacement, velocity and acceleration at each time instant can be obtained. The measured data can be exported in the ASCII format. Dynamic animation of the particular kinematics is also available.

However, in our case, we have encountered several obstacles to properly utilize the given camera motion system's ability to reach a high measurement accuracy. First, the tested object is relatively small in comparison to the camera system, as can be seen in Fig.5-4. (Dimensions of the tested MAV are shown later in Fig. 5-6.)

Fig. 5-4. The tested MAV: a radio-controlled (RC) ornithopter.

Second, our to-be-tested mechanical bird has wings that are made of a foil-like material, and therefore, cannot be approximated as a rigid body. Finally, in order to have a detailed representation of the wing geometry, we had to use smaller markers. A measurement theory based on photogrammetry was developed for this type of testing objects [68]. By using this measurement theory, it is estimated that the measurement error of the EAGLE-500 camera system is less than 0.25 mm for a measurement volume of $2m \times 2m \times 2m$. Therefore, the problem of measurement accuracy has been solved, and we can proceed with the measurement of large dynamic displacements of flapping wings.

5.2 Experimental Setup

The mechanical bird was tightened to a string, and hence it could only fly in a circular pattern, as shown in Fig. 5-5.

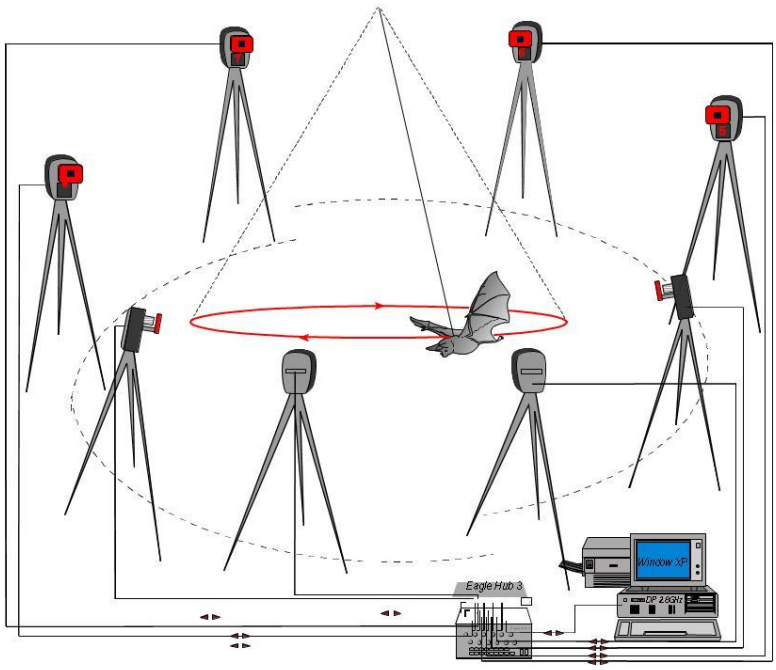

Fig. 5-5. Experimental setup for noncontact 3D dynamic measurement of the time-varying deformations of MAV flapping wings.

We placed 33 flat circular retro-reflective markers having a diameter of 6 mm on the upper surface of the wings. Locations of the markers and some of their corresponding location numbers are shown in Fig. 5-6.

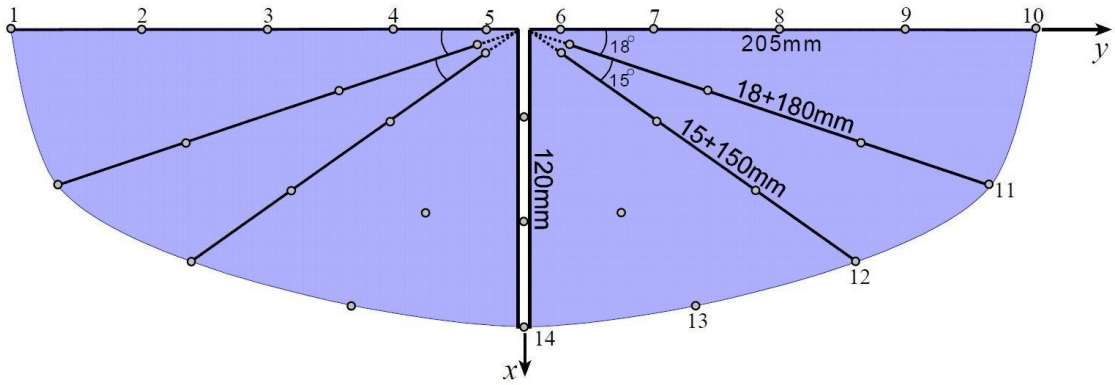

Fig. 5-6. Locations of retro-reflective markers on the wing surface and their corresponding location numbers for signal processing.

For each wing, five markers are placed on the leading edge, four markers are placed on each of the middle rods, two markers are placed on the foil-like wing surface, and three markers are placed on the center rod.

5.3 Experimental Results

After trying different frame rates, the best results were achieved at 300 FPS. At this frame rate, the camera system used the best resolution possible of 1280 x 1024 pixels. Signal processing software allowed us to make dynamic animation of the experiment that consisted of three thousand frames. Figure 5-7 shows ten separate time-varying wing geometries of the tested mechanical bird taken from this dynamic animation.

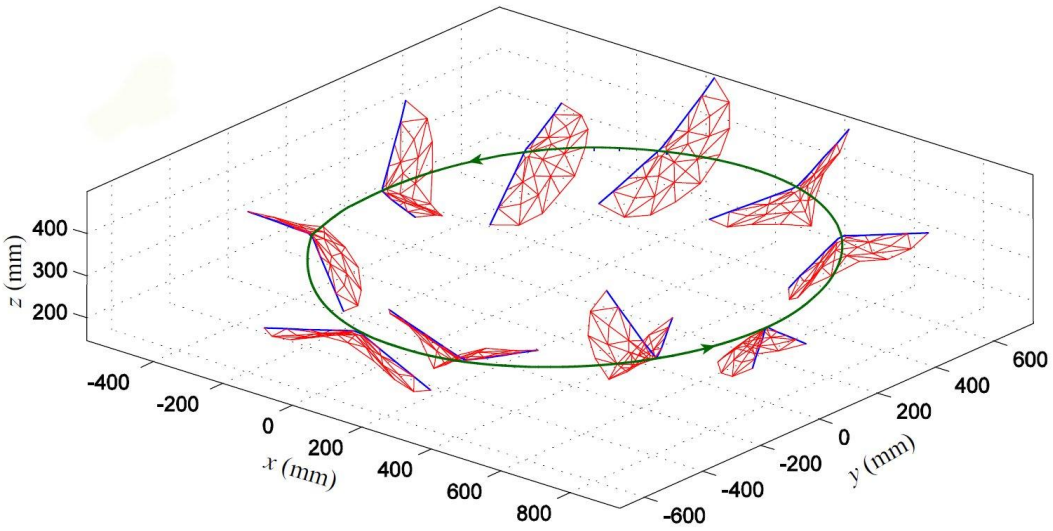

Fig. 5-7. Collection of ten separate time-varying wing geometries during the flapping flight.

Figure 5-7 shows that the wing surface is meshed. This was done by using the EVaRT4.6 software to connect markers to create the wing geometry. With the help of this meshed surface, we can see the dynamic deformations of wings during flight. Detailed time-varying displacements of certain nodes are shown next. Figure 5-8 shows the close-up view of the time-varying wing geometries during one flapping cycle.

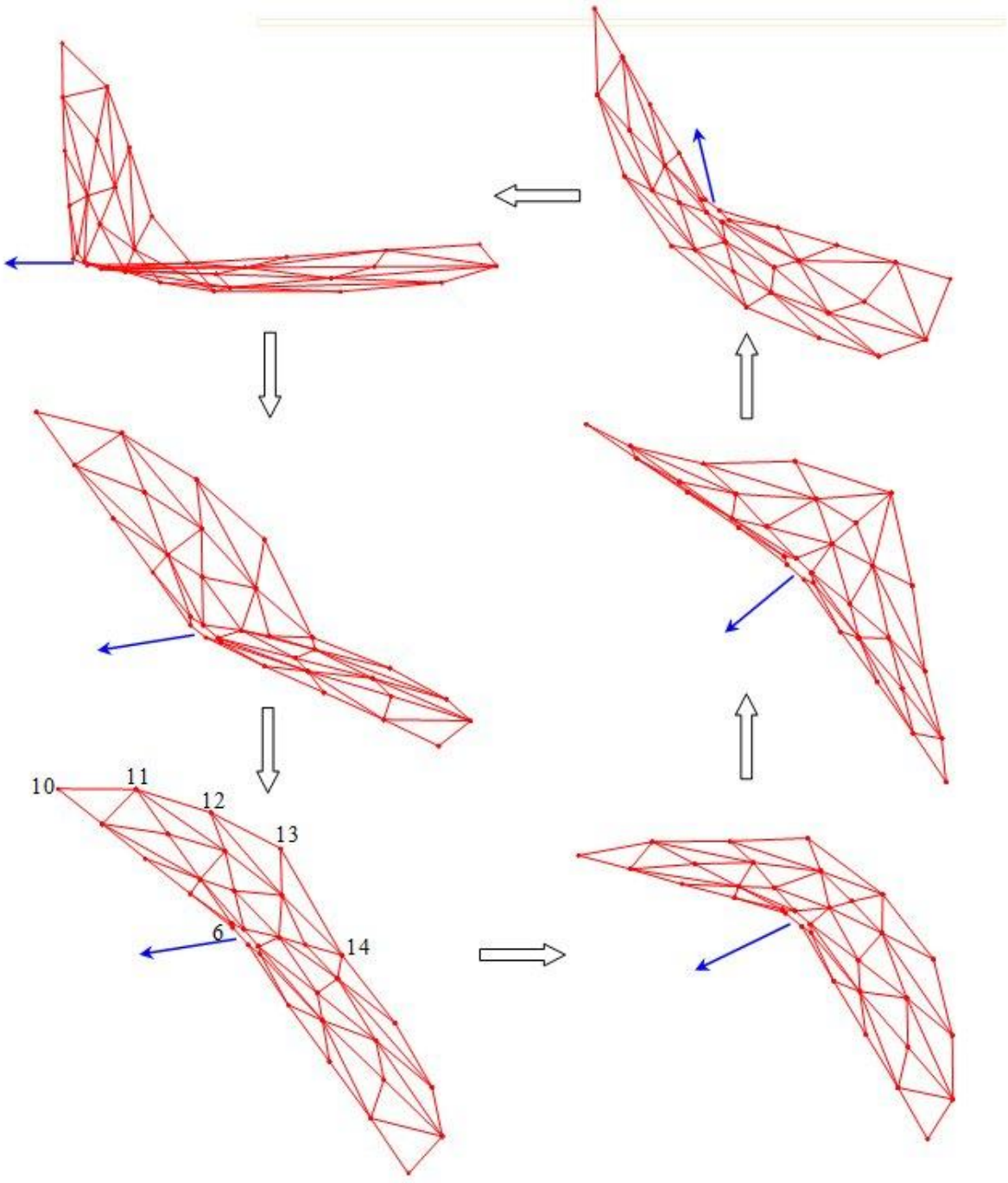

Fig. 5-8. Experimental time-varying geometries of the wing during one flapping cycle.

From Fig. 5-8, it can be seen that the leading edge, rod $\overline{6-10}$, as well as other two rods do not experience significant bending during flapping, which agrees with the numerical simulation presented in Chapter 4.

Figure 5-9 shows the time-varying *x*-location of markers 10 through 13.

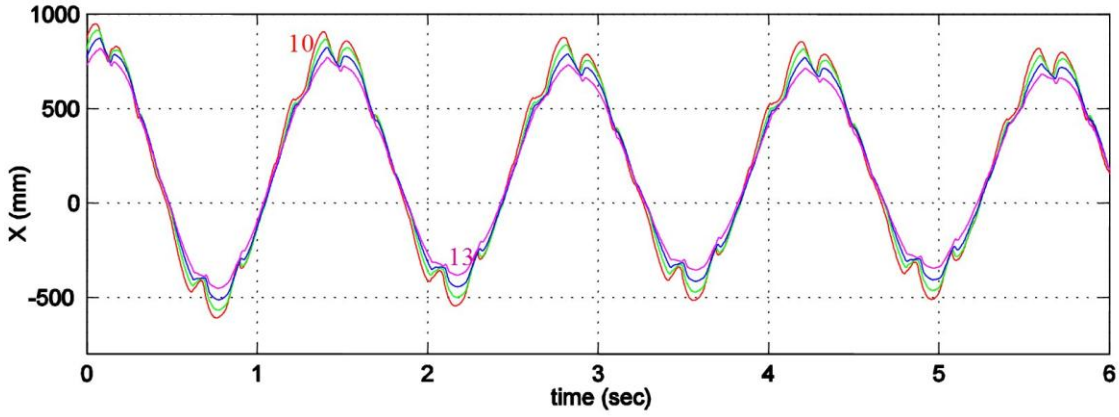

Fig. 5-9. Experimental results: time-varying x-location of markers 10-13.

It can be seen from Fig. 5-9 that marker 10 has the largest amplitude in x-direction that occurs on the first period. Therefore, this marker can be considered for calculation of the radius of MAV's flying path. Marker 10 has a maximum of about 0.92 m and a minimum of about -0.6 m. Therefore, the diameter of the flying circle is calculated by summing up the maximum and the minimum values of marker 10, and then subtracting the length of the rod $\overline{6-10}$, which is 0.205 m. Therefore, the diameter of the flying path is about 1.3 m. The length of the flying path is calculated as πD (where D is the diameter of the path) and is equal to about 4.77 m. From the same Fig. 5-9, we see that the period is about 1.5 seconds, and therefore, the velocity of the flying MAV is about 3.18 m/s. This velocity is a steady-state velocity that was achieved at the given experimental setup. More trials were performed to achieve adequate experimental results at higher speeds. However, at higher speeds, the wing's upper surface that is intended to be seen by at least two cameras at any instant was moved to a plane that was not able to be seen by some

cameras. A different experimental setup with larger facility with larger quantity of cameras is suggested.

Figure 5-10(a) shows the time-varying *z*-locations of markers 6 and 10 through 14, and Fig. 5-10(b) shows the time-varying *z*-locations of markers 6 through 10.

(a)

(b)

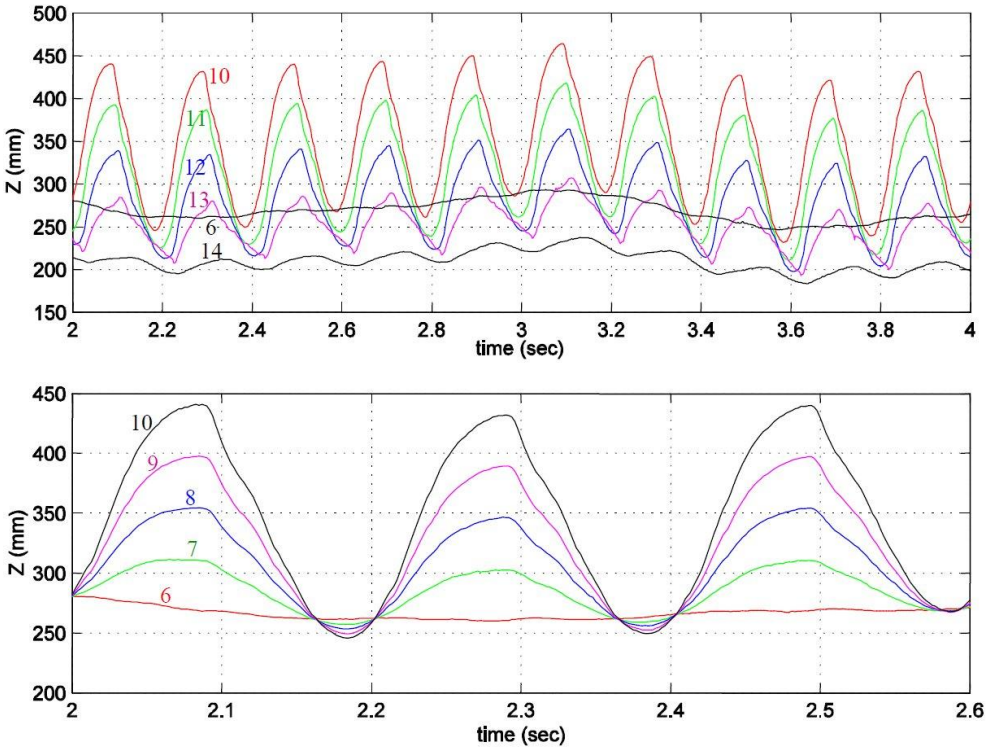

Fig. 5-10. Experimental results: (a) time-varying z-location of markers 6 and 10-14; (b) time-varying z-locations of markers 6-10.

By analyzing Fig. 5-10(a), we can see that markers 10 through 13 reach their respective maximums in *z*-direction at different times. This indicates that the flapping motion contains at least two first modes that were shown earlier in Figs. 4-3 and 4-4 in Chapter 4. From Fig. 5-10(a), we also can see that the period of flapping is about 0.2 seconds, and

therefore, the flapping frequency is calculated as $^1/_T$ (where T is the flapping period) and is equal to 5 Hz. Taking marker 6 as a reference node, we can see that markers 10 through 13 oscillate about it. Also, knowing that marker 10 is located on the tip of the leading edge of the wing, we can see that the upstoke takes more time than the downstroke. In other words, the angular velocity of the wing about x-axis is slower during upstroke than during downstroke. This observation agrees with the experimental observations of small birds at slow speeds [35]. In our case, mechanically, it can be explained by the use of the crank mechanism on the DC motor's shaft.

It's also possible to calculate the reduced frequency, k, and Reynolds number, *Re*. The reduced frequency is given as $\frac{\pi f c_m}{V_\infty}$, and *Re* is given as $\frac{\rho V_\infty c_m}{\mu}$. The mean chord length is calculated from the geometry given in Fig. 5-6 to be about 0.1036 m. Then, for air density of $1.225\ kg/m^3$ and air dynamic viscosity of $1.7892 \cdot 10^{-5} kg/(s \cdot m)$, the reduced frequency is calculated to be about 0.51, and *Re* is about 22,600.[11]

Since markers 6 and 10 are located on the leading edge, the maximum flapping angle can be calculated from their time traces shown in Fig. 5-10(b). It is estimated to be about 40º. The angle of the flapping axis with respect to the free stream velocity, $\bar{\theta}_a$, is also calculated from Fig. 5-10(b) by using the time traces of points 6 and 14, which are located on the bird's relative x-axis. It is estimated to be about 26º. Figs. 5-10(b) and 5-8 show that the leading edge, rod $\overline{6-10}$, does not have significant bending during flapping, and this agrees with the numerical simulations described in Chapter 4.

[11] Air density and air dynamic viscosity are taken from the Table 4-3 in Chap. 4.

5.4 Summary

The experimental procedure based on the developed noncontact measurement theory for static/dynamic testing of flexible multibody systems allows visualizing the flapping flight by using a high-speed camera system and the accompanied software package. Dynamically deformed wing geometries are obtained by tracing the three-dimensional instantaneous coordinates of retro-reflective markers adhered to the wing upper surfaces. This approach can be used for future experimental work. The results show that, besides obtaining wing deformed geometries, the flight kinematics can be calculated as well. However, the setup may require changes when it is used for measurement of MAVs at high flying speeds because it is difficult to capture the displacements of the entire wing. Moreover, using this experiment alone did not allow the calculation of aerodynamic forces. Thus, experimental results should be used in conjunction with numerical simulations for better understanding of flapping wing dynamics and mechanics.

CHAPTER 6

Conclusions and Recommendations

This chapter summarizes the work done on numerical simulations and experiments on flapping wing dynamics. Also, some topics for future work are also presented.

6.1 Conclusions

This research offers a perspective into progress and challenges associated with the design of micro air vehicles and investigates the flapping flight dynamics of the MAV's forward flight. The research attempts to systematize the available scientific information for MAV development. Also, it presents a new experimental approach for the development of MAVs that can also be used in other areas of engineering where dynamic results are required. Finally, the research utilizes a fully nonlinear finite element analysis coupled with the aerodynamic solution technique to investigate the deformation of the wing during flapping flight.

The experimental method is based on using noncontact sensors to measure the displacements of flapping wings during flight. The procedure is based on the developed noncontact measurement theory for static/dynamic testing of flexible multi-body systems which allows visualizing flapping flight by using a high-speed camera system and the accompanying software package. Dynamically deformed wing geometries are obtained by tracing the three-dimensional instantaneous coordinates of retro-reflective markers adhered to the wing upper surfaces.

The numerical simulations of the flapping-wing dynamics were performed by using a total-Lagrangian displacement-based nonlinear finite element code, GESA (Geometrically Exact Structural Analysis), which is capable of solving for large-amplitude dynamic elastic displacements and rotations of highly flexible wing structures. The GESA structural module was coupled with an aerodynamic module to produce results that incorporated not only the structural dynamics of the wing, but also the time-variable aerodynamic loads. The aerodynamic solver is based on the enhanced modified strip theory.

The experimental results show that, besides obtaining wing deformed geometries, the flight kinematics can be calculated as well. However, the setup may require changes when it is used for measurement of MAVs at high flying speeds because it is difficult to capture the displacements of the entire wing. Moreover, using this experiment alone did not allow the calculation of aerodynamic forces. Thus, experimental results should be used in conjunction with numerical simulations for better understanding flapping wing dynamics and mechanics.

Numerical simulations of flapping flight are separated into two parts. First, the simulation was performed without coupling the structural module with the aerodynamic module. The geometry of the numerical model was created using MAV, which was tested experimentally. The second numerical simulation was performed by combining the structural module with the aerodynamic module. The iterative approach allowed performing fully nonlinear simulations of flapping flight and computing displacements

and time-varying aerodynamic forces that act on the wing at a particular instant. This time the geometry of the numerical model was a rigid plate-like rectangular wing. The first numerical study was done for *Re* around 22,600, and the second numerical study was done for *Re* around 6,400.

Results from the first series of numerical experiments show that, if the wing is modeled as a beam-membrane structure, at a relatively low flapping frequency, the aerodynamic forces that act on the wing will include the membrane's inertial forces. As confirmed by experimental results, at a low flapping frequency, particularly less than 5 Hz, the time-varying dynamic change of the wing mostly contains the first three mode shapes achieved by numerical simulation of the beam-membrane model. At a flapping frequency of 5 Hz, the direct linear numerical simulations show that the beam-membrane model with a uniform pretension of 0.02 N/m behaves most like the beam-plate model. Also, as results show, for the beam-membrane model, MAV can be built using the front rod instead of the initially given rods.

Results from the second series of nonlinear numerical experiments show the following. First, because aerodynamic damping reduces the first natural frequency to become close to the flapping frequency, the efficient flapping of a MAV should be at the frequency that is close to the first aerodynamically-damped frequency. However, because MAV's flight speed changes and because the frequency depends on the flight speed, the first aerodynamically-damped frequency would need to be adjusted according to the flight speed. Second, the comparison of the wing deformation with and without aerodynamic loads showed the delay of wing deformation peaks for the case with no aerodynamics and

no delay with added aerodynamics. This indicates that the aerodynamic forces dominate wing deformation over the structural deformation. This leads to the conclusion that aerodynamics is the major factor, and, apparently, should be designed first. Third, the aerodynamic forces computed by the enhanced modified strip theory are the concentrated loads. Ideally, a smoothly distributed load along the chord of each strip is required. Unfortunately, the distribution profile is not known, which could lead to a different deformed geometry profile. Thus, the proposed framework for the design of MAV is a reverse design process. First, it is reasonable to assume the aerodynamically efficient wing deformations for each time instant, and then design a wing structure that would satisfy the time-variable wing deformations assumed at the first step.

6.2 Recommendations for Future Work

Since the experimental approach produced adequate results, it should be incorporated into future research. It would be necessary to perform more experiments using different wing geometries. Also, flight patterns should be more flexible: MAV's have to be able to fly not only in the circular manner. Different speeds should be investigated as well.

Next, all the experimental work should be numerically modeled and possibly validated by using the nonlinear structural module coupled with the aerodynamic module. Studies for different values of the reduced frequency as well as for different Reynolds numbers have to be performed. Possibly, numerical studies should also include the aspect ratio as a flight variable in the research. Also, it will be necessary to incorporate the pitching

motion, and numerical studies should include a combined plunging/pitching motion of wings.

Eventually, the proposed reversed design technique will have to be developed and incorporated into the research. It may include the recording of the ideally-efficient flight of a real bird or insect that later can be used for the development of efficient flapping flight using numerical modeling.

BIBLIOGRAPHY

1. Agrawal, A., Agrawal, S. K., 2009, "Design of bio-inspired flexible wings for flapping- wing micro-sized air vehicle applications." *Advanced Robotics* **23(7-8)**: 979–1002.

2. Altshuler, D. L., Dudley, R., Ellington, C. P., 2004, "Aerodynamic forces of revolving hummingbird wings and wing models." *Journal of Zoology* **264**:327-332.

3. Ammoo, M. S., Dahalan, M. N., *Micro air vehicle: technology review and design study*, Department of Aeronautic and Automotive, Faculty of Mechanical Engineering, Universiti Teknologi Malaysia, 81310 Skudai, Johor, http://eprints.utm.my/318/1/MohdShariffAmmoo2006_MicroAirVehicleTechnologyReview.pdf (Aug. 10, 2011)

4. Anderson, J. D., 2007, *Fundamentals of Aerodynamics*, 4th Edition, McGraw Hill, New York, NY, pp. 397, 74, 354, 795.

5. Anderson, J. M., Streitlien, K., Barrett, D. S., Triantafyllou, M. S., 1998, "Oscillating foils of high propulsive efficiency." *Journal of Fluid Mechanics* **360**:41-72.

6. Aono, H., Chimakurthi, S. K., Cesnik, C. E. S., Liu, H., Shyy, W., 2009, "Computational modeling of spanwise flexibility effects on flapping wing aerodynamics." *47th AIAA Aerospace Sciences Meeting Including the New Horizons Forum and Aerospace Exposition*, AIAA 2009–1270, Orlando, FL, January 2009.

7. Aono, H., Chimakurthi, S. K., Wu, P., Sällström, E., Stanford, B. K., Carlos, E. S. Cesnik, C. E. S., Ifju, P., Ukeiley, L., Shyy, W., 2010, "A computational and experimental study of flexible flapping wing aerodynamics." *48th AIAA Aerospace Sciences Meeting Including the New Horizons Forum and Aerospace Exposition*, AIAA 2010-554, Orlando, FL, January 2010.

8. Bergou, A. J., Xu, S., Wang, Z. J., 2007, "Passive wing pitch reversal in insect flight." *Journal of Fluid Mechanics* **591**:321–337.

9. Breden, E., *Available Hummingbird Images List*, The Otter Side, Harlingen, Texas, April 17, 2011. http://otterside.com/htmfiles/hummer.htm (Aug. 10, 2011)

10. Chai, P., Millard, D., 1997, "Flight and size constraints: Hovering performance of large hummingbirds under maximal loading." *The Journal of Experimental Biology* **200**:2757-2763.

11. Chandar, D., Damodaran, M., 2009, "Computational fluid-structure interaction of a flapping wing in free flight using overlapping grids." *27th AIAA Applied Aerodynamics Conference*, AIAA 2009–3849, San Antonio, TX, June 2009.

12. Chimakurthi, S. K., Tang, J., Palacios, R., Cesnik, C. E. S., Shyy, W., 2009, "Computational aeroelasticity framework for analyzing flapping wing micro air vehicles." *AIAA Journal* **47(8)**:1865–78.

13. Davis, W. B., Schmidly, D. J., *Brazilian Free-tailed Bat*, The Mammals of Texas - Online Edition, Texas Tech University, Lubbock, TX. http://www.nsrl.ttu.edu/tmot1/tadabras.htm (Aug. 10, 2011)

14. DeLaurier, J. D., 1993, "An aerodynamic model for flapping-wing flight." *Aeronautical Journal* **97(964)**:125-130.

15. Dial, K. P., 1992, "Avian forelimb muscles and non-steady flight: Can birds fly without using the muscles in their wings." *Auk* **109**:874-885.

16. Dickinson, M. H., Götz, K. G., 1993, "Unsteady aerodynamic performance of model wings at low Reynolds numbers." *Journal of Experimental Biology* **174**:45-64.

17. Dickinson, M. H., 1996, "Unsteady mechanisms of force generation in aquatic and aerial locomotion." *American Zoology* **36**:537-554.

18. Dickinson, M. H., Lehman, F.-O., Sane, S. P., 1999, "Wing rotation and the aerodynamic basis of insect flight." *Science* **284**:1954-1960.

19. Dickson, W. B., Dickinson, M. H., 2004, "The effect of advance ratio on the aerodynamics of revolving wings." *Journal of Experimental Biology* **207**:4269-4281.

20. Ehrlich, P. R., Dobkin, D. S., Wheye, D., *Wing Shapes and Flight*, Stanford's Academic Reserve, Stanford University, Stanford, CA, 1988. http://www.stanford.edu/group/stanfordbirds/text/essays/Wing_Shapes.html (Aug. 10, 2011)

21. Ellington, C. P., 1984, "The aerodynamics of insect flight. III. Kinematics." *Philosophical Transactions of the Royal Society of London* Series B, **305**:41-78.

22. Ellington, C. P., van den Berg, C., Willmott, A. P., Thomas, A. L. R., 1996, "Leading-edge vortices in insect flight." *Nature* **384**: 626-630.

23. Erickson, L., McGowan, K., Powell, H., Savoca, M., Sedgwick, C., *Bird Guide*, All About Birds/The Cornell Lab of Ornithology, Cornell University, Ithaca, NY, 2011. http://www.allaboutbirds.org/guide/search (Aug. 10, 2011)

24. Frampton, K. D., Goldfarb, M., Monopoli, D., Cveticanin, D., edited by Mueller, T. J., 2001, "Passive aeroelastic tailoring for optimal flapping wings." *Fixed and Flapping Wing Aerodynamics for Micro Air Vehicle Applications*, *Progress in Astronautics and Aeronautics*, AIAA, Reston, VA, **195**:473–482.

25. Gopalakrishnan, P., 2008, *Unsteady Aerodynamic and Aeroelastic Analysis of Flapping Flight*, Ph.D. Dissertation, Department of Mechanical Engineering, Virginia Polytechnic Institute and State University, Blacksburg, VA.

26. Gordnier, R., 2008, "High fidelity computational simulation of a membrane wing airfoil." *46th AIAA Aerospace Sciences Meeting and Exhibit*, AIAA-2008-614, January 2008, Reno, NV.

27. Gough, G.A., Sauer, J.R., Iliff, M., *Patuxent Bird Identification Infocenter,* Patuxent Wildlife Research Center, Laurel, MD, Version 97.1, 1998. http://www.mbrpwrc.usgs.gov/id/framlst/infocenter.html (Aug. 10, 2011)

28. Gough, G.A., Sauer, J.R., Iliff, M., *Rufous hummingbird Selasphorus rufus*, Patuxent Wildlife Research Center, Laurel, MD, Version 97.1, 1998. http://www.mbr-pwrc.usgs.gov/id/framlst/i4330id.html (Aug. 10, 2011)

29. Greenewalt, C. H., 1960, *Hummingbirds*, Doubleday & Company, Inc., Garden City, New York, p.205.

30. Greenewalt, C. H., 1960, "The wings of insects and birds as mechanical oscillators." *Proc. Am. Philos. Soc.* **104**:605-611.

31. Guvernyuk, S. V., Dynnikova, G. Ya., 2007 "Modeling the flow past an oscillating airfoil by the method of viscous vortex domains." *Fluid Dynamics* **42(1)**:1-11.

32. Hamamoto, M., Ohta, Y., Hara, K., Hisada, T., 2007, "Application of fluid–structure interaction analysis to flapping flight of insects with deformable wings." *Advanced Robotics* **21(1–2)**:1–21.

33. Harris, M., Naumann, R., Kirschbaum, K., *Archilochus colubris/Ruby-Throated Hummingbird*, Animal Diversity Web, University of Michigan Museum of Zoology, Ann Arbor, MI, 2000. http://animaldiversity.ummz.umich.edu/site/accounts/information/Archilochus_colubris.html (Aug. 10, 2011)

34. Hedenström, A., Van Griethuijsen, L., Rosen, M., Spedding, G. R., 2006, "Vortex wakes of birds: Recent developments using digital particle image velocimetry in a wind tunnel." *Journal of Animal Biology* **56(4)**:535-549.

35. Hedrick, T. L., Usherwood, J. R., Biewener, A. A., 2004, "Wing inertia and whole-body acceleration: An analysis of instantaneous aerodynamic force production in cockatiels (*Nymphicus hollandicus*) flying across a range of speeds." *Journal of Experimental Biology* **207**: 1689-1702.

36. Hilton, B. Jr., *Hummingbird Size and Mass*, Operation RubyThroat: The Hummingbird Project/ Hilton Pond Center for Piedmont Natural History, York, SC, 20 May 2011. http://www.rubythroat.org/RTHUSizeMain.html (Aug. 10, 2011)

37. Hoerner, S. F., 1965, Skin-friction drag, *Fluid-Dynamic Drag*, Published by the Author, Brick Town, NJ, pp. 2-1 to 2-16.

38. Ishihara, D., Horie, T., Denda, M., 2009, "A two-dimensional computational study on the fluid-structure interaction cause of wing pitch changes in dipteran flapping flight." *Journal of Experimental Biology* **212**:1–10.

39. Jones, K. D., *Bio-inspired design of flapping-wing vehicles*, Department of Mechanical and Astonautical Engineering, Monterey, CA, International Symposium on Flying Insects and Robots, Monte Verita, Ascona, Switzerland, Aig. 2007. http://fir.epfl.ch/docs/FIR_proceedings_online.pdf (Aug. 10, 2011)

40. Jones, R., 1990, *Wing Theory*, Princeton University Press, Princeton, N.J.

41. von Karman, T., Burgers, J.M., edited by Durand, W. F., 1934, "General aerodynamic theory—perfect fluids." *Aerodynamic Theory* **2**, Julius Springer, Berlin.

42. Kim, D., Choi, H., 2007, "Two-dimensional mechanism of hovering flight by single flapping wing." *Journal of Mechanical Science and Technology* **21**(1):207-221.

43. Kim, D., Lee, J.-S., Lee, J.-Y., Han, J., edited by Ahmadian, M., 2008, "An aeroelastic analysis of a flexible flapping wing using modified strip theory." *Active and Passive Smart Structures and Integrated Systems*, *Proceedings of the SPIE*, **6928(69281O)**.

44. Kim, D., Lee, J.-S., Lee, J.-Y., Han, J., 2011, "Improved aerodynamic model for efficient analysis of flapping-wing flight." *AIAA Journal* **49(4)**:868-872.

45. Kuethe, A. M., Chow, C.-Y., 1986, The finite wing, *Foundations of Aerodynamics*, 4th Edition, John Wiley, New York, pp. 145-164.

46. Lai, J. C. S., Platzer, M. F., 1999, "Jet characteristics of a plunging airfoil." *AIAA Journal* **37**:1529-1537.

47. Lai, J. C. S., Platzer, M. F., 2001, "Characteristics of a plunging airfoil at zero freestream velocity." *AIAA Journal* **39(3)**:531-534.

48. Lentink, D., *Novel micro aircraft inspired by insect flight*, Experimental Zoology Group, Wageningen University, Wageningen, The Netherlands. International Symposium on Flying Insects and Robots, Monte Verita, Ascona, Switzerland, Aug. 2007. http://fir.epfl.ch/docs/FIR_proceedings_online.pdf (Aug. 10, 2011)

49. Lentink, D., Müller, U. K., Stamhuis, E. J., de Kat, R., van Gestel, W., Veldhuis, L. L. M., Henningsson, P., Hedenström, A., Videler, J. J., van Leeuwen, J. L., 2007, "How swifts control their glide performance with morphing wings." *Nature* **446**:1082-1085.

50. LeVeque, R. J., Adams, L. M., Bube, K. P., 1996, "Immersed interface methods." Department of Energy, *DOE Grant DE-FG06-93ER25181*, Final Report, November 1996. http://www.osti.gov/bridge/servlets/purl/418466-HkIjpO/webviewable/418466.pdf (July 8, 2011)

51. Lian, Y., Shyy, W., Viieru, D., Zhang, B., 2003, "Membrane wing aerodynamics for micro air vehicles." *Progress in Aerospace Sciences* **39**:425–465.

52. Liani, E., Guo, S., Allegri, G., 2007, "Aeroelastic effect on flapping wing performance." *48th AIAA/ASME/ASCE/AHS/ASC Structures, Structural Dynamics, and Materials Conference*, AIAA Paper 2007-2412, Honolulu, Hawaii, April 2007.

53. Lissaman, P., 1983, "Low-Reynolds-Number Airfoils."*Annual Review of Fluid Mechanics* **15**: 223-39.

54. Liu, H., 2002, "Computational biological fluid dynamics: digitizing and visualizing animal swimming and flying." *Journal of Integrated Comparative Biology* **42**:1050-1059.

55. Liu, T., Kuykendoll, K., Rhew, R., Jones, S., 2004, "Avian wings." *24th AIAA Aerodynamic Measurement Technology and Ground Testing Conference*, AIAA Paper 2004-2186, Portland, OR, June 2004.

56. Lockwood, R., Swaddle, J. P., Rayner, J. M. V., 1998, "Avian wingtip shape reconsidered: Wingtip shape indices and morphological adaptations to migration." *Journal of Avian Biology* **29**:273-292.

57. Luo, H., Yin, B., Dai, H., Doyle, J., 2010, "A 3-D computational study of the flow-structure interaction in flapping flight." *48th AIAA aerospace sciences meeting including the new horizons forum and aerospace exposition*, AIAA 2010-556.

58. Maxworthy, T., 1981, "The fluid dynamics of insect flight." *Annual Review of Fluid Mechanics* **13**:329-350.

59. McLetchie, K. W., 2004, *Force and Hydrodynamic Efficiency Measurements of a Three-Dimensional Flapping Foil*, M. S. thesis, Department of Ocean Engineering and Department of Mechanical Engineering, Massachusetts Institute of Technology, Cambridge, MA, p.21.

60. McMichael, J. M., Francis, M. S., 1997, *Micro air vehicles - toward a new dimension in flight*, Federation of American Scientists (FAS), Washington, DC, 12/18/1997, http://www.fas.org/irp/program/collect/docs/mav_auvsi.htm (08/30/2011).

61. Miller, L. A., Peskin, C. S., 2005, "A computational fluid dynamics of 'clap and fling' in the smallest insects." *The Journal of Experimental Biology* **208**:195-212.

62. Munson, B., Young, D., Okiishi, T., 2005, *Fundamentals of Fluid Mechanics*, 5th Edition, John Wiley & Sons, Inc., USA, p.155.

63. Nagai, H., Isogai, K., Fujimoto, T., Hayase, T., 2009, "Experimental and numerical study of forward flight aerodynamics of insect flapping wing." *AIAA Journal* **47(3)**:730-742.

64. Noberg, U. M., 2002, “Structure, form, and function of flight in engineering and the living world.” *Journal of Morphology* **252**:52-81.

65. Okamoto, M., Azuma, A., 2005, "Experimental study on aerodynamic characteristics of unsteady wings at low Reynolds number." *AIAA Journal* **43(12)**:2526-2536.

66. Pai, P. F., 2007, *Highly Flexible Structures: Modeling, Computation and Experimentation*, AIAA, Reston, Virginia.

67. Pai, P. F., Chernova, D. K., Palazotto, A. N., 2009, “Nonlinear modeling and vibration characterization of MAV flapping wings.” *50th AIAA/ASME/ASCE/AHS/ASC Structures, Structural Dynamics and Materials Conference*, Palm Springs, CA, May 2009.

68. Pai, P. F., Ramanathan, S., Hu, J., Chernova, D. K., Qian, X., Wu, G., 2010, “Camera-based noncontact metrology for static/dynamic testing of flexible multibody systems.” *Measurement Science and Technology* **21**.

69. Park, K. J., Rosen, M., Hedenstrom, A., 2001, “Flight kinematics of the Barn Swallow (Hirundo Rustica) over a wide range of speeds in a wind tunnel.” *The Journal of Experimental Biology* **204**:2741–2750.

70. Patone, G., *Flexible Flaps for Separation Control an a Wing with Low Aspect Ratio*, Technical University of Berlin, Berlin, Germany, 29 May 1997. http://www.bionik.tu-berlin.de/user/giani/vortrag/index.htm (March 26, 2009)

71. Pennycuick, C. J., 1968, “A wind-tunnel study of gliding flight in the Pigeon Columbia Livia.” *Journal of Experimental Biology* **49**:509-526.

72. Pennycuick, C. J. 1982, “The flight of Petrels and Albatrosses (Procellariiformes), observed in South Georgia and its vicinity.” *Philosophical Transactions of the Royal Society of London* **B300**:75-106.

73. Pennycuick, C. J., 1983, “Thermal soaring compared in three dissimilar tropical bird species, Fregata Magnificens, Pelecanus Occidentalis and Coragyps Atratus.” *Journal of Experimental Biology* **102**:307-325.

74. Pennycuick, C. J., Klaassen, M., Kvist, A., Lindström A., 1996, “Wingbeat frequency and the body drag anomaly: Wind-tunnel observations on a thrush nightingale (Luscinia Luscinia) and a teal (Anas Crecca).” *Journal of Experimental Biology* **199**:2757-2765.

75. Pennycuick, C. J., 2008, *Modeling the Flying Bird*, Elsevier Inc., Canada, pp.56, 372, 102, 101, 91, 94, 95.

76. Pederzani, J., Haj-Hariri, H., 2006, "Numerical analysis of heaving flexible airfoils in a viscous flow." *AIAA Journal* **44(11)**:2773–9.

77. Platzer, M. F., Jones, K. D., Young, J., Lai, J. C. S., 2008, "Flapping-wing aerodynamics: Progress and challenges." *AIAA Journal* **46 (9)**:2136-2148.

78. Polhamus, E. C., 1968, "Application of the leading-edge-suction analogy of vortex lift to the drag due to lift of sharp-edge delta wings", *National Aeronautics and Space Administration*, Washington, D. C.

79. Powers, D. R., *Magnificent Hummingbird* (Eugenes fulgens), The Birds of North America Online (A. Poole, Ed.). Ithaca: Cornell Lab of Ornithology; Retrieved from the Birds of North America Online, 1996. http://bna.birds.cornell.edu/bna/species/221 doi:10.2173/bna.221 (Aug. 19 2011)

80. Raymer, D. P., 2006, *Aircraft Design: A Conceptual Approach*, 4th Edition, AIAA, Reston, VA.

81. Rayner, J. M. V., 1979, "A vortex theory of animal flight. I. The vortex wake of a hovering animal. II. The forward flight of birds." *Journal of Fluid Mechanics* **91**:731-763.

82. Ritchison, G., *Lecture Notes 3 - Bird Flight II*, EKU Department of Biological Sciences, Richmond, KY. http://people.eku.edu/ritchisong/554notes3.html (Aug. 19, 2011)

83. Roubik, D. W., Sakai, S., Hamid Karim, A. A., 2005, *Pollination Ecology and the Rain Forest: Sarawak studies*, Springer, USA, p. 93.

84. Sane, S. P., Dickinson, M. H., 2001, "The control of flight force by a flapping wing: Lift and drag production." *Journal of Experimental Biology* **204:**2607-2626.

85. Shao, X., Pan, D., Deng, J., Yu, Z., 2010, "Numerical studies on the propulsion and wake structures of finite-span flapping wings with different aspect ratios." *Journal of Hydrodynamics* **22(2)**:147-154.

86. Shyy, W., Ifju, P.G., Viieru, D., 2005, "Membrane wing-based micro air vehicles." *Applied Mechanics Reviews* **58**:283-301.

87. Shyy, W., Lian, Y., Tang, J., Liu, H., Trizila, P., Stanford, B., Bernal, L., Cesnik, C. E. S., Friedmann, P., Ifju, P., 2008, "Computational aerodynamics of low Reynolds number plunging, pitching and flexible wings for MAV applications." *46th AIAA Aerospace Sciences Meeting and Exhibit,* AIAA Paper 2008-523, Reno, NV, January 2008.

88. Shyy, W., Aono, H., Chimakurthi, S. K., Trizila, P., Kang, C.-K., Cesnik, C.E.S., Liu, H., 2010, "Recent progress in flapping wing aerodynamics and aeroelasticity." *Progress in Aerospace Sciences* **46**:284-327.

89. Singh, B., 2006, *Dynamics and Aeroelasticity of Hover Capable Flapping Wings: Experiments and Analysis*, Ph.D. Dissertation, Department of Aerospace Engineering, University of Maryland, College Park, MD.

90. Smith, M. J. C., 1996, "Simulating moth wings aerodynamics: Toward the development of flapping-wing technology." *AIAA Journal* **34(7)**:1348-1355.

91. Smith, M. J. C., Wilkin, P. J., Williams, M. H., 1996, "The advantages of an unsteady panel method in modeling the aerodynamic forces on rigid flapping wings." *Journal of Experimental Biology* **199**:1073–1083.

92. Smith, R., Shyy, W., 1995, "Computation of unsteady laminar flow over a flexible two-dimensional membrane wing." *Physics of Fluids* **7(9)**: 2175–2184.

93. Sohn, M. H., Chang, J. W., 2007, "Flow visualization and aerodynamic load calculation of three types of clap-fling motions in a Weis-Fogh mechanism." *Aerospace Science and Technology* **11:** 119–129.

94. Spedding, G. R., 1986, "The wake of a jackdaw (Corvus monedula) in slow flight." *Journal of Experimental Biology* **125**:287-307.

95. Spedding, G. R., 1987, "The wake of a kestrel (Falco tinnunculus) in gliding flight." *Journal of Experimental Biology* **127**:45-57.

96. Spedding, G. R., 1987, "The wake of a kestrel (Falco tinnunculus) in flapping flight." *Journal of Experimental Biology* **127**:59-78.

97. Spedding, G. R., Hedenström, A., Rosén, M., 2003, "Quantitative studies of the wakes of freely flying birds in a low-turbulence wind tunnel." *Experiments in Fluids* **34**:291-303.

98. Stanford, B., Ifju, P., 2009, "Membrane micro air vehicles with adaptive aerodynamic twist: Numerical modeling." *Journal of Aerospace Engineering* **22(2)**:173-184.

99. Tang, J., Viieru, D., Shyy, W., 2007, "A study of aerodynamics of low Reynolds number flexible airfoils." *37th AIAA Fluid Dynamics Conference and Exhibit*, AIAA Paper 2007-4212, June 2007.

100. Tang, J., Chimakurthi, S. K., Palacios, R., Cesnik, C. E. S., Shyy, W., 2008, "Computational fluid–structure interaction of a deformable flapping wing for micro air vehicle applications." *46th AIAA Aerospace Sciences Meeting and Exhibit*, AIAA Paper 2008-615, Reno, NV, January 2008.

101. Taylor, G. K., Nudds, R. L., Thomas, A. L. R., 2003, "Flying and swimming animals cruise at a Strouhal number tuned for high power efficiency." *Nature (London)* **425**:707–711.

102. Tobalske, B. W., Peacock, W. L., Dial, K. P., 1999, "Kinematics of flap-bounding flight in the Zebra Finch over a wide range of speeds." *The Journal of Experimental Biology* **202**:1725–1739.

103. Tobalske , B. W., Warrick, D. R., Clark, C. J., Powers, D. R., Hedrick, T. L., Hyder, G. A., Biewener, A. A., 2007, "Three-dimensional kinematics of the hummingbird flight." *The Journal of Experimental Biology* **210**:2368-2383.

104. Toomey, J., Eldredge, J. D., 2008, "Numerical and experimental study of the fluid dynamics of a flapping wing with low order flexibility." *Physics of Fluids* **20(073603)**:1–10.

105. Triantafyllou, M. S., Triantafyllou, G. S., Grosenbaugh, M., 1993, "Optimal thrust development in oscillating foils with application to fish propulsion." *Journal of Fluids and Structures* **7(2)**: 205–224.

106. Tuncer, I. H., Platzer, M. F., 2000, "Computational study of flapping airfoil aerodynamics." *Journal of Aircraft* **37**:514-520.

107. Usherwood, J. R., Ellington, C. P., 2002, "The aerodynamics of revolving wings I: Model hawkmoth wings." *Journal of Experimental Biology* **205**:1547-1564.

108. Videler, J. J., 2005, *Avian Flight*, Oxford Ornithology Series, Oxford University Press, New York.

109. Waite, M., *Bird Identification Guide*, Mitch Waite Group. http://identify.whatbird.com/mwg/_/0/attrs.aspx

110. Wang, Z. J., 2000 "Vortex shedding and frequency selection in flapping flight." *Journal of Fluid Mechanics* **410**:323-341.

111. Wang, Z. J., Birch, J. M., Dickinson, M. H., 2004, "Unsteady forces and flows in low Reynolds number hovering flight: Two-dimensional computations vs. robotic wing experiments." *Journal of Experimental Biology* **207**:449-460.

112. Wang, Z. J., 2005, "Dissecting insect flight." *Annual Review of Fluid Mechanics* **37**:183-210.

113. Warrick, D. R., Tobalske, B. W., Powers, D. R., Dickinson, M. H., 2007, "The aerodynamics of hummingbird flight." *Proceedings of the AIAA Aerospace Sciences Meeting.*

114. Weis-Fogh, T., 1973, "Quick estimates of flight fitness in hovering animals, including novel mechanisms for lift production." *Journal of Experimental Biology* **59**:169-230.

115. Willis, D., Israeli, E., Persson, P., Drela, M., Peraire, J., Swartz, S. M., Breuer, K. S., 2007, "A computational framework for fluid structure interaction in biologically inspired flapping flight." *25th AIAA Applied Aerodynamics Conference*, AIAA Paper 2007-3803, Miami, FL, June 2007.

116. Willmott, A. P., Ellington, C. P., 1997, "Measuring the angle of attack of beating insect wings: Robust three-dimensional reconstruction from two-dimensional images." *Journal of Experimental Biology* **200**:2693 -2704.

117. Young, J., Lai, J. C. S., 2004, "Oscillation frequency and amplitude effects on the wake of a plunging airfoil." *AIAA Journal* **42**:2042-2052.

118. Young, J., Walker, S. M., Bomphrey, R. J., Taylor, G. K., Thomas, A. L. R., 2009, "Details of insect wing design and deformation enhance aerodynamic function and flight efficiency." *Science* **325**:1549–52.

119. Zhu, Q., 2007, "Numerical simulation of a flapping foil with chordwise or spanwise flexibility." *AIAA Journal* **45(10)**:2448–2457.

120. Zufferey, J.-C., Beyeler, A., Floreano, D., *Insect-inspired autonomous microflyer*, Laboratory of Intelligent Systems, EPFL, Lausanne, Switzerland, International Symposium on Flying Insects and Robots,

Monte Verita, Ascona, Switzerland, Aig. 2007. http://fir.epfl.ch/docs/FIR_proceedings_online.pdf (Aug. 10, 2011)

121. *Appendix E. Assessing Terrestrial Invertebrate Exposure To Pesticides*, United States Environmental Protection Agency. http://www.epa.gov/espp/litstatus/effects/redleg-frog/naled/appendix-g.pdf (Aug. 10, 2011)

122. *Dragon Fly Species*, Animal Corner, United Kingdom**.** http://www.animalcorner.co.uk/insects/dragonfly/dfspecies.html(Aug. 10, 2011)

123. *Entomopter*, Harvard University, 2007. http://www.flightglobal.com/articles/2007/09/06/216590/picture-harvard-universitys-insect-scale-robot-fly-flies.html (Aug. 10, 2011)

124. *Mexican Free-tailed Bat*, Wikipedia, 4 August 2011. http://www.answers.com/topic/brazilian-free-tailed-bat (Aug. 10, 2011)

125. *Rufous Hummingbird*, Hummingbird Pictures Guide, 2005. http://fohn.net/hummingbird-pictures/rufous-hummingbird.html (Aug. 10, 2011)

126. *Wings for Flight*, National Aviary/America's Bird Zoo, Pittsburgh, PA. http://www.aviary.org/curric/profiles.htm (Aug. 10, 2011)

VITA

Dar'ya Konstantinovna Chernova was born January 1, 1975, in Odessa, Ukraine (former USSR). She came to the United States in 1998 to study at Lincoln University, Missouri. She earned a Bachelor of Science with honors in Economics from Lincoln University, Missouri in 2002. While there, she competed for Lincoln University tennis team as a number one player. She continued on at Lincoln and earned MBA degree in 2005. The same year, she entered a graduate program in Mechanical and Aerospace Engineering at University of Missouri-Columbia. While being a graduate student, she completed the required work and graduated with Bachelor of Science with honors in Mechanical and Aerospace Engineering in 2010. She earned Master of Science degree in 2011.

In 2009, she was chosen to participate in the NREIP internship program in San Diego, CA. She has two children which were born in December of 2005 and in September of 2009.